THE EFFECT OF A BRANS-DICKE COSMOLOGY UPON STELLAR EVOLUTION AND THE EVOLUTION OF GALAXIES

A Dissertation

Presented to the Faculty of the Graduate School

of

Yale University

in Candidacy for the Degree of

Doctor of Philosophy

by

Michael John Prather

May 1976

ABSTRACT

THE EFFECT OF A BRANS-DICKE COSMOLOGY UPON
STELLAR EVOLUTION AND THE EVOLUTION OF GALAXIES

Michael John Prather

Yale University 1976

This thesis examines the effect which a variable G cosmology, such as Brans-Dicke, will have on the evolution of individual stars and of galaxies composed of these stars in the hope that present day observation of globular clusters or giant elliptical galaxies will provide a test for the Brans-Dicke theory. The higher value of the gravitational coupling coefficient G in the past history of various Brans-Dicke universes is studied in detail. A low-density, open universe is selected for study: fractional closure density = 0.2, present Hubble constant = 55 km/s/Mpc, stellar formation at a redshift of 5, and the Brans-Dicke parameter omega = 6.

In this universe a set of stellar evolutionary tracks is computed from the Zero-Age Main Sequence through the Giant Branch to the Horizontal Branch for approximately solar composition, (Y,Z) = (0.25,0.02). When compared at equivalent evolutionary phases, the luminosity of individual stars is found to increase greatly with G from the ZAMS to the HB. The higher G greatly speeds up the evolutionary time scale for the main sequence, and it decreases the core mass at the helium flash, leaving the luminosity of the tip of the GB

and the HB unchanged. The net effect of a higher G on a cluster of stars is to increase the apparent mass at the turn-off and to reduce the lifetimes of all the evolutionary phases from the ZAMS to the HB by the same factor. Thus, the relative number density of stars in the major phases of stellar evolution is unchanged.

A set of metal-poor stellar tracks are computed from the ZAMS to the base of the GB in order to simulate the turn-off and sub-giant regions of globular clusters. At the present epoch the only difference caused by the higher G in the past is the increase in the apparent age of the cluster.

Single-generation, solar abundance models of giant elliptical galaxies show a substantial evolution of the integrated galactic magnitude but have a very small evolution of the integrated colors. The colors and magnitudes of the variable G models evolve almost parallel to those of the constant G models and do not display the expected increase in luminosity with G. The only difference between the two models is that the Brans-Dicke galaxy appears older, and hence redder.

Thus, the effects of a moderately higher value of G in the past are unobservable, as are the effects of a moderately higher G in a nearby cluster.

PREFACE

I would like to acknowledge the genius of A. Einstein, without whose insights, this dissertation would not exist. To the work of C. Brans and R. H. Dicke, I am also indebted for providing me with a subject for this dissertation.

This dissertation is dedicated to my wife, my family, my friends, the staff, students and faculty of the Yale Astronomy Department, and the members of the Planetary Sciences Division of Kitt Peak National Observatory. All of these people--whom I would like to name individually but lack the paper to do so--have aided, supported and encouraged me over the last four years and, thus, enabled me to complete this dissertation.

In particular, I would like to acknowledge my advisor Dr. Pierre Demarque, whose direction, encouragement and, most of all, patience has guided me through this thesis. The advice and assistance of Dr. Allen Sweigart was essential because otherwise I would never have evolved a star off the zero-age main sequence. I would like to thank Mrs. Mary S. Albee, who has aided me in multitudinous ways as a graduate student in the Astronomy Department. Finally, I praise the heavens for the support and endurance of my wife Charlotte Carroll Prather, who survived my dissertation while writing her own.

TABLE OF CONTENTS

CHAPTER I. INTRODUCTION

§1. General Relativity and Brans-Dicke

When the general theory of relativity was presented by Einstein (1916), it accounted for the 43"/century residual precession of Mercury's perihelion that had been noted by Leverrier (1859) and accurately measured 34 years before by Newcomb (1882). The predicted deflection of starlight by the sun was verified during the 1919 solar eclipse (Dyson, Eddington and Davidson 1920), and the general theory gained wide acceptance. Since that time Einstein's general theory of relativity (henceforth GR) has survived all observational tests and has become the "standard" theory of gravitation.

At present, the most viable alternative to GR is the scalar-tensor theory of Brans and Dicke (1961), which predicts a variation of G with the age of the universe. In this thesis I shall consider only the GR and Brans-Dicke cosmologies. For a thorough review of the variety of variable-G cosmologies and their astrophysical and geophysical implications see Wesson (1973). The Brans-Dicke theory (henceforth BD) is a Machian theory in that the local gravitational field is affected by the total mass-energy distribution of the universe. The BD theory contains a dimensionless constant ω and a scalar field ϕ. The coupling constant ω is a measure of the deviation of BD theory from GR theory (BD approaches GR in the limit $\omega\to\infty$). The inverse of the

scalar field ϕ is proportional to the local gravitational coupling coefficient G.

As has been stressed by McVittie (1969), the BD scalar field ϕ--and hence G--is a function of both time and space. For hydrostatic models which involve no time derivatives, the temporal variation of ϕ presents no problems. However, if ϕ has strong spatial variations from the center to the surface of a star, then the application of the non-relativistic hydrostatic equilibrium equation--which includes a spatial derivative and G--will no longer be valid. Eardley (1975) points out that the assumption of a spatially constant ϕ is accurate if the star is non-relativistic. He derives the center-to-surface variation of ϕ (or G) in BD theory which is

$$\left|\frac{\delta\phi}{\phi}\right| \simeq \left|\frac{\delta G}{G}\right| \simeq \frac{1}{2\omega+4}\cdot\frac{U}{c^2} \qquad (1)$$

to first order in U/c^2 where U is the Newtonian gravitational potential. Thus, the spatial variations of ϕ are insignificant ($\sim 10^{-5}$ for a white dwarf star with $\omega = 3$), and I shall assume that the temporal variations of ϕ can be computed from a homogeneous, isotropic universe.

§2. Observational Evidence

The BD predicted rate of decrease in G at the present (equation II.9) is theoretically observable and would provide a direct test of the theory. The preliminary upper limits of $|\dot{G}/G|_0 < 4\cdot 10^{-10}$ yr^{-1} from radar observations of planetary motions (Shapiro et al. 1971) could only rule out

the densest of the BD universes. The more recent results are not yet decisive.

$$(\dot{G}/G)_0 = +4 \pm 8 \cdot 10^{-11} \text{ yr}^{-1} \text{ (Shapiro 1974)} \quad (2)$$

$$= -8 \pm 5 \cdot 10^{-11} \text{ yr}^{-1} \text{ (van Flandern 1975)} \quad (3)$$

In addition to the predicted decrease in G, other notable differences between BD and GR include the classical tests of: (i) the deflection of starlight by the sun where BD predicts a smaller deflection,

$$\Theta(\text{BD}) = \frac{2\omega+3}{2\omega+4} \cdot \Theta(\text{GR}) \; ; \quad (4)$$

and (ii) the precession of Mercury's perihelion where BD also predicts a lower rate,

$$\Delta\phi(\text{BD}) = \frac{3\omega+4}{3\omega+6} \cdot \Delta\phi(\text{GR}) \; . \quad (5)$$

While optical measurements of the deflection of light are limited to solar eclipses and are unlikely to be able to differentiate between BD and GR, radio observations (Counselman et al. 1974, Fomalont and Sramek 1975) may soon be sufficiently accurate to discriminate. The precession of Mercury's perihelion can be compatible with BD if the sun is oblate by a factor of $5 \cdot 10^{-5}$ (Dicke 1964). However, this degree of oblateness is extremely difficult to measure to any degree of concordance (Dicke 1974, Hill et al. 1974, Hill and Stebbins 1975).

The effects of BD theory on nucleosynthesis in the early universe have been investigated by Greenstein (1968). With regard to the primordial production of deuterium and helium,

he finds no observable differences between BD and GR models except for the high density BD universes which produce excessive amounts of helium.

§3. Stars and Variable G

I propose to examine the differences between BD and GR by employing what are possibly the most sensitive instruments to detect changes in G: the stars. As was first pointed out in homology arguments (Teller 1948), the luminosity of a main sequence star is a highly sensitive function of gravity ($L \sim G^7$). These relatively higher luminosity stars, formed at a larger G in a BD universe, will have evolved more rapidly within the same time span than their counterparts in a GR universe (Dicke 1962). The greatest effect will be found in the oldest population of stars which have experienced a larger G for a longer period of time.

For this reason I shall examine the effects of a BD cosmology upon both the evolution of giant elliptical galaxies and the color-magnitude diagram of globular clusters. Giant ellipticals provide one of the better tests because they are composed of old stars and their brightness allows them to be observed at large redshifts. Globular clusters supply more detailed data of the oldest stellar component of our galaxy, but they can only be observed at the present epoch (i.e., $G = G_0$). The integrated colors and magnitudes of nearby giant ellipticals can be used to specify free parameters in the models (e.g., initial mass function).

Then, the more distant giant ellipticals can test the predicted backwards evolution of these quantities.

§4. The Brans-Dicke Variable G

The variations of G in a BD universe are studied in Chapter II. In that chapter the GR and BD cosmological models, which are to be used in the galaxy synthesis, are selected and described. A series of evolutionary tracks for a constant $G = G_0$ and for a BD variable G are computed with the stellar evolution code described in Appendix A. The detailed effects of a variable G upon these stellar models is examined in Chapter III. For the first time, the variable G evolution is followed beyond the main sequence through the giant branch to the horizontal branch.

In Chapter IV,I shall examine the effects of a BD universe upon the distribution of stars in a simulated color-magnitude diagram of an old metal-poor globular cluster. For the construction of these diagrams and for the later synthesis of galaxies, a new method of evolutionary-track interpolation and isochrone construction is described in Appendix B.

The synthesis of giant elliptical galaxies from the evolutionary tracks of Chapter III is completed in Chapter V. This is the first such synthesis to be made from a complete set of tracks which span the evolution from the zero-age main sequence to the horizontal branch. In Chapter V,I shall follow the backwards evolution of the integrated luminosities

and colors of these galaxy models to determine the differential effects between the GR and BD models. I shall conclude in Chapter VI whether the differences in stellar evolution caused by BD theory are possible to detect.

I. References

Brans, C. and R.H. Dicke 1961, Phys.Rev., 124, 925.

Counselman, C.C. III, S.M. Kent, C.A. Knight, I.I. Shapiro, T.A. Clark, H.F. Hinteregger, A.E.E. Rogers and A.R. Whitney 1974, Phys.Rev.Letters, 33, 1621.

Dicke, R.H. 1962, Rev.Mod.Phys., 34, 110.

---------- 1974, Science, 184, 419.

Dyson, F.W., A.S. Eddington and C. Davidson 1920, Mem.R.A.S., 62, 291.

Eardley, D. 1975, private communication.

Einstein, A. 1916, Annalen der Phys., 49, 769.

Fomalont, E.B. and R.A. Sramek 1975, Ap.J., 199, 749.

Greenstein, G.S. 1968, Ap.&Space Sci., 2, 155.

Hill, H.A., P.D. Clayton, D.L. Patz, A.W. Healy, R.T. Stebbins, J.R. Oleson and C.A. Zanoni 1974, Phys.Rev.Letters, 33, 1497.

Hill, H.A. and R.T. Stebbins 1975, Ap.J., 200, 484.

Leverrier, U.-J. 1859, Ann.Obs.Paris, 5, 1.

McVittie, G.C. 1969, The Application of Modern Physics to the Earth and Planetary Interiors (S.K. Runcorn,ed.), (New York: Wiley-Interscience), p.19.

Newcomb, S. 1882 Ast. Papers of the Am. Ephem., 1, 473.

Shapiro, I.I., W.B. Smith, M.B. Ash, R.P. Ingalls and G.H. Pettengill 1971, Phys.Rev.Letters, 26, 27.

Shapiro, I.I. 1974, paper at the 5th Cambridge Conference on Relativity, June 10.

Teller, E. 1948, Phys.Rev., 73, 801.

van Flandern, T.C. 1975, M.N.R.A.S., 170, 333.

Wesson, P.S. 1973, Q.J.R.A.S., 14, 9.

CHAPTER II. THE COSMOLOGICAL MODELS

§1. The Brans-Dicke Equations

For the Brans-Dicke (Brans and Dicke 1961, henceforth BD) models investigated in this paper, I shall assume that the universe is always matter-dominated and has a zero cosmological constant. The cosmological models resulting from the general relativity (GR) theory of Einstein (1916) are the Friedmann (1922, 1924) models which are derived from the Einstein equations. These equations (Weinberg 1972)

$$3\cdot\frac{\ddot{R}}{R} = -4\pi G\rho \tag{1}$$

$$\frac{\ddot{R}}{R} + 2\cdot\frac{\dot{R}^2}{R^2} + 2\cdot\frac{k}{R^2} = 4\pi G\rho, \tag{2}$$

reduce to

$$\frac{\dot{R}^2}{R^2} + \frac{k}{R} = \frac{8\pi G}{3}\cdot\rho, \tag{3}$$

where R is the arbitrary cosmic scale factor, ρ is the density, and k is a constant = 0, ±1. In BD the constant G is replaced by the scalar field ϕ, and the equivalent Einstein equations then yield (Weinberg 1972)

$$3\cdot\frac{\ddot{R}}{R} = -\frac{8\pi\rho}{\phi}\cdot\frac{\omega+2}{2\omega+3} - \omega\cdot\frac{\dot{\phi}^2}{\phi^2} - \frac{\ddot{\phi}}{\phi} \tag{4}$$

$$\frac{\ddot{R}}{R} + 2\cdot\frac{\dot{R}^2}{R^2} + 2\cdot\frac{k}{R^2} = \frac{8\pi\rho}{\phi}\cdot\frac{\omega+1}{2\omega+3} - \frac{\dot{\phi}}{\phi}\cdot\frac{\dot{R}}{R}\ . \tag{5}$$

These equations reduce to

$$\frac{\dot{R}^2}{R^2} + \frac{k}{R^2} = \frac{8\pi\rho}{3\phi} - \frac{\dot{\phi}}{\phi}\cdot\frac{\dot{R}}{R} + \frac{\omega}{6}\cdot\frac{\dot{\phi}^2}{\phi^2}\ , \tag{6}$$

where the derivative of the scalar field is

$$\dot{\phi} = \frac{8\pi\rho t}{2\omega+3} + \frac{C}{R^3} \quad , \tag{7}$$

t is the age of the universe, and ω is the dimensionless coupling constant. The BD theory approaches GR in the limit $\omega \to \infty$.

I shall adopt the constraint initially proposed--but since relaxed--by Brans and Dicke (1961) that $\dot{\phi}R^3 \to 0$ as $R \to 0$. Hence, the constant $C \equiv 0$, and ϕ increases toward the future. The local gravitational coupling coefficient G, as measured by non-relativistic test particles, is not a constant but is a function of the scalar field ϕ.

$$G = \frac{2\omega+4}{2\omega+3}\cdot\frac{1}{\phi} \tag{8}$$

Thus, the value of G was greater in the past and is presently decreasing at the rate,

$$\left(\frac{\dot{G}}{G}\right)_0 = -\frac{8\pi G_0 \rho_0 t_0}{2\omega+4} \quad , \tag{9}$$

where the subscript $_0$ refers to the present value of the quantities.

§2. Solution of the Cosmological Equations

In order to describe the previous history of a BD universe, one must specify the present values (subscript $_0$) of (i) the expansion rate or Hubble constant H_0 where

$$H_0 \equiv \left(\frac{\dot{R}}{R}\right)_0 , \tag{10}$$

(ii) the density or Ω where,

$$\Omega \equiv \rho_0/\rho_{crit} = \rho_0 \cdot \frac{8\pi G_0}{3H_0^2} \quad , \tag{11}$$

and (iii) the value of the scalar field or G_0. The critical density ρ_{crit} is defined for the GR models such that the values of $\Omega < 1$, $\Omega = 1$ and $\Omega > 1$ correspond to open (k=-1), flat (k=0) and closed (k=+1) GR universes. While the Friedmann (1922,1924) solutions to the GR theory are well known and analytic under the present assumptions, the BD models are rarely studied except for the analytic flat-space model. In a BD flat universe the requisite density is greater than the GR critical density,

$$\rho(\text{BD flat-space}) = \frac{(3\omega+4)\cdot(\omega+2)}{3\cdot(\omega+1)^2}\cdot\rho_{crit} \ , \qquad (12)$$

as might be predicted since the gravitational coupling is weakening with age. The solutions for R and ϕ are then

$$R \sim t^{\frac{2\omega+2}{3\omega+4}} \qquad (13)$$

$$\phi \sim t^{\frac{2}{3\omega+4}} \qquad (14)$$

and the present age is

$$t_0 = H_0^{-1}\cdot\left(\frac{2\omega+2}{3\omega+4}\right) \ . \qquad (15)$$

For all other BD models one must solve numerically equations (6) and (7) subject to the conditions: (i) conservation of matter, $\rho \sim R^{-3}$; (ii) present values of H_0, Ω and ϕ_0; (iii) R and t both go to zero at the origin, R(t=0) = 0. In order to start the integration backwards in time, one selects a value of t_0 and uses the values of H_0, Ω and ϕ_0 to determine the value of R_0 and the sign of k. One then integrates backwards in time to the origin to see if condition (iii) above is fulfilled. In general one finds either (a)

$t \to 0$ with R finite in which case the selected t_0 is too low, or (b) $R \to 0$ with t finite in which case the selected t_0 is too high. The true age $\underline{t}_0$ is found by selecting two ages which must bound the true age,

$$0 < t_0^{low} < \underline{t}_0 < t_0^{hi} < H_0^{-1} , \qquad (16)$$

and then applying a binary chop. The value $t_0 = \frac{1}{2}(t_0^{low}+t_0^{hi})$ is used for the integration. In case (a) one redefines $t_0^{low} = t_0$; in case (b), $t_0^{hi} = t_0$. This process is repeated until the true age is bracketed to satisfactory accuracy.

Since the density is given in terms of Ω, the resultant age fraction $(t_0 \cdot H_0)$ is independent of the assumed Hubble constant. The age fractions thus calculated are given in table 1. The analytic values for the GR models are included in order to compare them with the computed values for the BD models with $\omega = 10^{12}$ which should approach the GR limit. The range of values in ω bounds the limits considered to be most probable by Dicke (1974), $5 \leq \omega \leq 9$. For the cases in table 1 the difference in universe ages between the GR and BD models is small and increases from -1% to +3% as the density increases.

At large densities the age for a BD universe is less than that for the corresponding GR universe as would be naively expected. In BD models the gravitational coupling was greater in the past; and thus the initial expansion of the universe would have slowed more quickly; and thus the universe would reach its present state in less time. However, in low-density models the BD age exceeds the GR age.

This phenomenon occurs because the ϕ-field can actually reduce the deceleration. By comparing equations (1) and (4) at the present,

$$\left(\frac{\ddot{R}}{R}\right)_0^{BD} = \frac{1}{\omega+2}\cdot\left(\omega + 3(1-t_0H_0) + \frac{3\omega}{2\omega+4}\cdot\Omega(t_0H_0)^2\right)\cdot\left(\frac{\ddot{R}}{R}\right)_0^{GR}, \quad (17)$$

one can see that the coefficient is less than unity in low-density models ($\Omega<<1$, $t_0H_0\tilde{}1$). Thus, the acceleration backwards to the origin starts off at a slower rate and yields a greater age.

Once the age of a given BD universe is determined, any quantities from the present or past history of the model may be calculated. For example, the present rate of decrease in G calculated from equation (9) with the values of table 1 is shown in table 2. These values for all of the models considered are within the most recent limits (equation I.2) of Shapiro (1974). However, the results (equation I.3) of van Flandern (1975) are compatible only with BD models of high density or large Hubble constant.

Henceforth, I shall no longer be concerned with the present changes in G, but rather with its previous history. The increase in $\log(G/G_0)$ with redshift in a BD universe is shown in figures 1 and 2. Figure 1 shows the effect of differing density universes with a fixed $\omega = 6$; and figure 2, for differing ω-values with a fixed density $\Omega = 0.20$. Since the density is defined in terms of Ω, the function G(z) is independent of the choice of Hubble constant. The gravitational coupling coefficient G rises more steeply and reaches higher values at a given redshift when either the present

density (in terms of Ω) is increased or the coupling constant ω is decreased. In very low density universes ($\Omega < 0.02$) the increase in G back to a redshift of $z = 10$ is negligible.

§3. Selection of Model Parameters

Unfortunately, in a study of this kind one has a multitude of parameters which must be fixed. I shall now set all of the parameters necessary for the cosmological model and try to justify them. For the BD theory in particular, one must specify the dimensionless coupling coefficient ω. I shall set $\omega = 6$ which is the lower limit initially proposed by Brans and Dicke (1961) and is within Dicke's (1974) more recent range of values. The previous assumption that $\dot{\phi}R^3 \to 0$ as $R \to 0$ eliminates the need to fix a second BD parameter. The present expansion rate in terms of the Hubble constant is taken to be $H_0 = 55$ km/s/Mpc. This value is consistent with the most recent measurements (Harris 1974, Kirshner and Kwan 1974, Sandage and Tammann 1974) and gives a GR critical density of $\rho_{crit} = 5.7 \cdot 10^{-30} gm/cm^3$. The present density of the universe is assumed to be $\Omega = 0.20$ or $\rho_0 = 1.13 \cdot 10^{-30} gm/cm^3$. This assumption is consistent with recent results that the universe is open, but it is slightly denser than the value of $\Omega = 0.06$ preferred by Gott *et al.* (1974).

Now that the cosmological parameters are set, one is left with the determination of when the stars in the giant elliptical galaxies were formed and when the globular clusters formed. Although all of the stars in a giant elliptical

were obviously not formed at the same instant in time, I shall assume, as have other authors (Tinsley 1972), that the star formation occurs in a single burst. Larson's (1974) model calculations of elliptical galaxies support this assumption while displaying a realistic spread in star formation. These models show a distinct peak in star formation which occurs in a free-fall time and then predict a rapid decline with little or no star formation at the present.

In addition to simplifying the overall model and eliminating further parameters, the single-generation hypothesis is necessary for computational moderation. Ideally, one should synthesize the stellar population of these giant ellipticals with groups of stars formed over an interval of time in the early universe. This procedure is straight forward for stellar models constructed with a constant G since the evolutionary tracks can be shifted arbitrarily in time with respect to the age of the universe. But when G varies as in a BD universe, the evolutionary tracks are fixed to a specific time of birth. They cannot be shifted to a new birthtime--a new G--but must be entirely recomputed.

A birthtime for the giant elliptical galaxies can be given in terms of either the age of the universe t_{birth} or the redshift z_{birth}. Kristian (1973) finds quasars to be embedded in the center of giant ellipticals whenever the galaxy itself should be discernible. If one postulates that even the most highly redshifted quasars are both cosmological and associated with giant ellipticals, one can set an obser-

vational lower limit to the redshift at galaxy formation: $z_{birth} \gtrsim 3$. With regard to theoretical limitations, Larson's (1974) models predict a range in t_{birth} of from 0.8 to 2.7 Gyr. In order to compare these times with redshifts, the age of a universe with H_0 = 55 km/s/Mpc is plotted against the present density in figure 3 for a range of redshifts z = 3, 5, 8. The ages in figure 3 apply to both a GR universe and a BD universe with $\omega = 6$, and they scale as H_0^{-1}. For the case $\Omega = 0.20$ the range in redshift of $3 < z < 8$ roughly spans the age range predicted by the theoretical models. The only incompatibility between the ages and the redshifts occurs for the high density universes where $t_{birth} \geq 1.0$ Gyr implies $z_{birth} \leq 3$.

As a test of the sensitivity of the overall model to the exact choice of z_{birth}, I shall compare the ranges of stellar evolution times in the redshift range $3 \leq z \leq 8$. For a universe with H_0 = 55 km/s/Mpc (either GR or BD with $\omega = 6$) the look-back time is plotted against redshift in figure 4 for a range of densities. These look-back times are a measure of the stellar evolution times for a constant $G = G_0$. For a larger G the time scale of stellar evolution is speeded up ($L \sim G^7$, Teller 1948), and the resulting evolu-ionary times are the integrated look-back times weighted by $(G/G_0)^7$. In all the cases of figure 4 the GR evolution times vary slightly ($\simeq$10%) over the range in redshift, but the BD evolution times can vary greatly, especially in the high density models. Fortunately, in the assumed low density

model (Ω=0.20) the variation over the redshift range of the BD evolution time (14.8-18.5 Gyr) is not excessive.

Lacking any other information to more accurately determine z_{birth}, I shall assume an intermediate value of z_{birth} = 5. I shall apply this birthtime to single-generation synthesis models of both giant elliptical galaxies and globular clusters. The two different universe models, which I shall be comparing, are denoted STD (GR universe with H_0 = 55 km/s/Mpc, Ω = 0.20, z_{birth} = 5) and BDI (BD universe with ω = 6 and the same parameters as the STD model). A list of redshifts, ages, and G-values for the STD and BDI models is given in table 3.

TABLE 1. FRACTIONAL AGES ($t_0 \cdot H_0$)

FOR BRANS DICKE-UNIVERSE MODELS

	Ω = 0.028	0.200	0.600	1.000	2.000
GR	0.956524	0.846492	0.731896	0.666667	0.570796
$\omega = 10^{12}$	0.956524	0.846492	0.731896	0.666672	0.570796
= 12	0.959231	0.850037	0.732008	0.663955	0.563747
= 6	0.961363	0.852977	0.732514	0.662513	0.559479
= 3	0.964521	0.857549	0.733862	0.661321	0.554775

TABLE 2. PRESENT RATE OF DECREASE IN G

FOR A BRANS-DICKE UNIVERSE

$-(\dot{G}/G)_0$ in units of $(H_0/55$ km/s/Mpc$)$ yr^{-1}

	Ω = 0.028	0.200	0.600	1.000	2.000
ω = 3	4.6(-13)	2.9(-12)	7.4(-12)	1.1(-11)	1.9(-11)
6	2.8(-13)	1.8(-12)	4.6(-12)	7.0(-12)	1.2(-11)
12	1.6(-13)	1.0(-12)	2.6(-12)	4.0(-12)	6.8(-12)

TABLE 3. THE STD AND BDI MODELS

H_0 = 55 km/s/Mpc Ω = 0.20

	GENERAL RELATIVITY	BRANS-DICKE (ω = 6)	
Redshift	Age(Gyr)	Age(Gyr)	G/G_0
0.00	15.049	15.164	1.0000
0.05	14.204	14.319	1.0016
0.10	13.440	13.554	1.0032
0.20	12.113	12.224	1.0063
0.30	11.001	11.107	1.0093
0.40	10.056	10.158	1.0123
0.50	9.246	9.341	1.0153
0.60	8.542	8.633	1.0182
0.70	7.927	8.012	1.0210
0.80	7.386	7.465	1.0238
0.90	6.905	6.979	1.0266
1.00	6.476	6.545	1.0293
1.20	5.744	5.804	1.0347
1.40	5.144	5.195	1.0398
1.60	4.644	4.688	1.0449
1.80	4.222	4.259	1.0498
2.00	3.862	3.892	1.0546
2.20	3.551	3.576	1.0592
2.40	3.280	3.300	1.0637
2.60	3.043	3.059	1.0682
2.80	2.834	2.845	1.0725
3.00	2.648	2.656	1.0767
3.50	2.263	2.263	1.0869
4.00	1.964	1.959	1.0966
4.50	1.726	1.717	1.1058
5.00	1.533	1.521	1.1146
5.50	1.374	1.359	1.1230
6.00	1.241	1.224	1.1311
7.00	1.031	1.011	1.1463
8.00	0.875	0.853	1.1604

II. REFERENCES

Brans, C. and R.H. Dicke 1961, Phys.Rev., 124, 925

Dicke, R.H. 1974, Science, 184, 419.

Einstein, A. 1916, Annalen der Phys., 49, 769.

Friedmann, A. 1922, Z.Phys., 10, 377.

---------- 1924, Z.Phys., 21, 326.

Gott, J.R. III, J.E. Gunn, D.N. Schramm and B.M. Tinsley 1974, Ap.J., 194, 543.

Harris, W.E. 1974, Ph.D. dissertation, University of Toronto, p. 210.

Kirshner, R.P. and J. Kwan 1974, Ap.J., 193, 27.

Kristian, J. 1973, Ap.J.(Letters), 179, L61.

Larson, R.B. 1974, M.N.R.A.S., 166, 585.

Sandage, A. and G.A. Tammann 1974, Ap.J., 194, 559.

Shapiro, I.I. 1974, paper at the 5th Cambridge Conference on Relativity, June 10.

Teller, E. 1948, Phys.Rev., 73, 801.

Tinsley, B.M. 1972, Ap.J.(Letters), 173, L93.

van Flandern, T.C. 1975, M.N.R.A.S., 170, 333.

Weinberg, S. 1972, Gravitation and Cosmology, (New York: Wiley & Sons), Chapters 15 & 16.

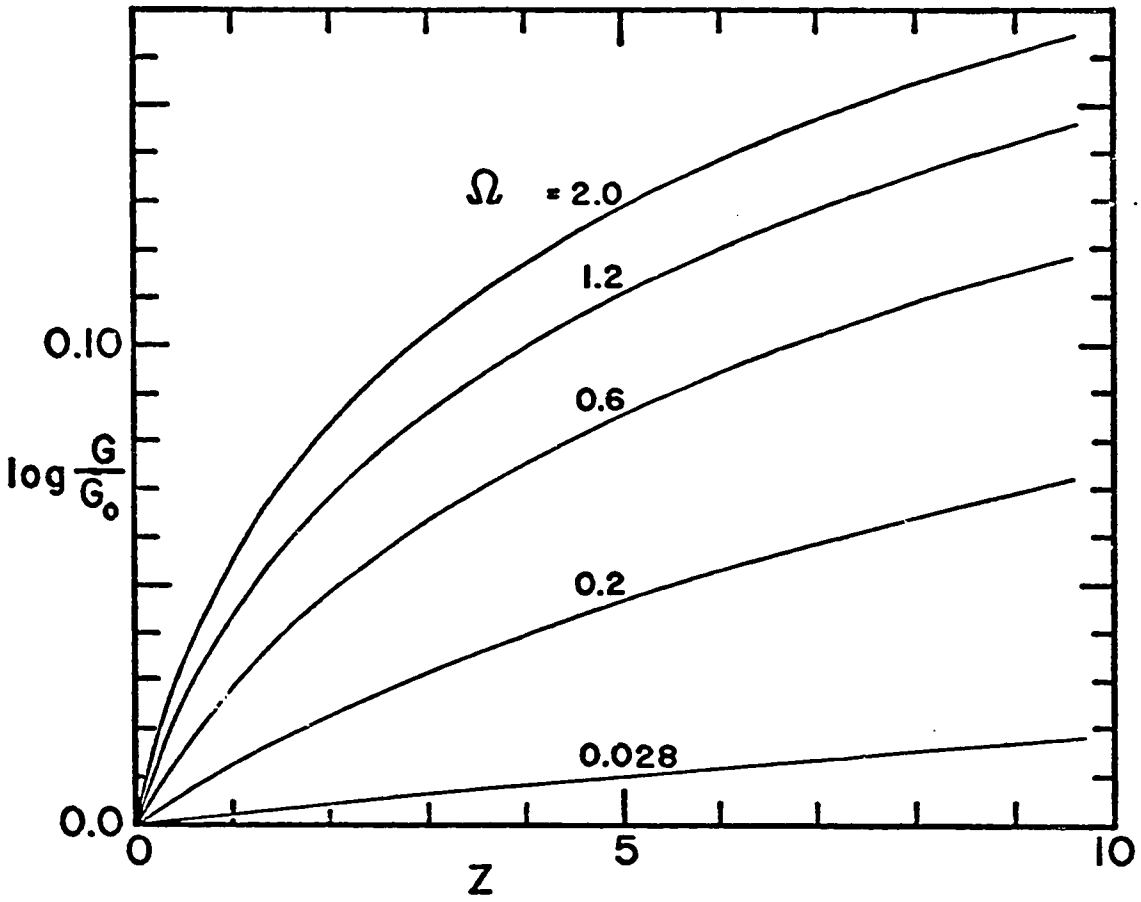

Fig.1.---Log(G/G_0) vs. z. The increase in G with redshift z for a Brans-Dicke universe with $\omega = 6$ is shown for models with differing densities Ω, where $\Omega \equiv \rho_0/\rho_{crit} = \rho_0 \cdot 3H_0^2/8\pi G_0$. The function G(z) is independent of the Hubble constant.

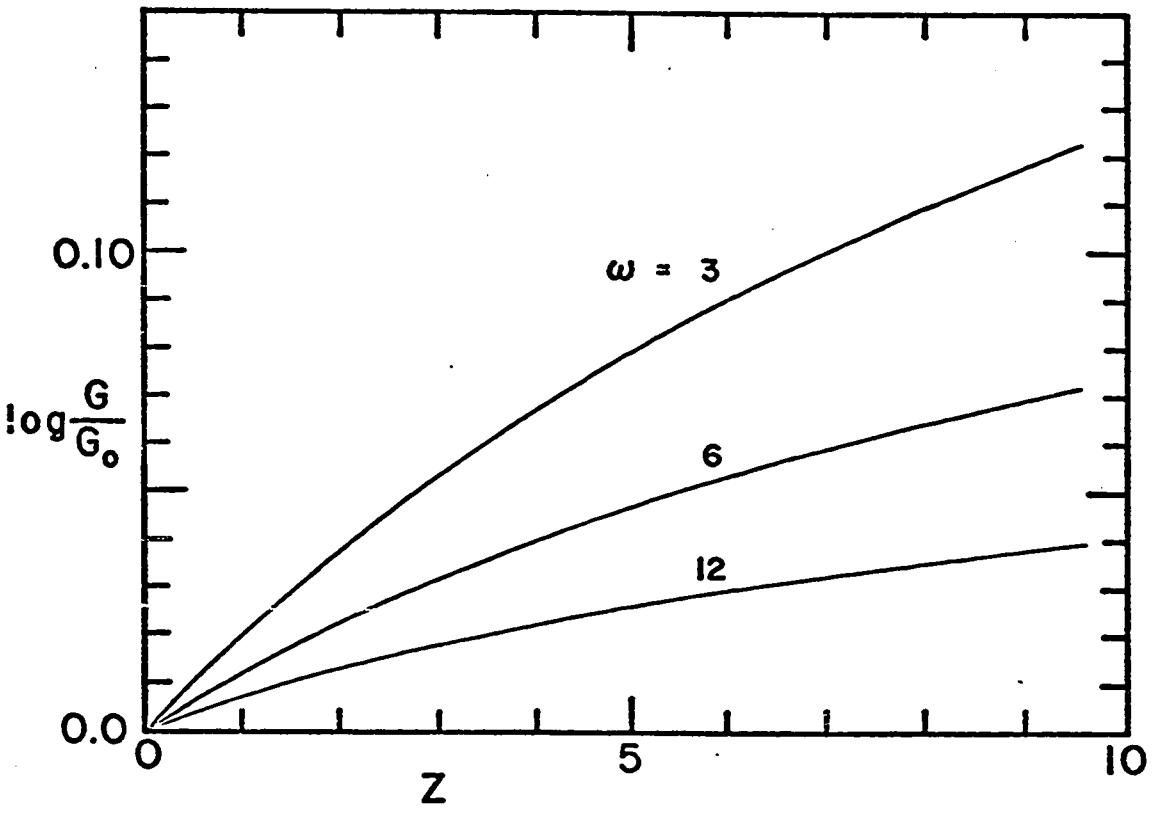

Fig.2.---Log(G/G) vs. z. The increase in G with redshift z for $\Omega = 0.20$ is shown for a Brans-Dicke universe with different values of ω. The function G(z) is independent of the Hubble constant.

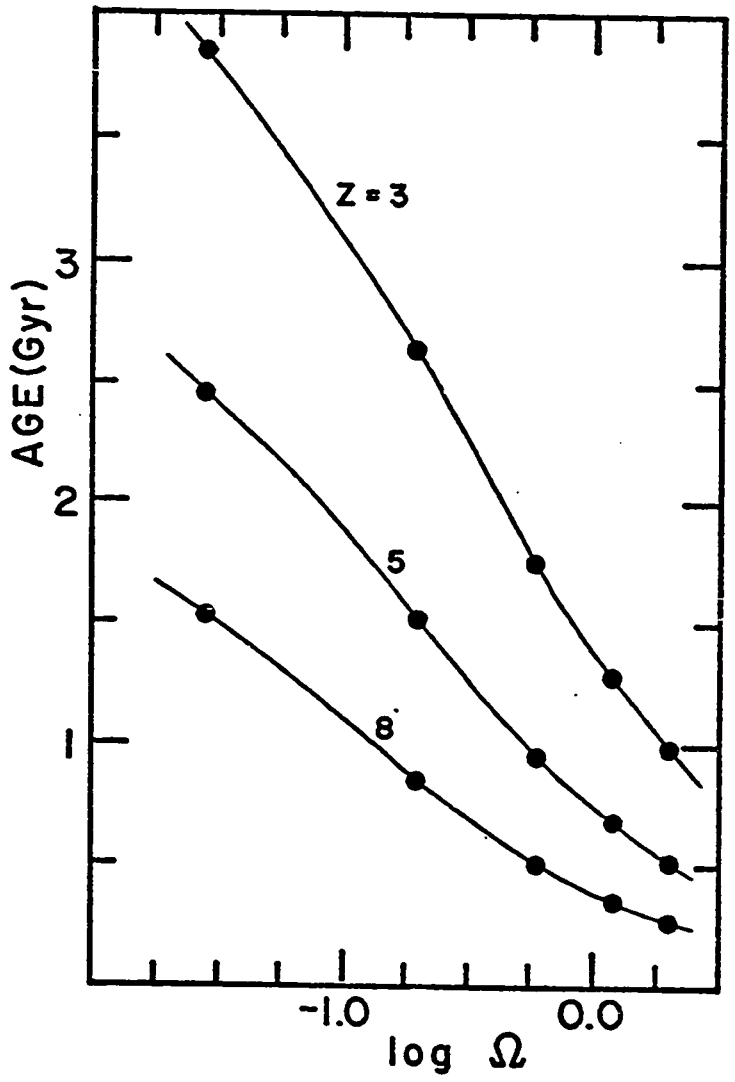

Fig.3.---Age of the universe at different redshifts z vs. the present density Ω. At a fixed redshift the age of the universe decreases as the fractional closure density Ω increases. The ages given are for a Brans-Dicke universe with $\omega = 6$ but differ unnoticeably from the General Relativity models. The ages correspond to $H_0 = 55$ km/s/Mpc and scale as H_0^{-1}.

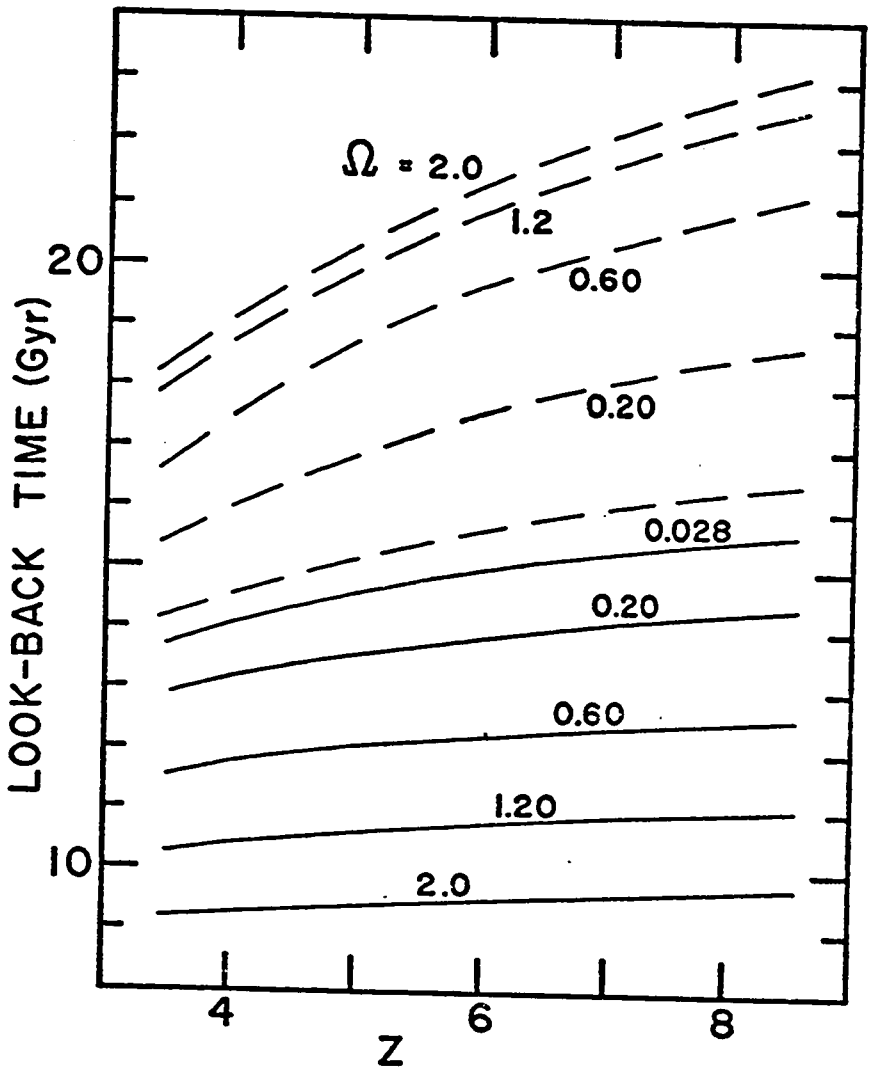

Fig.4.---Look-back time vs. z. The look-back time as a function of redshift z is shown for a Brans-Dicke universe with $\omega = 6$ and $H_0 = 55$ km/s/Mpc. The solid lines represent the direct time difference between the present age of the universe and the age at the given redshift; the dashed lines are the integrated time differences weighted by $(G/G_0)^7$. The curves are labelled with the fractional closure density Ω.

CHAPTER III. THE EFFECT OF G ON STARS

§1. Introduction

The static effects of a decreasing gravitational coupling coefficient G upon the evolution of stars will be examined in extensive detail. A series of stellar models are evolved from the zero-age main sequence (ZAMS) through the giant branch (GB) to the horizontal branch (HB) for the Brans-Dicke model proposed in Chapter II (BDI: $\omega=6$, $H_0=55$ km/s/Mpc, $\Omega=0.20$). The results of this examination significantly extend the knowledge of the effect of $G \neq G_0$ upon stellar evolution. The generalized effects of G which are derived in this chapter are not restricted to the particular Brans-Dicke model.

Early work in this area (Teller 1948, Gamow 1967) used homology arguments to claim $L \sim G^7$ on the main sequence. This result was then applied to the sun to rule out the extreme case $G \sim t^{-1}$ (Dirac 1938) based upon either the temperature (Teller) or the age (Gamow) of the earth. Pochoda and Schwarzschild (1964) first constructed solar models for a variable G of the form $G \sim t^{-n}$. They also found it difficult to produce an acceptable model of the sun for the extreme case of $n = 1$, but were easily able to construct a solar model for the case of $n = 0.2$--equivalent to Brans-Dicke flat space with $\omega = 2$. Roeder and Demarque (1966) also computed solar models for a range of Brans-Dicke flat-space universes (ω = 4,6,8; H_0 = 75,100,113 km/s/Mpc). They were able to fit these models to the observed present-day sun by a reasonable

variation in the initial chemical composition. Ezer and Cameron (1966) followed the evolution of a solar model from the early contraction phase through to an age of 4.5 Gyr for a single Brans-Dicke model ($\omega = 5$, $H_0 = 75$ km/s/Mpc, $t_0 = 7.0$ Gyr). Compared with a standard model, their variable G model showed less lithium depletion and a factor of 4 increase in the present-day B^8 neutrino flux.

Interest in the solar-neutrino problem (see review of Bahcall and Sears 1972) also provoked Shaviv and Bahcall (1969) to construct a wide variety of Brans-Dicke solar models. For all of their decreasing-G models they found an increase in the expected neutrino flux, thus increasing the discrepancy between observation and theory. All of these studies have been limited to the effect of a decreasing G upon the sun and the earth and are unable to rule out any reasonable Brans-Dicke model. The increase in the neutrino-flux for the Brans-Dicke models cannot be considered conclusive evidence against these models since even the standard models are unable to match the extremely low observed value.

The effect of a Brans-Dicke universe was extended beyond the solar models by Dicke and Peebles (1965) who used the homology result $L \sim G^7$ and a variation $G \sim t^{-n}$. They derived effective ages for cluster turn-offs assuming that the turn-off age $\sim \int L^{-1} dt$. Their results are limited, however, by the accuracy of the homology relation and to the flat-space Brans-Dicke models. Roeder (1967) computed a series of turn-off tracks in the mass range 0.9 $M_\odot$ to 1.4 $M_\odot$ with composition

(X,Z) = (0.68,0.03) for Brans-Dicke flat-space model with $\omega = 6$ and $H_0 = 75$ km/s/Mpc. His empirical result $L \sim G^{7.02}$ agrees remarkably well with the earlier homology results for the main sequence. The resulting cluster models from the Brans-Dicke tracks could be fitted to observed clusters equally as well as the standard models. These models are restricted, however, to main-sequence turn-offs and to cluster ages of less than 3 Gyr out of a universe age of 8.8 Gyr. Tinsley (1972) is one of the few prople to even comment on the effect of G upon advanced stellar evolution. She claims that the integrated GB luminosity for a star is independent of G since the amount of hydrogen burned on the GB is unaffected by G.

All of these efforts, with the exception of Tinsley, have been restricted to main-sequence evolution of solar-type models with ages significantly shorter than the age of the universe. In this chapter I shall follow the evolution through to the HB of solar-composition stars which formed very early in the history of a Brans-Dicke universe and, hence, have experienced a larger G over a longer period of time than their recently formed counterparts. These models are evolved under the conditions particular to a specific Brans-Dicke universe (BDI) and will be used for galaxy synthesis in Chapter V. For the present, however, I shall generalize the results as much as possible in order to derive the effects of G upon evolutionary phases which may be considered independent of the previous history of G. I will compare my main-sequence results with the previous studies

and will present new information about the effect of G upon the GB and the HB.

The selection of stellar models to be constructed was based upon the primary objective of galaxy synthesis and also upon a generous but still finite computing budget. The evolutionary sequence computed with a constant G for the STD universe model ranges from 0.5 $M_\odot$ to 1.2 $M_\odot$ in intervals of 0.1 $M_\odot$; the BDI (ω=6, Ω=0.20, H_0=55 km/s/Mpc, z_{birth}=5) sequence ranges from 0.5 $M_\odot$ to 1.1 $M_\odot$. The close spacing in mass of these tracks provides a sufficiently fine grid for the construction of isochrones, and the 0.5 $M_\odot$ track allows the position of the lower main sequence to be properly located. In order to span the same range of ages for both sets of tracks, the STD models are computed up to 1.2 $M_\odot$ (GB age = 6.5 Gyr), while the BDI models only go up to 1.1 $M_\odot$ (GB age = 6.2 Gyr). The computing limitations allowed for the calculation of only four GB tracks (≃75% of computing budget). Because both the STD and the BDI universe models have approximately the same age range of 1.5 Gyr to 15 Gyr from a redshift of z = 5 to the present, the GB tracks were selected in order to span equivalent age ranges from z = 0.8 to z = 0.0 (7.5-15.1 Gyr): 1.2-1.0 $M_\odot$ STD (8.0-14.3 Gyr) and 1.1-0.9 $M_\odot$ BDI (7.7-17.1 Gyr).

The evolutionary sequences start at the chemically homogeneous ZAMS and are computed with the evolution code which is described in Appendix A. This evolution code is a standard Henyey-type code (Henyey, Forbes and Gould 1964) and was

written specifically by the author for the purpose of this research. The chemical abundances were chosen to be solar-type composition, (X,Y,Z) = (0.73,0.25,0.02), and a mixing length equal to one pressure-scale height ($\ell/H = 1$) was used for the computation of the temperature gradient in the convective envelope. The radiative opacities were taken from Cox and Stewart (1970); and the thermonuclear reaction rates, from Fowler, Caughlan and Zimmerman (1975). Appendix A contains full details of the calculations.

For the STD evolutionary sequences the value of G was held constant to its present-day value of G_0. For the BDI sequences the value of $\log(G/G_0)$ was computed from $s = \log(t_0/t)$ where

t_0 = present age of the universe = 15.16 Gyr,
t = age of the universe at the time of the model,
= age of stellar model + $t(z=5)$,
$t(z=5)$ = 1.521 Gyr.

A least-squares fitting of log G vs. log s for the BDI universe model was applied over the range z = 5 to z = 0. The resulting relation is used to calculate the value of G at any point in the evolution of the BDI models.

$$\log(G/G_0) = 0.0271508 \cdot s + 0.0201262 \cdot s^2$$

Let us now examine how G affects stellar models by comparing the BDI models with the STD models.

§2. The Static ZAMS

In examining the zero-age main sequence, we are interested in the detailed effects of G upon chemically homogeneous static models with regard to their influence upon (i) the position of

the main sequence in the HR-diagram, (ii) the main sequence lifetimes, and (iii) the behavior of the evolution at the turn-off (e.g., prediction of gaps). An additional ZAMS sequence was calculated in order to test the linearity of the G-effects over a range of $\log(G/G_0) = 0.0$ (STD), +0.0472 (BDI), and +0.0723. Furthermore, a pair of ZAMS for the composition (Y,Z) = (0.25,0.01) with $\log(G/G_0) = 0.0$ and +0.100 were also computed to determine if the effects of G are independent of small variations in metallicity. The (log L, log M)-relationship for all five ZAMS is shown in figure 1. The increase in luminosity with G is both uniform across this mass range (0.5-1.2 $M_\odot$) and linear in log G. However, for larger masses or for larger values of G, the turn-over in the mass-luminosity relationship--expected for the CNO-dominated higher mass stars--will become noticeable. Thus, the smooth linearity of the relations will be destroyed.

The theoretical HR-diagram for the three ZAMS of metallicity Z = 0.02 is shown in figure 2. For a given mass, the increase in G causes a large increase in L,

$$L \sim G^{6.3\text{-}7.0}\, M^{4.7},$$

and a significant increase in the effective temperature,

$$T_{eff} \sim G^{1.0\text{-}1.5}.$$

However, since the ZAMS shifts almost parallel to itself, the net observable effect of G upon a cluster of stars is to shift the main sequence as a whole by a small amount to the blue,

$$T_{eff}\ (\text{ZAMS}) \sim G^{0.2}.$$

Ignoring this small shift in T_{eff}, the mass at a point on the main sequence varies with G, $M \sim G^{-1.4}$. The resultant effect on the surface gravity g of stars at a given luminosity on the main sequence is small,

$$g \sim GM/R^2 \sim GM\cdot(T_{eff}^4/L) \sim G^{-0.4}.$$

Allowing for the slight ZAMS shift in T_{eff}, a very small positive variation of g with G is expected,

$$g(ZAMS) \sim G^{+0.4}.$$

The uniform change in total luminosity of a star with respect to G does not necessarily imply that all the other quantities of main sequence evolution, such as core exhaustion and time scales, may be rescaled in a similar manner. Figure 3 shows the (fractional luminosity, mass)-relationship for the Z = 0.02 ZAMS sequences. The fractional luminosity due to the PP2, PP3 and CNO cycles is plotted; but the PP1 cycle is not included since it is dominant and always contributes at least 90% of the luminosity in all of the models. As can be seen in figure 3, an increase in G causes an increase in the effective mass of the star. The behavior of the central density and the central temperature with mass is shown in figure 4 for the same ZAMS sequences. Once again, with respect to the central temperature, an increase in G is equivalent to an increase in mass. However, while the central density does increase with G, it does not correspond to a straightforward mass shift.

As an example of these effects, consider the three stellar models which are circled in figures 1, 3 and 4: 1.2 $M_\odot$

(log G/G_0=0.0), 1.0 M_θ(+0.047) and 0.9 M_θ(+0.072). With regard to their central temperatures and fractional luminosities, one would judge all three stars to be alike. By comparing their total luminosities, one would point out that even larger values of G are needed for equality. Contrary to either of the above, by comparing central densities, one would reduce the differences in G to create equality.

Aside from merely presenting the complex G-effects upon the ZAMS models, I would like to resolve the various differences in order to be able to predict the main-sequence lifetime and the behavior at the turn-off. The turn-off of the 1.0 M_θ model in the example will depend upon whether it exhausts its core as a 1.2 M_θ or a 1.0 M_θ standard model. This matter is clarified by examining how the energy generation ε--and hence the burning rate--varies with mass fraction throughout the star. Figure 5 shows the (log ε, M)-relationship for the 1.0 and 1.2 M_θ standard models and for the 1.0 M_θ model with $\log(G/G_0) = +0.047$. It can be seen in figure 5 that (i) the higher value of G causes an increase in the burning rate throughout the star; (ii) the new rates are basically a constant multiple of the burning rates of the standard model of the same mass; and hence, (iii) the star with a higher G will leave the main sequence in the same manner as a standard model of the same mass but in a shorter time. The above conslusion holds only for the mass range and for the G values such that a convective core does not develop and dominate the core during hydrogen core-exhaustion. In order

to study this latter effect, one must construct models with higher masses ($M > 1.2\ M_\odot$) than those considered in this paper.

For the chemically homogeneous ZAMS one has the advantage of being able to use homology results to compare with the model calculations. The most straightforward derivation of the homology relations uses the differential equations of stellar structure (see Schwarzschild 1958, p. 96ff) assuming that the star is in radiative equilibrium throughout.

$$dP/dm = - Gm/4\pi r^4 \tag{1}$$

$$dr/dm = + 1/4\pi r^2\rho \tag{2}$$

$$dL/dm = + \varepsilon \tag{3}$$

$$dT/dm = - (3/4ac)\cdot(\kappa/T^3)\cdot(L/16\pi r^4) \tag{4}$$

One uses the dimensionality of these equations along with (i) the perfect gas law, $P \sim \rho T$; (ii) an energy generation of the form $\varepsilon \sim \rho T^\nu$; and (iii) an opacity of the form $\kappa \sim \rho^{1+\alpha}/T^{3.5+\beta}$. The resulting proportionalities,

$$P_c R^4 \sim GM^2 \tag{5}$$

$$P_c R^3/T_c \sim M \tag{6}$$

$$L/P_c T_c^{\nu-1} \sim M \tag{7}$$

$$T_c^{8.5+\alpha+\beta} R^4/L P_c^{1+\alpha} \sim M\ , \tag{8}$$

can be solved for the dependences upon G and M,

$$P_c \sim G^{1+4a}\cdot M^{2+4b} \tag{9}$$

$$T_c \sim G^{1+a}\cdot M^{1+b} \tag{10}$$

$$L \sim G^{\nu+(\nu+3)a}\cdot M^{(\nu+2)+(\nu+3)b} \tag{11}$$

$$R \sim G^{-a}\cdot M^{-b}\ , \tag{12}$$

where

$$a = (7.5 - \nu + \beta)/(2.5 + \nu + 3\alpha - \beta) \tag{13}$$

$$b = (3.5 - \nu - \alpha + \beta)/(2.5 + \nu + 3\alpha - \beta)\ . \tag{14}$$

In order to determine the values of (ν, α, β), the full range of stellar models was plotted in the (log ρ, log T)-plane. The true form of the PP-chain energy generation, $\varepsilon \sim \rho T^{-2/3} \cdot \exp\{-3380/T^{1/3}\}$, and the radiative opacities of Cox and Stewart (1970) were examined in the (log ρ, log T)-region of interest. The following values of (ν, α, β) describe most of the variation:

$$\nu = 4.6 \pm 0.5$$
$$\alpha = -0.60 \pm 0.06$$
$$\beta = -1.0 \pm 0.3 \ .$$

A comparison of the homology predictions with the model calculations is given in table 1 and demonstrates the compatibility of the two independent methods. The results of previous studies, $L \sim G^{7}$ (homology) and $L \sim G^{7.02}$ (Roeder 1967), are consistent with these new results.

§3. Main Sequence Evolution

I shall now turn from the study of the effects of a static G upon the ZAMS to the examination of the models evolving under the decreasing G of the BDI model universe. The moment one allows evolution to proceed, one has difficulty in separating the G-effects from the evolution effects. For the main sequence I claim that models of identical central hydrogen abundance X_c are comparable; and similarly for the giant branch, models of identical helium core-mass M_c. The evolutionary tracks for the STD models and for the BDI models are shown in the (log L, log T_{eff})-plane in figures 6 and 7, respectively. In the theoretical HR-diagram the most obvious difference between the two sets of tracks is the main-sequence

dip in the BDI models. These models decrease in luminosity as G decreases until $X_c \simeq 0.50$. At this point the evolution-induced increase in luminosity overcomes the G-induced decrease in luminosity and the subsequent evolution of the BDI models resembles the STD models.

For the moment, consider the change in luminosity due to a change in G from the main sequence to the base of the giant branch. In figure 8 the difference in luminosity between the BDI and STD models of a star at equivalent evolutionary phases (i.e., the same X_c or M_c) is plotted against the $\log(G/G_0)$ value of the BDI model. The models with $X_c > 0.20$ seem to fall along the relation $L \sim G^{6.6}$. However, the models with $X_c < 0.01$ up to $M_c = 0.170$ fit best to the relation $L \sim G^{4.0}$. Thus at the point near hydrogen core-exhaustion ($0.20 > X_c > 0.01$), there is a transition in the stellar structure which causes a change in the luminosity's dependence upon G (e.g., a shift from core burning to shell burning).

In order to predict the main-sequence lifetimes, one assumes that the hydrogen burning rate for the bulk of the main sequence is increased uniformly throughout the star by an increase in G (shown for the ZAMS in §2). One then expects the same amount of hydrogen to be exhausted and the turn-off times to be proportional to the time-weighted mean of the inverse of the luminosity,

$$\tau_{\text{turn-off}} \sim \int_{\text{ZAMS}}^{\text{turn-off}} G^{-6.6}\, dt \,. \qquad (15)$$

The main sequence lifetimes of the BDI models agree well enough with this assumption (see Chapter IV for a more detailed comparison of predicted and computed turn-offs).

One would like also to compare the time a star takes to cross the HR-diagram from the turn-off to the base of the giant branch. Unfortunately, a relatively large amount of time is spent by a star at core-exhaustion as compared with this traverse time. Thus, for the small differences in G of the BDI models the errors in determining the age of a model at a specific evolutionary phase at the turn-off override any detectable differences in the traverse time.

§4. The Giant Branch

In determining the effects of G upon the giant branch(GB), I am limited to the study of the two BDI giant-branch tracks. Although G is monotonically decreasing as the stellar model ages in the BDI universe, the time scale of evolution along the GB is sufficiently fast to consider these two GB tracks as having a constant G: $0.9\ M_\odot$(log G/G_0 = -0.0014) and $1.1\ M_\odot$(+0.010).

As was pointed out in §1, the STD giant-branch tracks were computed for different masses (1.0 and 1.2 $M_\odot$), and thus a direct comparison of the models for G effects is not possible. It is possible, however, to use the STD models to eliminate the effects due to a difference in stellar mass. As an example, consider the four GB's in the (log L, log T_{eff})-plane which are shown in figure 9. The effect of G upon the

effective temperature of the GB may be non-zero, but it is certainly small. For the 1.1 $M_\odot$ BDI model the increase in log T_{eff} is at most +0.002 for the increase in log G of +0.010.

The dip in luminosity along the GB, which is caused by the encounter of the hydrogen shell with the composition discontinuity left by the convective envelope, is denoted in figure 9. Below this dip the hydrogen shell is burning through the partially exhausted hydrogen profile which is a remnant of the main sequence evolution. Since this profile varies considerably with stellar mass, it is difficult to compare models of different mass in this region.

Above this luminosity dip the hydrogen shell is burning through an envelope of constant composition, and the only parameters of the static model are total mass, core mass and G. While differences in the composition of the envelope will affect the evolution of the models, the envelope compositions of the four models are almost identical. (The difference of 0.002 in the envelope hydrogen abundance among the four models is not necessarily real, but is probably due to the point structure of the models at the base of the convective envelope.)

The (luminosity, core mass)-relation for the four GB's is shown in figure 10. Above the luminosity dip (M_c>0.25) the luminosity becomes independent of total mass for both STD models. A crude graphical fit to the (L, M_c)-relation for the STD models above this dip yields,

$$\log(L/L_\odot) = 5.10 + 3.32 \cdot \log(M_c/M_\odot - 0.172) \ . \qquad (16)$$

The G effects can be easily isolated from the mass effects by comparing the BDI models with the STD models at a fixed core mass, and they are listed in table 2. The obvious conclusion is that G has a very large influence upon the structure of the individual models.

A region of great interest in GB evolution is the terminal phase of the GB, the helium core flash. In the computations the evolution was followed until the helium luminosity exceeded 10^3 solar luminosities ($\log L_{He}/L_\odot > 3.0$), at which point it was assumed that the star leaves the GB for the horizontal branch. A description of the four GB models at the core flash is given in table 3.

The quantitative effect of G upon the core mass at the helium flash was determined by using the STD models to predict the core masses for a 0.9 and 1.1 $M_\odot$ STD model. I then applied the formula $dM_c/dX = +0.2$ (Sweigart 1975) to make a small correction for the difference in envelope abundance. The resulting dependence is

$$M_c \sim G^{-1.86\pm0.33} \qquad (0.9\ M_\odot \text{ BDI})$$

$$M_c \sim G^{-1.51\pm0.05} \qquad (1.1\ M_\odot \text{ BDI}) ,$$

where the quoted error corresponds to an error in the core mass of $\pm0.0005\ M_\odot$.

These results agree remarkably well with the simple-minded homology argument that is derived as follows. From the stellar structure equations (1) and (2) one has

$$P_c \sim GM_c^2/R_c^4 \tag{17}$$

$$\rho_c \sim M_c/R_c^3 , \tag{18}$$

where the subscript $_c$ refers to the core values of mass and radius and to the central values of pressure and density. Combining these equations to eliminate the radius and assuming that the core flash is triggered at a certain central pressure--and hence density since the core is degenerate--one derives

$$M_c \sim G^{-1.5} \tag{19}$$

Perhaps the most interesting feature of table 3 is that the maximum luminosity of the GB at core flash is not very sensitive to G. The increase in L with G at a fixed core mass is offset by the decrease of the core-flash M_c with G. One can estimate the G dependence by taking the (L, M_c)-relation of equation (16), adopting $L \sim G^7$ from table 2, and assuming the veracity of equation (19). In the region about $M_c = 0.47$ one derives,

$$L(\text{core flash}) \sim G^{-1} \tag{20}$$

While this result does not quantitatively agree with the models given in table 3, it does predict the mildly inverse relationship between L(core flash) and G which is shown by the models.

Thus far, I have shown that G has little effect upon either the shape of the GB track or its position or its extent in the theoretical HR-diagram. The important descriptive parameter which still remains is the time scale of GB evolution. The time interval spent by the four GB models in the region $\log(L/L_\odot) = 2.0$ to 3.0 is given in table 4. The time decreases as G increases since there is a lesser increment

in the core mass (i.e., less fuel burned) over the same luminosity interval. With equation (16) and the assumption $L \sim G^7$, one can make an analytical estimate of the G effects,

$$\tau \sim \Delta M_c/L \sim G^{-2} \quad . \tag{21}$$

This crude result adequately describes the proportionality to within a factor of G which is shown by the BDI models in table 4.

As a potentially observable criterion one would like to examine how the luminosity function N(L) depends on G. For a uniform mass distribution of stars N(L) is defined as the number of stars expected in the luminosity interval $(\log L - \frac{\Delta}{2}, \log L + \frac{\Delta}{2})$. For a single GB track the luminosity function can be defined empirically in terms of the time spent in a given luminosity interval,

$$N(L) \equiv \tau(\log L + \tfrac{\Delta}{2}) - \tau(\log L - \tfrac{\Delta}{2}) \quad , \tag{22}$$

or it can be defined theoretically,

$$N(L) \equiv \Delta/(\partial \log L/\partial \tau) \quad . \tag{23}$$

An analytical evaluation of N(L), which is valid above the luminosity dip, can be made from the time derivative of equation (16) and from

$$dM_c(\theta)/d\tau(\mathrm{Myr}) = 1.47 \cdot 10^{-5} L(\theta) \quad , \tag{24}$$

which yields

$$N(L) = 1.4 \cdot 10^{-3} \cdot \Delta/L(\theta)^{+0.7} \quad (\mathrm{Myr}). \tag{25}$$

The empirical luminosity function (equation 22) of the 1.2 M_θ giant-branch track is compared in figure 11 with the theoretical luminosity function of equation (25). The two luminosity functions agree well above the luminosity dip,

but the theoretical form consistently underestimates the time spent below this point. The empirical luminosity functions for the other three GB tracks are not plotted because their differences would not be noticeable on the graph scale of figure 11 except in the region about the luminosity dip. The sharp rise in N(L) at the lower luminosities correctly predicts the relative overabundance of low-luminosity giant stars.

In conclusion, the GB can be treated as a static-G case in the Brans-Dicke type universes due to its relatively short time span. The major effect of an increase in G is to reduce the lifetime of the GB. Secondary effects are the slight reduction in luminosity at the top of the GB and the small shift of the GB as a whole to the blue ($T_{eff} \sim G^{<0.2}$).

§5. The Horizontal Branch

The four basic horizontal branch (HB) models were constructed as a continuation of the four GB models with the core mass and shell structure existing at the helium core flash. These models were reconverged with central helium burning on the zero-age horizontal branch (ZAHB) and then evolved along the HB. Only the 1.0 M_θ STD model was evolved to helium core-exhaustion because of the computing limitations.

The HB star is presumed to leave the GB at the core flash and to reappear on the ZAHB with the same hydrogen shell structure and a uniform increase in carbon throughout

the helium core (Z=0.02 → Z=0.05). For the helium burning in the core, only the triple-alpha reaction is used; the alpha-carbon reaction which is important during helium core exhaustion is not included. The semi-convection which greatly extends the HB lifetime was not treated rigorously (Robertson and Faulkner 1972), but was approximated by the forced convective overshooting described by Castellani, Gianonne and Renzini (1971). Sweigart and Gross (1974) have shown that this approximation yields equivalent HB ages.

The number of parameters necessary to describe a ZAHB model--core mass M_c in addition to total mass M_* and composition--prohibited the computation of a full grid of models. Using the four HB models continued from the GB, identical ZAHB and evolved HB models were computed with $G \neq G_0$ to discern the effects of G on the HB. An enormous set of HB models from Sweigart and Gross (1975) is used to determine the HB variations with core mass and total mass.

Considering the observable quantities--luminosity and color--these relatively high-mass, metal-rich stars do not describe a horizontal branch in the color-magnitude diagram; but rather, they fall in a clump immediately to the blue of the GB about $M_{bol} \approx 0^m.5$. As measured by the difference in effective temperature from the GB of the same stellar mass, the color of these stars varies little with either G, M_c, or M_* for $M_c < 0.5 \cdot M_*$. The luminosity of the HB model is composed of both hydrogen L_H and helium L_{He} sources which strongly depend on G and M_c.

$$L_H \sim G^{3.0\pm0.4} \cdot M_c^{2.0\pm0.3} \cdot M_*^{0.5\pm0.2} \quad (26)$$

$$L_{He} \sim G^{6.5\pm0.5} \cdot M_c^{4.6\pm0.5} \cdot L_H^{-0.06\pm0.01} \quad (27)$$

The notation L_H and L_{He} apply only to the ZAHB luminosities unless otherwise noted. The helium luminosity becomes less dependent on the core mass as the core exhausts.

$$\begin{aligned} L_{He}(\text{ZAHB},\ Y_c=0.95) &\sim M_c^{4.6} \\ L_{He}(Y_c=0.50) &\sim M_c^{3.4} \\ L_{He}(Y_c=0.05) &\sim M_c^{2.7} \end{aligned} \quad (28)$$

The HB lifetimes τ_{HB} from the models of Sweigart and Gross (1975) are found to obey the empirical relation,

$$\tau_{HB} \sim L_{He}^{-0.65\pm0.05} \cdot L_H^{-0.15\pm0.05} . \quad (29)$$

Since τ_{HB} is proportional directly to the amount of core exhausted and inversely to the helium luminosity, one can conclude that the exhausted region is dependent upon M_c (otherwise $\tau_{HB} \sim L_{He}^{-1}$). This region, estimated from either the convective core mass M_{cc} or the extent of the semi-convective zone M_{sc}, also varies like L_{He} with evolutionary stage.

$$M_{cc}(\text{ZAHB}) \sim M_c^{1.3\pm0.1} \quad (30)$$

$$M_{cc}(\text{max}) \sim M_c^{1.0\pm0.1} \quad (31)$$

$$M_{sc}(\text{max}) \sim M_c^{0.55\pm0.05} \quad (32)$$

For my models which were calculated with various values of G, the size of the convective core was not influenced by G. Thus, I shall assume as I have done on the main sequence that the amount of material burned on the HB is independent of G.

For an individual star which has evolved from the GB, the net effect of G on the HB is surprisingly small. Recalling

the effect of G upon the core mass at the helium flash (equation 19), the resulting HB luminosity is almost independent of G.

$$L_H \sim G^{0.0\pm0.6} \tag{33}$$

$$L_{He} \sim G^{-0.4\pm0.9} \tag{34}$$

As mentioned before, the effective temperature as measured relative to the GB of these HB models is not significantly changed by G. If the amount of helium consumed on the HB is independent of G as is the convective core, then the HB lifetimes can be determined by (i) finding the dependence of τ_{HB} on M_c and (ii) dividing by the G dependence of the helium burning. The effect of G on the HB lifetimes is similar to that on the GB lifetimes.

$$\tau_{HB} \sim G^{-2\pm1} \tag{35}$$

The adopted HB evolutionary tracks for the STD and BDI models exhibit G-variations only so far as my variable-G calculations extend. The HB track up to helium core-exhaustion for the 1.0 $M_\odot$ STD model is listed in table 5. The HB tracks for the other models use the 1.0 $M_\odot$ track which is rescaled uniformly in (i) time via equation (29), (ii) luminosity via equations (26) and (27) and (iii) effective temperature relative to the particular model's giant branch. Since I did not calculate any models beyond helium core-exhaustion, the continuation of the HB--the asymptotic giant branch--is modelled upon Sweigart's (1975) 1.5 $M_\odot$ model with composition (Y,Z) = (0.30,0.02). The extrapolation of the track from $\log(L/L_\odot)$ = 4.1 to 4.4 is based upon the (L, M_c)-relation

derived from Sweigart's 1.5 $M_\odot$ and 3.5 $M_\odot$ model sequences.

$$L/L_\odot = 55500 \cdot (M_c/M_\odot - 0.474) \quad (36)$$

This asymptotic GB track, which is given in table 6, is attached onto the end of the HB track. It is not modified for differences in G or stellar mass because of insufficient data.

§6. The Detection of $G \neq G_0$ through Stars

When comparing stars of the same mass at equivalent evolutionary phases, the changes induced by G seem quite substantial. This effect is most apparent in the luminosity where $L \sim G^{6-7}$ on the main sequence, $L \sim G^{7-10}$ on the giant branch, and $L \sim G^{3-7}$ on the horizontal branch. The effective temperature of the models is also affected by G, but not as strongly, $T_{eff} \sim G^{0.5-1.5}$. Unfortunately, when viewing the main sequence or giant branch of a cluster of stars, these differences all but disappear. With a larger G the main sequence shifts parallel to itself upwards in luminosity and towards the blue so that it appears as a slightly more massive main sequence. Although the luminosity of the giant branch is increased with G, the core mass at the helium flash is reduced. Thus, the luminosity at the tip of the giant branch is barely changed. The horizontal branch also shows a shift to the blue and an increase in luminosity with G. The luminosity increase is nullified by the reduced helium core mass, and the color relative to the giant branch with the same value of G remains unchanged.

Although these changes in luminosity with G will be difficult to observe in a cluster of stars, they do induce a substantial change in the time scales of stellar evolution which may be detectable. The main sequence lifetime of a star is reduced by the increase in luminosity. Relative to a star of the same mass, the high-G star has a much shorter lifetime, $\tau \sim G^{-6.6}$; and relative to the higher mass star which it is imitating on the main sequence, it still has a reduced lifetime, $\tau \sim G^{-2\pm1}$. This reduction in the main sequence lifetime carries over to the giant branch and the horizontal branch lifetimes which exhibit similar G-dependences.

All of these effects combine to make the detection of a value of $G \neq G_0$ into a most difficult task. Suppose we are able to observe a detailed color-magnitude diagram of an old cluster of solar-type stars which--unknown to us--has a higher value of $G > G_0$. Unable to determine the actual mass at the turn-off, we will deduce a larger turn-off mass from the higher luminosity. The appearance of the main sequence will be similar to the standard clusters. Likewise, the giant branch and horizontal branch will appear normal. Even the relative number distribution of stars will be the same as in standard clusters since the apparent ages scale as $\tau \sim G^{-2}$ for all phases of evolution. Thus, in order to discern the effects caused by a variable G, we must have a set of absolute calibrations of mass, composition and luminosity.

TABLE 1. THE EXPONENTIAL VARIATION OF STELLAR QUANTITIES

	with M:		with G:	
	models	homology	models	homology
L	4.6-4.8	4.5-4.9	6.0-6.9	6.3-7.0
T_c	0.7	0.7-0.8	1.1-1.4	1.1-1.4
P_c	0.7-0.9	0.7-1.3	1.8-2.2	1.6-2.5

TABLE 2. G-EFFECTS ON THE GIANT BRANCH AT A FIXED CORE MASS

Quantity	Variation
Total Luminosity	$L \sim G^{10} \rightarrow L \sim G^{7}$ *
Neutrino Losses	$L_{\nu} \sim G^{14\pm1}$
Gravitational Contraction	$L_{G} \sim G^{11\pm3}$
Central Temperature	$T_{c} \sim G^{2.0\pm0.5}$
Central Density	$\rho_{c} \sim G^{3.5\pm0.5}$

* Decreases smoothly up to core flash

TABLE 3. GIANT BRANCH MODELS AT HELIUM CORE FLASH

M/M_θ	Age(Gyr)	$\log T_{eff}$	$\log \frac{L}{L_\theta}$	M_c/M_θ	$\log G/G_0$	$X_{env.}$
1.0 STD	12.832	3.4594	3.365	0.47394	0.0	0.7073
1.2 STD	6.458	3 4709	3.363	0.47325	0.0	0.7078
0.9 BDI	15.612	3.4538	3.370	0.47755	-0.00139	0.7096
1.1 BDI	6.221	3.4661	3.360	0.45847	+0.00945	0.7086

TABLE 4. THE GIANT BRANCH IN THE INTERVAL

$LOG(L/L_\theta) = 2.0 \rightarrow 3.0$

Model	M_{core}/M_θ	$\Delta\tau$(Myr)	$\delta(\log\Delta\tau)$	log G/G_0
1.0/1.2 M_θ STD	0.289→0.403	27.77	0.0	0.0
0.9 M_θ BDI	0.290→0.405	27.99	+0.0034	-0.0014
1.1 M_θ BDI	0.280→0.391	27.01	-0.0122	+0.0095

TABLE 5. 1.0 $M_\odot$ HORIZONTAL BRANCH TRACK

$(M_c, Y_{env}, Z_{env}) = (0.474, 0.27, 0.02)$

ZAHB: $(\log L_H/L_\odot, \log L_{He}/L_\odot) = (1.53, 1.13)$

Age(Myr)	$\log L/L_\odot$	$\log T_{eff}$	$\Delta\log T_{eff}$*
0.0	1.680	3.6140	+0.0182
16.0	1.675	3.6148	0.0187
32.0	1.675	3.6156	0.0195
48.0	1.675	3.6164	0.0203
64.0	1.680	3.6172	0.0214
72.0	1.690	3.6163	0.0211
80.0	1.700	3.6153	0.0208
85.0	1.720	3.6135	0.0202
90.0	1.755	3.6102	0.0193
92.5	1.785	3.6074	0.0184
95.0	1.830	3.6034	0.0173
97.0	1.910	3.5963	0.0154
99.0	1.820	3.6043	0.0175
100.0	1.870	3.5999	0.0163
101.0	2.010	3.5873	0.0136
101.9	2.489	3.5461	0.0088

* $\Delta\log T_{eff} = (\log T_{eff})_{HB} - (\log T_{eff})_{GB}$ at the same luminosity.

TABLE 6. ASYMPTOTIC GIANT BRANCH

Age(Myr)	log $L/L_\odot$	δlog T_{eff}
0.000	2.49	≡0.0000
2.335	2.35	+0.0124
6.433	2.50	-0.0010
7.490	2.60	-0.0098
8.248	2.70	-0.0190
8.814	2.80	-0.0282
9.230	2.90	-0.0376
9.498	3.00	-0.0469
9.702	3.10	-0.0567
9.877	3.20	-0.0670
10.060	3.30	-0.0769
10.255	3.40	-0.0867
10.469	3.50	-0.0964
10.698	3.60	-0.1059
10.901	3.70	-0.1147
11.065	3.80	-0.1233
11.316	3.90	-0.1313
11.614	4.00	-0.1359
11.939	4.10	-0.1402
12.263	4.20	-0.1419
12.587	4.30	-0.1427
12.912	4.40	-0.1435

III. References

Bahcall, J.N. and R.L. Sears 1972, Ann.Rev.Ast.& Ap., 10, 25.

Castellani, V., P. Gianonne and A. Renzini 1971, Ap.& Space Sci., 10, 340.

Cox, A.N. and J.N. Stewart 1970, Ap.J.Suppl.No.174, 19, 243.

Dicke, R.H. and P.J.E. Peebles 1965, Space Sci.Rev., 4, 419.

Dirac, P.A.M. 1938, Proc.R.Soc., A165, 199.

Ezer, D. and A.G.W. Cameron 1966, Can.J.Phys., 44, 593.

Fowler, W.A., G.R. Caughlan and B.A. Zimmerman 1975, O.A.P., 380.

Gamow, G. 1967, Proc.N.A.S., 57, 187.

Henyey, L.G., J.E. Forbes and N.L. Gould 1964, Ap.J., 139, 306.

Pochoda, P. and M. Schwarzschild 1964, Ap.J., 139, 587.

Robertson, J.W. and D.J. Faulkner 1972, Ap.J., 171, 309.

Roeder, R.C. 1967, Ap.J., 149, 131.

Roeder, R.C. and P. Demarque 1966, Ap.J., 144, 1016.

Schwarzschild, M. 1958, Structure and Evolution of Stars, (New York: Dover).

Shaviv, G. and J.N. Bahcall 1969, Ap.J., 155, 135.

Sweigart, A. 1975, private communication.

Sweigart, A. and P. Gross 1975, paper in preparation.

Teller, E. 1948, Phys.Rev., 73, 801.

Tinsley, B.M. 1972, Ap.J.(Letters), 174, L119.

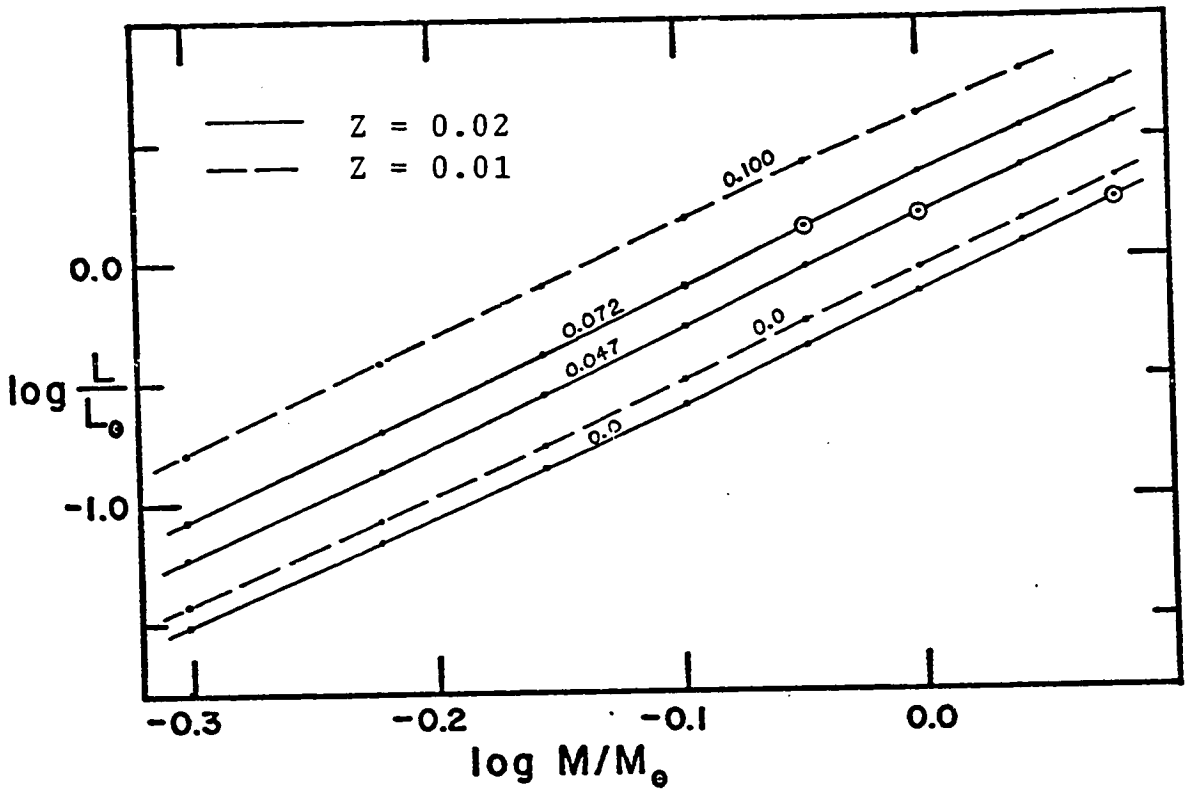

Fig.1.---ZAMS log L vs.log M. The mass-luminosity relationship for 5 different series of ZAMS is shown for two metallicities: (Y,Z) = (0.25,0.02) and (Y,Z) = (0.25,0.01). Each line is labelled with the value of $\log(G/G_0)$.

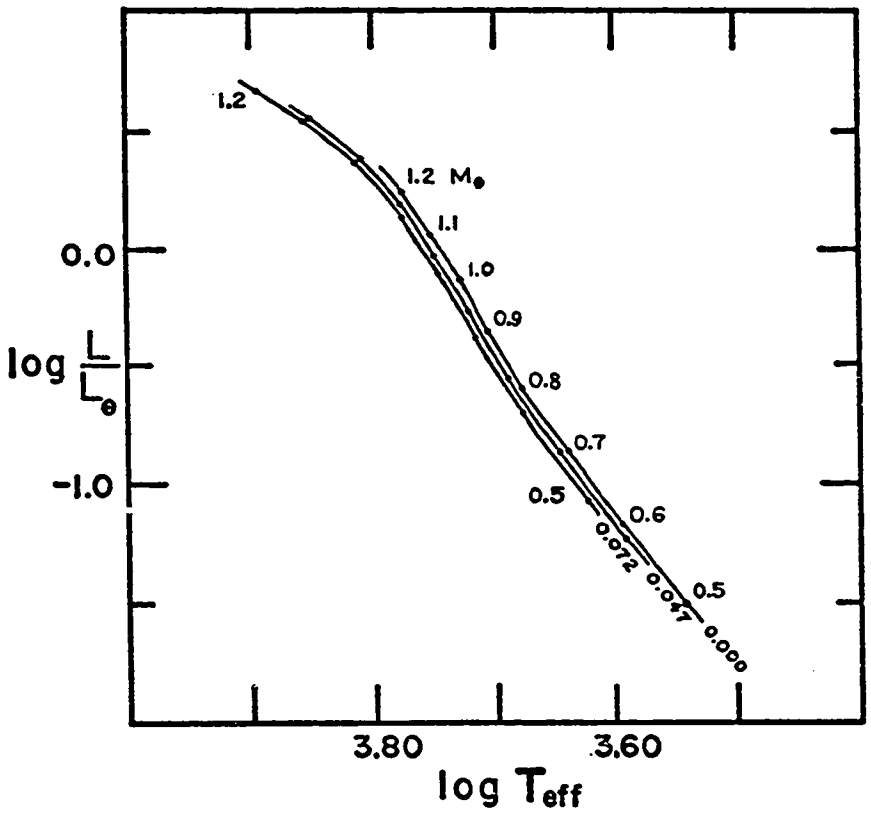

Fig.2.---ZAMS log L vs. log T_{eff}. The zero-age main sequence for composition (Y,Z) = (0.25,0.02) is shown for the mass range 0.5-1.2 M_θ. Each ZAMS is labelled with the value of $\log(G/G_0)$.

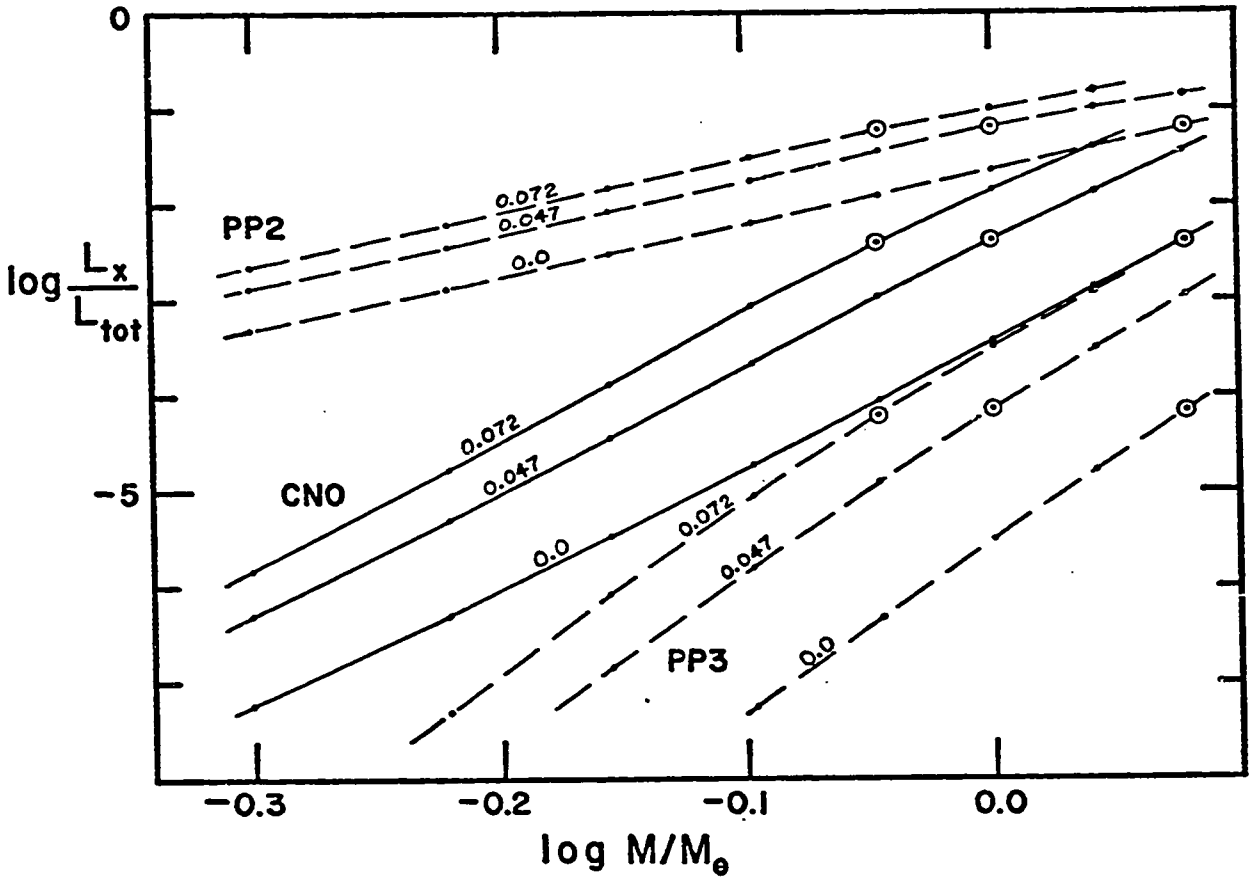

Fig.3.---Fractional luminosity due to PP2, PP3 and CNO energy cycles as a function of the stellar mass. The same three ZAMS are used and labelled as in Fig. 2.

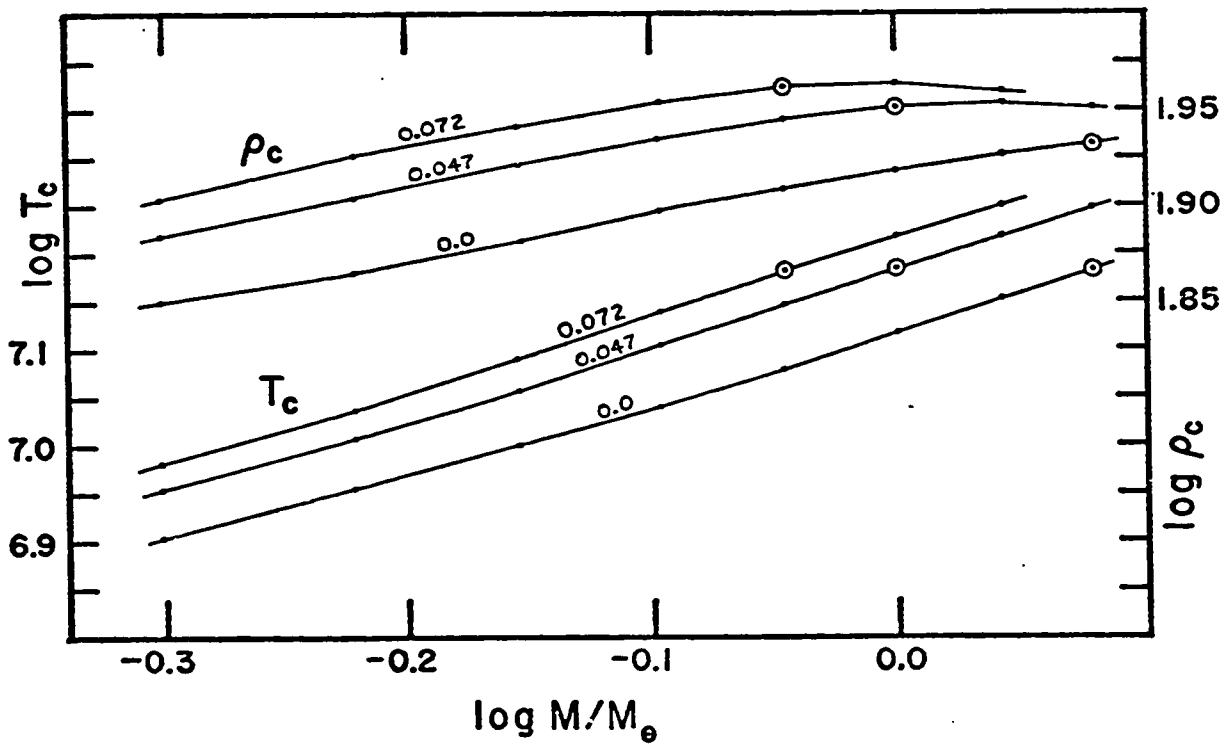

Fig.4.---Central density and temperature as a function of stellar mass. The same three ZAMS are used and labelled as in Fig. 2.

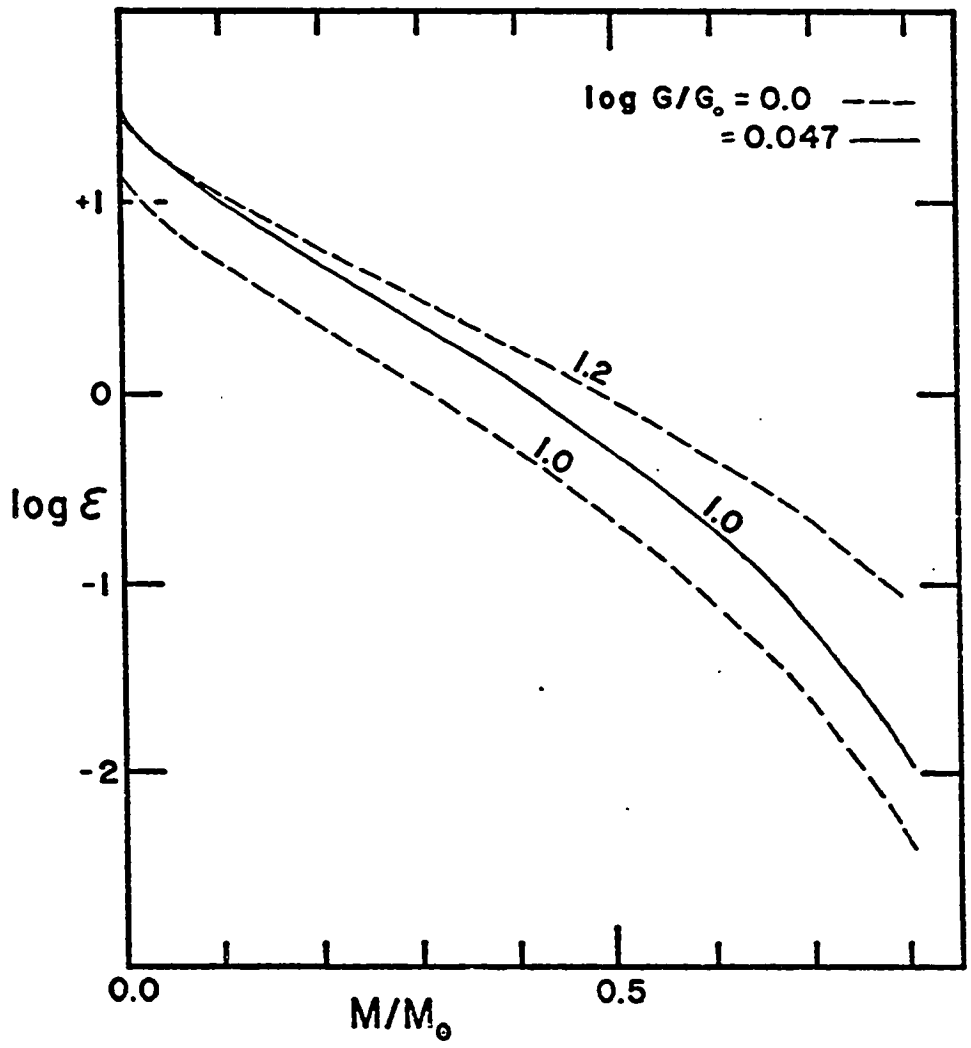

Fig.5.---ZAMS energy generation ε throughout the interior of the star. The value of log ε as a function of the interior mass is plotted for the 1.0 and 1.2 $M_\odot$ STD stars (log G/G_0 = 0.0) and for the 1.0 $M_\odot$ BDI star (log G/G_0 = +0.047).

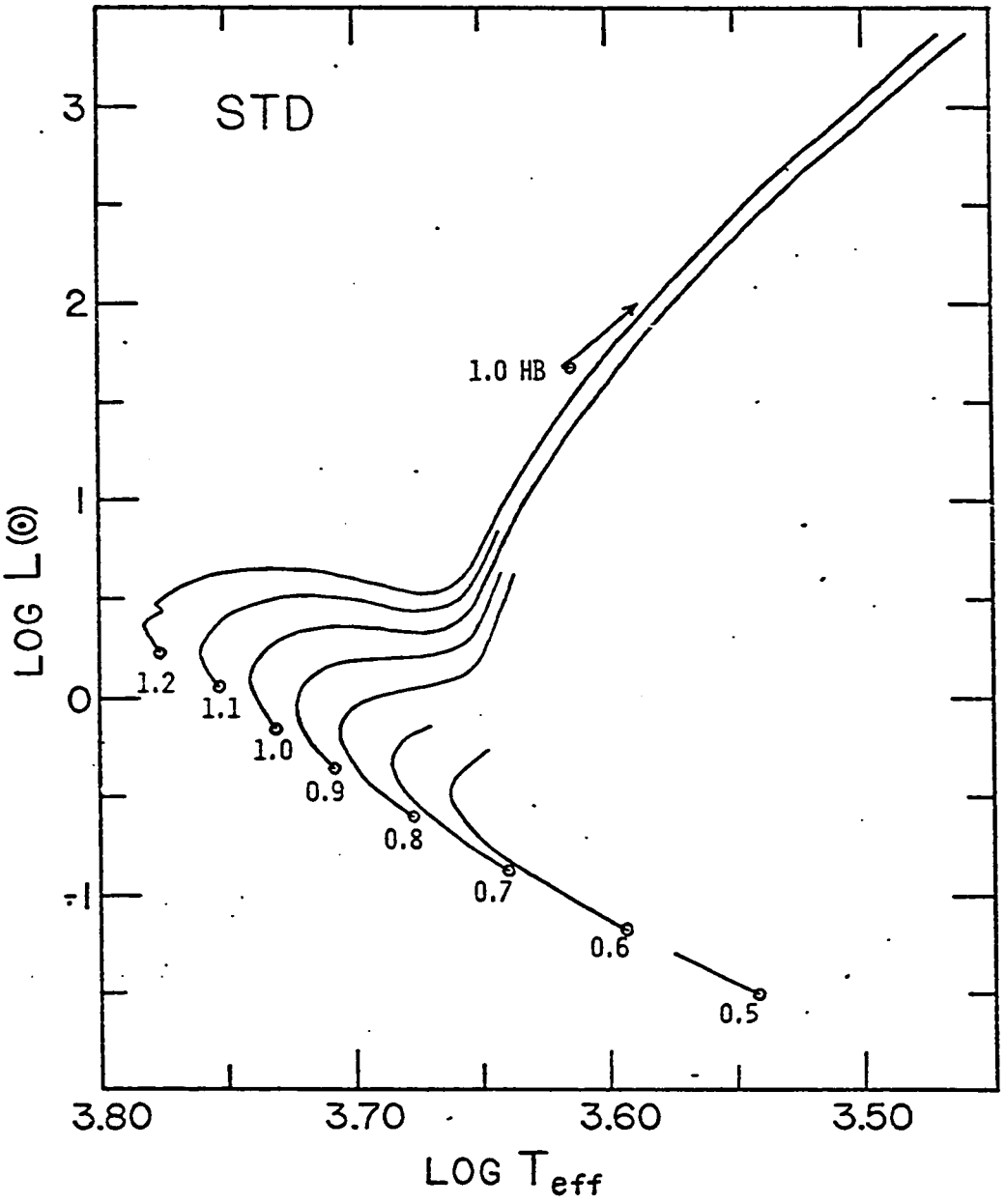

Fig.6.---The (log L, log T_{eff})-diagram for the STD tracks. The stellar mass range is 0.5-1.2 $M_\odot$ in intervals of 0.1 $M_\odot$, and the composition is (Y,Z) = (0.25,0.02). The stars are evolved with a constant G = G_0.

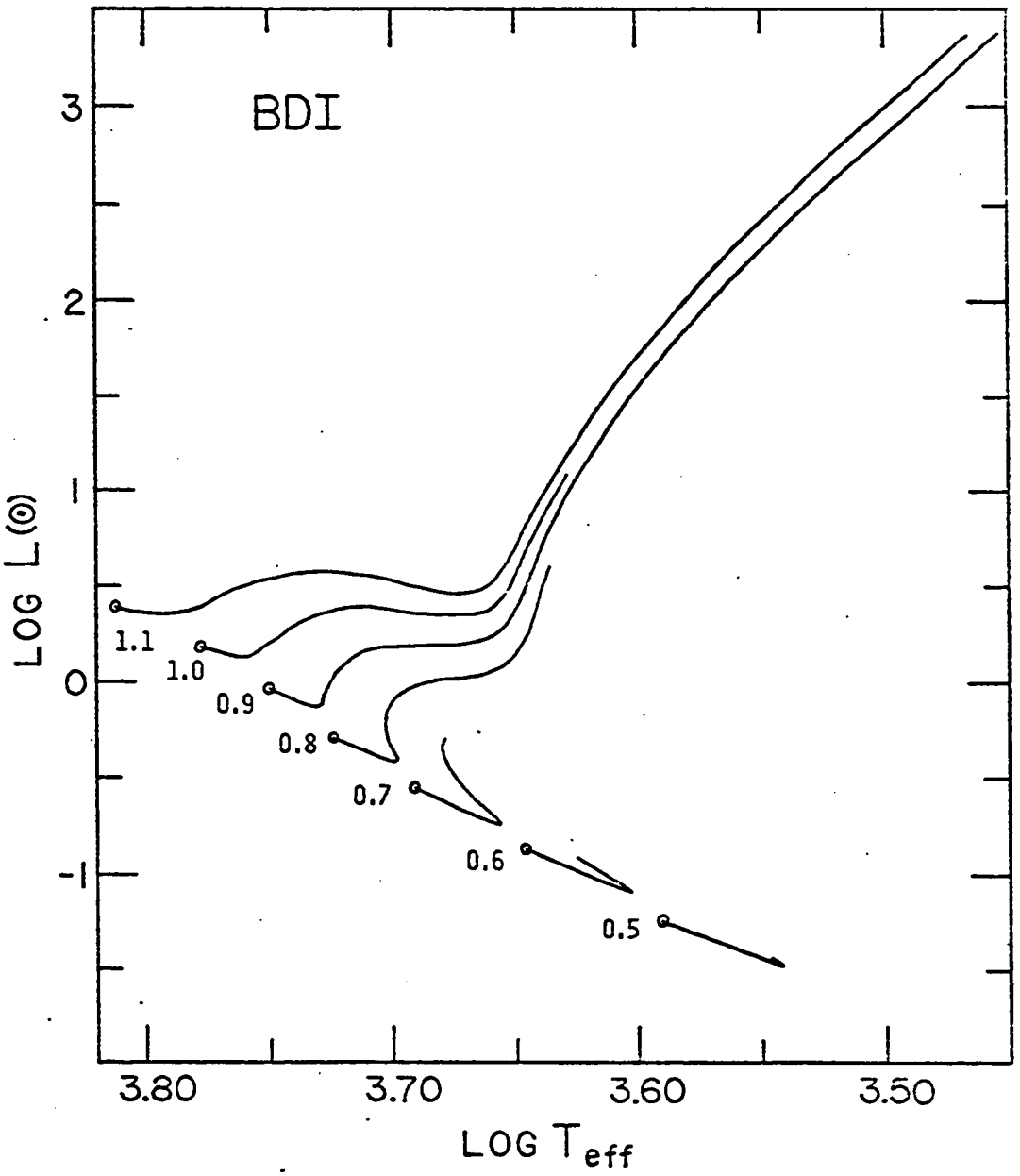

Fig.7.---The (log L, log T_{eff})-diagram for the BDI tracks. The stellar mass range is 0.5-1.1 M_θ in intervals of 0.1 M_θ, and the composition is (Y,Z) = (0.25,0.02). The stars are evolved from a redshift of z = 5 in a Brans-Dicke universe with ω = 6, H_0 = 55 km/s/Mpc and Ω = 0.20.

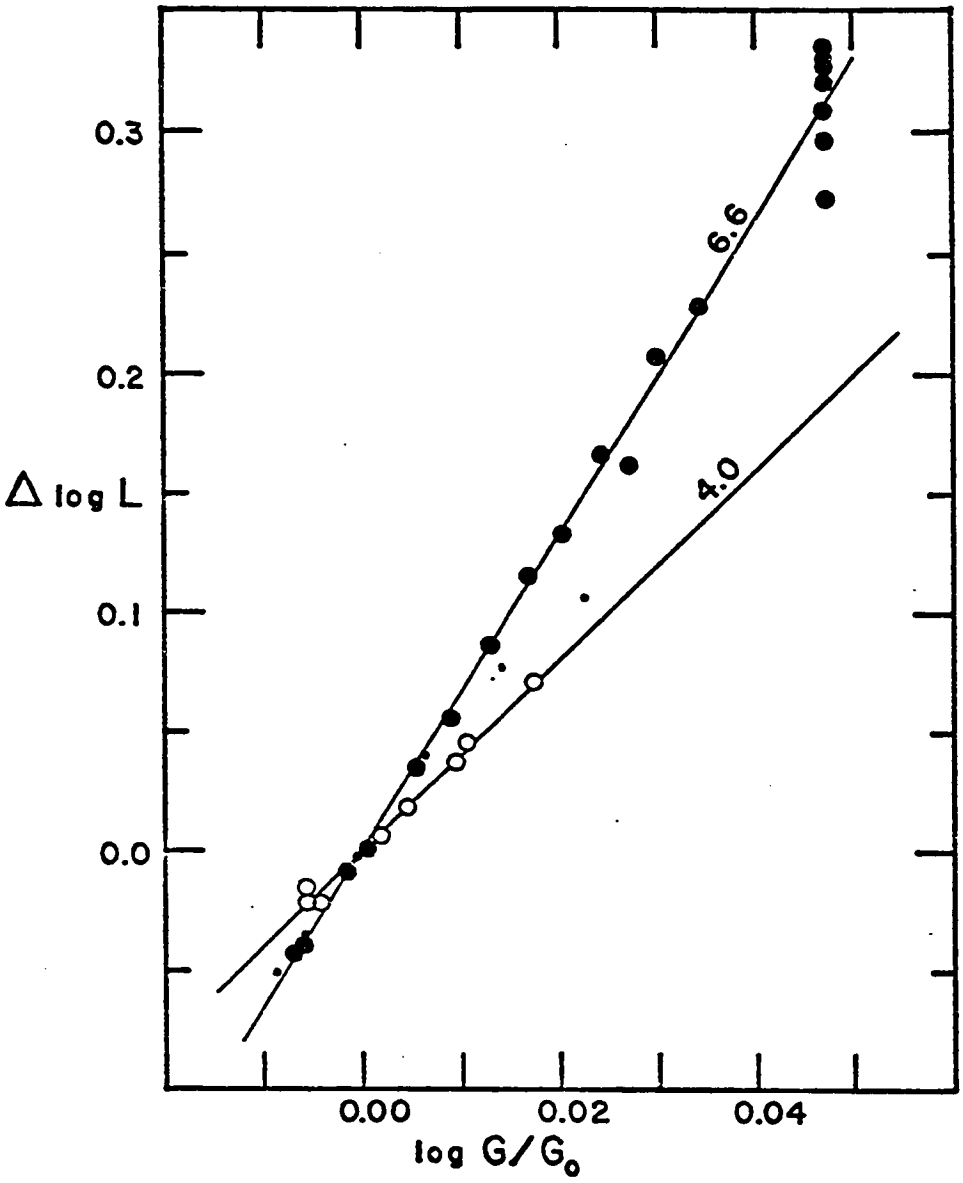

Fig.8.---Increase in log L as a function of log G/G_0. The difference in luminosity is calculated by comparing the BDI and STD models at the equivalent evolutionary phase from the ZAMS to the base of the giant branch. The large dots represent models with $X_c > 0.20$; the open circles, $X_c < 0.01$; the small dots, intermediate values. The solid lines depict the hypothetical relationships $L \sim G^{6.6}$ & $L \sim G^{4.0}$.

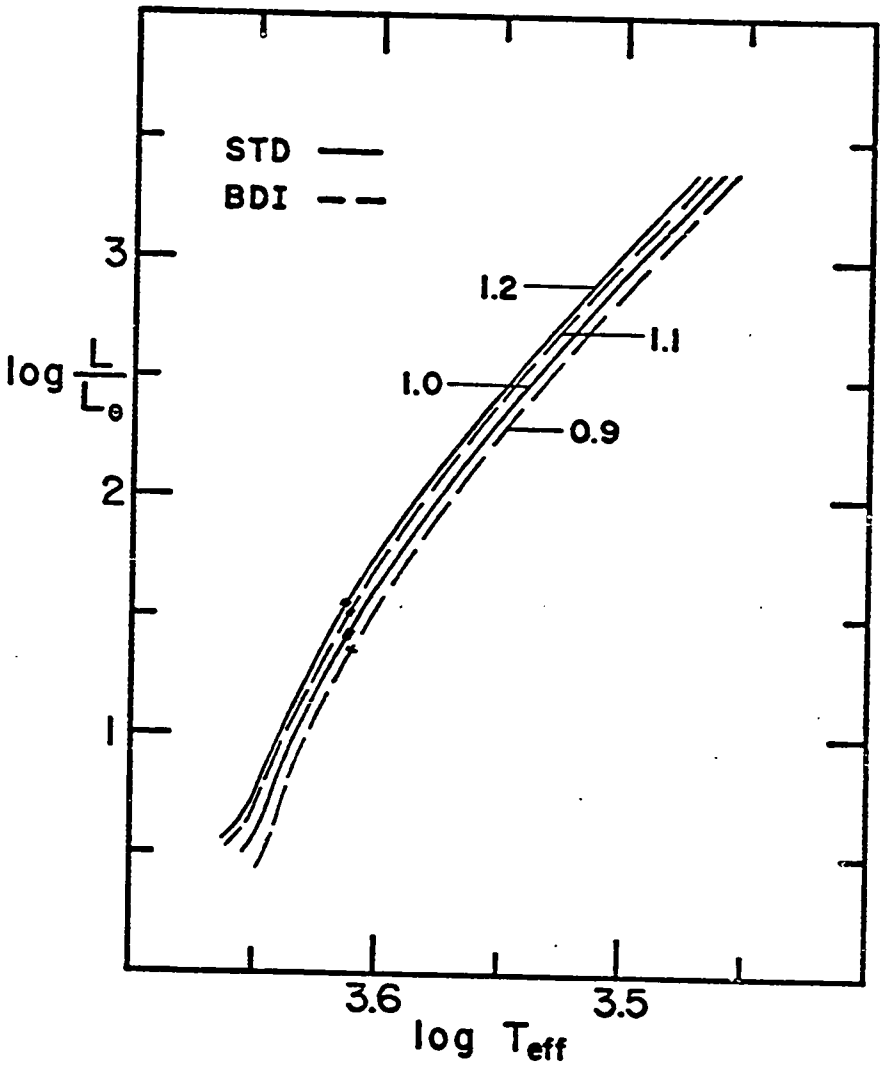

Fig.9.---The (log L, log T_{eff})-diagram of the giant branches. The giant branches of the 1.0 & 1.2 M_θ STD models and the 0.9 & 1.1 M_θ BDI models are shown. The thickened line on each giant branch is where the luminosity dips as the hydrogen shell meets the composition discontinuity in the envelope. A helium core flash occurs at the top of each giant branch.

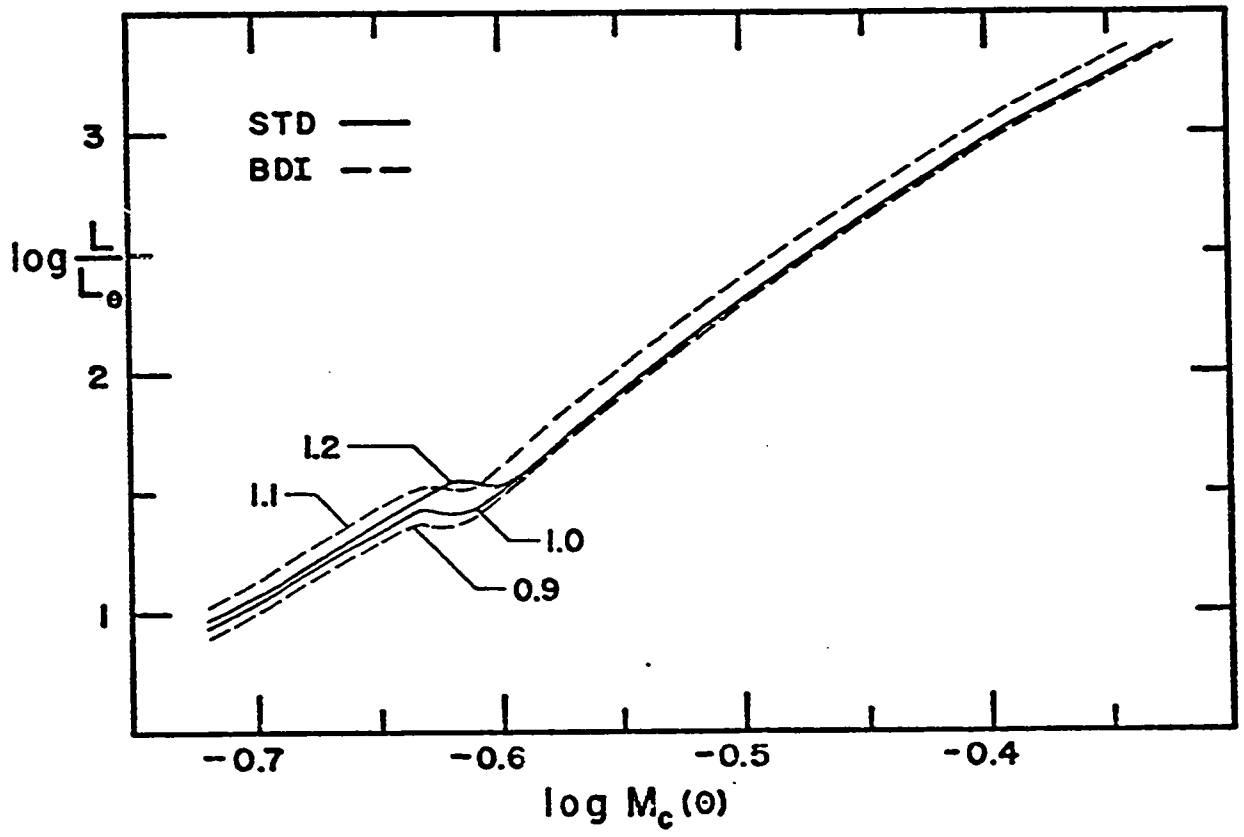

Fig.10.---The (luminosity, core mass)-relationship for the four giant branches of Fig. 9.

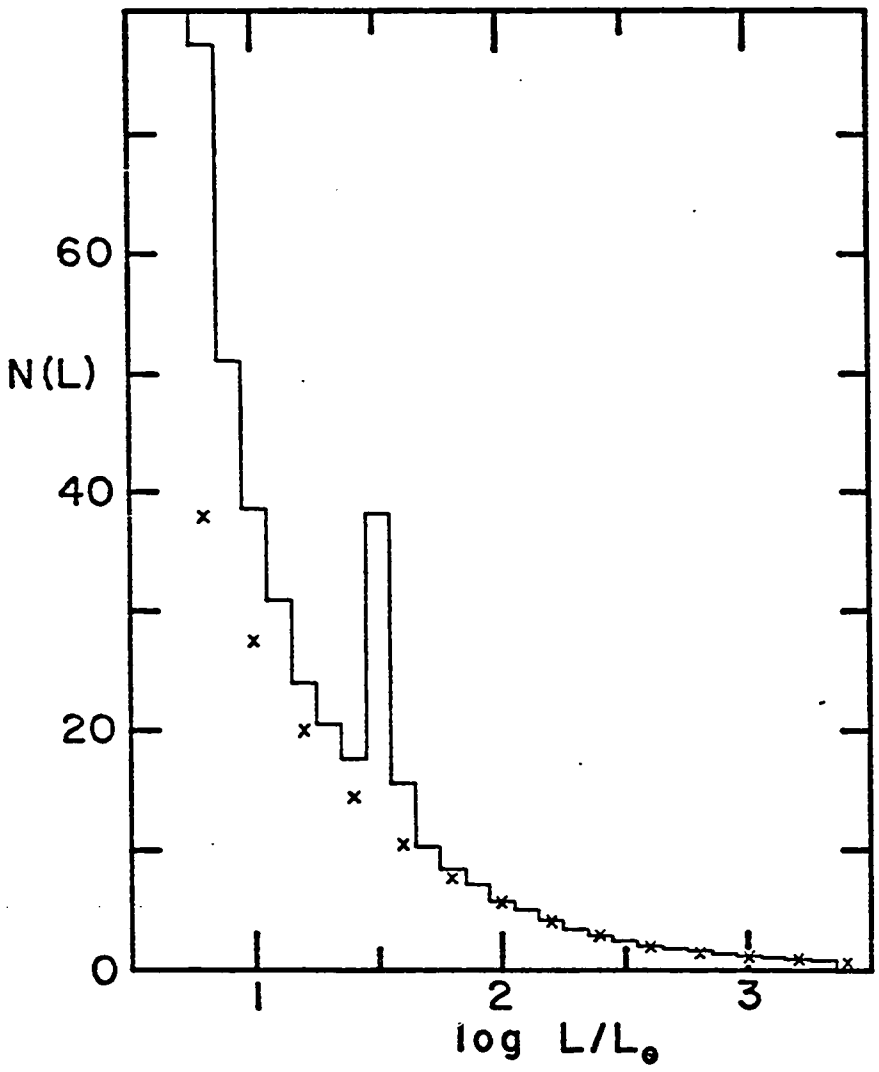

Fig.11.---Giant branch luminosity function. N(L) is the expected number of giant stars per unit interval in log L. The scale of N(L) is arbitrary. The peak about log L/L_{θ} = 1.5 is caused by the luminosity dip described in Fig. 9. The solid line is calculated from the times of the actual 1.2 M_{θ} giant branch track, and the X's represent the theoretical form $N(L) \sim L^{-0.7}$.

CHAPTER IV. GLOBULAR CLUSTERS AND DECREASING G

§1. The Limitations of Globular Clusters

The globular clusters may show the greatest effect of a decreasing G since they are among the oldest stellar population in our galaxy. They represent a static population in that one cannot view their evolution (i.e., at large redshifts). At the present epoch, however, one can observe a detailed HR diagram with a numerically significant distribution of stars which provides luminosity functions and details of the main sequence turn-off.

The giant branch and the horizontal branch will not show effects from a higher G in the past since all of these stars have evolved from the main sequence at a comparatively recent epoch where $G \approx G_0$. Once a star has reached the giant branch with a degenerate helium core and a uniform hydrogen envelope, any previous history of a larger G has disappeared. The variations observed in the horizontal branch are more complex and cannot be due simply to a larger G in the past (e.g., varying composition, rotation, binaries, mass loss).

The main sequence turn-off and the sub-giant branch may show the effects of a decreasing G. The turn-off and the sub-giant regions are affected by the manner of hydrogen-core exhaustion which may in turn be influenced by the integrated effect of a larger G in the past.

§2. The Evolutionary Tracks

In order to examine the main sequence turn-off and the sub-giant branch, I have computed a series of tracks from the zero-age main sequence to the base of the giant branch. The tracks cover the mass range 0.7-0.9 $M_\odot$ for the metal-poor composition (Y,Z) =(0.25,0.0001). The stellar evolution code is described in Appendix A and uses the energy generation rates of Fowler, Caughlan and Zimmerman (1975) and the opacities of Cox and Stewart (1970).

The STD tracks, computed with $G = G_0$, are shown in figure 1, and the key evolutionary points are listed in table 1. The BDI tracks are computed for a Brans-Dicke universe with H_0 = 55 km/s/Mpc, Ω = 0.20, ω = 6 and a redshift birthtime of $z_{birth} = 5$, which gives a birthtime of t_{birth} = 1.521 Gyr and a universe age of t_0 = 15.16 Gyr (see Chapter II). The variation of G is computed from

$$\log(G/G_0) = 0.0271508 \cdot s + 0.0201262 \cdot s^2,$$

where $s \equiv \log(t_0/t)$. These variable-G tracks are shown in figure 2 and listed in table 2. For the BDI tracks the decrease in luminosity due to a decreasing G is overcome by the evolution-induced increase in luminosity which occurs about $X_{center} \approx 0.5$.

§3. The Isochrones

Synthesized globular clusters from the STD and BDI tracks are computed for universe models with H_0 = 55 km/s/Mpc and

$\Omega = 0.20$ (and with $\omega = 6$ for the BDI model). The clusters are assumed to have formed at a redshift of $z_{birth} = 5$ which gives present cluster ages of 13.5 Gyr (STD) and 13.6 Gyr (BDI).

For these hypothetical clusters I have used the isochrone method described in Appendix B. I have assumed a constant initial mass function which gives a uniform distribution of stars in each mass interval. This assumption is valid in the region of interest for a large range of non-constant--but continuous--initial mass functions because all the stars from the turn-off to the base of the giant branch have approximately the same mass. The isochrones for the present-day STD and BDI models are shown in figures 3 and 4, respectively. The thickness of the line from the turn-off to the giant branch is proportional to the expected number of stars in that region. (The thickness will depend, of course, on the plotting scale.) There appears no obvious difference in the distribution of stars across the sub-giant branch except that the BDI cluster looks older than the STD cluster.

A more detailed examination of these clusters in the sub-giant region can be made with the luminosity and color functions which are calculated by the isochrone program. The luminosity function--the number of stars at a given luminosity L per unit interval in log L--is shown for a range of ages for both the STD and BDI models in figures 5 and 6, respectively. The color function--the number of stars at a given

effective temperature per unit interval in log T_{eff}--is shown for the same range of ages for both models in figure 7 and 8. Considering both the luminosity and color functions, there is little difference between the STD and BDI models which cannot be ascribed to a difference in apparent age. For example, the present-day BDI model at 13.6 Gyr looks like the STD model at an age of 16.8 Gyr.

§4. The Effects of a Varying G on Stars

While the isochrones demonstrate the difference in apparent age between the STD and BDI models, an examination of the stellar models can yield more detailed information. I shall isolate those effects of a varying G which are independent of the cosmological model.

Initially, it was postulated that the core exhaustion of a star might be affected by a higher value of G in its past history. One can examine the core exhaustion by looking at the energy generation rate ε throughout the interior of the star since the hydrogen exhaustion is proportional to ε. The zero-age main sequence values of ε for the 0.8 $M_\odot$ BDI model and for the 0.8 and 0.9 $M_\odot$ STD models are plotted in figure 9 as a function of the interior mass. The increase in G for the BDI model ($\log G/G_0 = +0.0472$) does not make the 0.8 $M_\odot$ model behave like a higher mass star, but rather just scales up ε by a constant factor throughout the star. Thus, the manner of core exhaustion will not be affected, but the

time scales up to the exhaustion of the hydrogen core will decrease as G--and hence ε--increases.

The density of stars observed on the sub-giant branch of a globular cluster is determined by the time interval which a star takes to cross from the turn-off to the giant branch. By defining the sub-giant crossing time as

$$t_{SG} \equiv t(M_c = 0.200) - t(X_c = 0.0002),$$

a comparison can be made with the data in tables 1 and 2. The 0.8 M_θ BDI model has experienced a larger G in the past but crosses the sub-giant branch at approximately the present epoch ($G \approx G_0$). The times for the two 0.8 M_θ models,

$$\begin{aligned} t_{SG} &= 1.179 \text{ Gyr (BDI)} \\ &= 1.182 \text{ Gyr (STD)} , \end{aligned}$$

are equal to within the error caused by the finite time step between models which is $\Delta t \approx 0.04$ Gyr at core exhaustion.

Thus, with the exception of the difference in apparent age, the region about the turn-off and the sub-giant branch of a globular cluster which is observed at the present epoch will be independent of the previous history of G. These results may not be applicable to larger mass, metal-rich stars where the CNO-PP energy generation balance may be changed by a larger G, causing the appearance of a large convective core and thus altering the hydrogen core exhaustion.

A varying G may affect the luminosity and effective temperature of stars in globular clusters to an extent which may be observable at the present time. The luminosity of the stellar models increases with G as is shown in figure 10

where $\Delta\log L$ is plotted against $\log(G/G_0)$. The value of $\Delta\log L$ is the increase/decrease in luminosity of a variable-G stellar model as compared with the standard model of the same mass at the equivalent evolutionary phase. The core hydrogen burning models follow $L \sim G^{6.6}$. The later phases of evolution ($X_c < 0.01$) have no well defined relationship but are less steeply dependent on G ($L \sim G^4$). Previous high-G values do not affect subsequent evolution since the ($\Delta\log L$, $\log G/G_0$)-relation passes through the origin. The effective temperature is not strongly affected by G which can be seen by examining tables 1 and 2: $T_{eff} \sim G^1$. As G approaches G_0, any difference in T_{eff} disappears. Thus, at the present epoch ($G=G_0$) these observable quantities (L, T_{eff}) become indistinguishable from the standard values.

§5. The Turn-off Mass

The only detectable difference between the STD and BDI models of globular clusters is the apparent age, or rather, the stellar mass at the main sequence turn-off. The higher G of the BDI models speeds up stellar evolution and reduces the turn-off mass. Since the increase in luminosity with G is uniform throughout the star, the hydrogen fuel burns out faster and the star ages more quickly. The evolution time scale of an individual star varies inversely with this increase in luminosity. Thus, for variable-G cosmologies one can define an evolution time τ_{ev} which includes the integrated effect of a varying G,

$$\tau_{ev}(\tau) \equiv \int_{t_{birth}}^{\tau+t_{birth}} (G/G_0)^{\alpha} \cdot dt,$$

where $L \sim G^{\alpha}$.

Using the luminosity dependence $L \sim G^{6.6}$ determined in §4, the evolution times and hence, the turn-off masses for the BDI cosmological model can be predicted and compared with the stellar models. In the calculation of $\tau_{ev}(\tau)$ for the BDI model, the integration is carried into the future ($G<G_0$) until $\tau_{ev} > 25$ Gyr, which is the turn-off age for the 0.7 $M_\odot$ STD model. The STD models were used to determine the (log τ, log M_{t-o})-relationship,

$$\log(M_{t-o}/M_\odot) = 0.220 - 0.270 \cdot \log \tau(\text{Gyr}).$$

The $\tau_{ev}(\tau)$-relation for the BDI case was then applied to predict the (log τ, log M_{t-o}(BDI))-relationship. The results are shown in figure 11.

The agreement of the BDI stellar models with the predictions is quite good but gives a better fit with $L \sim G^{7.0}$. This difference is induced by the method of evolving the star whereby the energy generation rates of the old, converged model are used to advance the composition of the model. For the case of a decreasing G, the new model which has a lower G will have lower burning rates, and the true time step between models will have been underestimated. The effect on the overall age of the models will be small as long as the chosen time steps allow only small decrements in G. For the calculation of the turn-off masses I shall adopt the true luminosity proportionality $L \sim G^{6.6}$, which will agree with

the ages of the models in the limit of infinitely small time steps.

The present examination of the turn-off masses will be extended to cover a full range of Brans-Dicke cosmological models. For the chosen composition (Y,Z) = (0.25,0.0001), the turn-off mass at the present epoch can be calculated for any variable-G cosmology in which $\tau_{ev}(\tau)$ is known. As is true for the real age τ, the evolution time τ_{ev} in a Brans-Dicke cosmology scales inversely with the Hubble constant, $\tau_{ev} \sim H_0^{-1}$. This evolution time as a function of both the Brans-Dicke coupling constant ω and the fractional closure density Ω is shown in figure 12, where the redshift at stellar formation is fixed $z_{birth} = 5$ and $H_0 = 55$ km/s/Mpc. For the region $3 < \omega < \infty$ and $0.028 < \Omega < 2.0$, I find that $\log \tau_{ev} \sim 1/(1+\omega)$ with the slope becoming steeper for larger Ω. In the general relativistic limit $1/(1+\omega) \to 0$, $\tau_{ev} = \tau$ since $G \equiv G_0$; and in the low density limit $\Omega \to 0$, $\tau_{ev} = \tau = H_0^{-1}$. For $\omega < 6$, τ_{ev} increases as Ω increases since the increase in G more than compensates for the decrease in real age. A most interesting feature occurs in the cross-over region about $\omega \approx 12$ where the value of $\tau_{ev} \approx 15$ Gyr is almost independent of Ω. Table 3 lists the present values of the turn-off mass for this range of (ω, Ω) with $H_0 = 55$ km/s/Mpc, $z_{birth} = 5$ and composition (Y,Z) = (0.25,0.0001). As a second example, by fixing $\omega = 6$ and $H_0 = 55$ km/s/Mpc, the variation of τ_{ev} with z_{birth} is shown in figure 13 for different values of Ω. Table 4 gives the present-epoch turn-off masses for this case

and for the composition (Y,Z) = (0.25,0.0001). For all of the densities considered, the value of the turn-off mass is extremely sensitive to the choice of z_{birth} if $z_{birth} < 4$.

Thus, in all the Brans-Dicke cases, including the special case of general relativity, the turn-off mass of the globular clusters will be strongly dependent upon the redshift at stellar formation. Assuming that z_{birth} can be determined, the turn-off mass for low-density universes ($\Omega<0.1$) will depend mainly on the Hubble constant. This condition also holds in the unusual case of $\omega = 12$ where $\tau_{ev} \approx 15\cdot(55/H_0)$ Gyr for $z_{birth} = 5$. For universes with approximately the closure density ($\Omega\approx1$), the turn-off mass will be a function of all of the cosmological parameters: H_0, Ω and ω.

§6. Conclusions

An attempt to discern the difference between the general theory of relativity and the Brans-Dicke theory is made by comparing the evolution of a globular cluster of constant $G \equiv G_0$ with that of a specific variable-G Brans-Dicke model. In making observations of individual stars in a globular cluster one is limited to nearby clusters and hence, to the present time where $G = G_0$. The only difference which is found between the general relativity and the Brans-Dicke models at the present epoch is that the Brans-Dicke cluster looks older. This difference in the apparent age, or rather, in the stellar mass at the main sequence turn-off, is due to the higher value of G in the past history of the Brans-Dicke models and is a

function of the parameters (H_0, Ω, z_{birth}, ω) of the cosmological model.

In theory the turn-off mass can be determined with a knowledge of the absolute bolometric magnitude, the effective temperature and the surface gravity at the turn-off. With measurements of these quantities, a knowledge of the stellar composition, and a belief in the accuracy of the stellar opacities, the evolution time scale can be computed from the turn-off mass. Supposing that a trustworthy evolutionary age for the globular clusters can be thus derived, there still remains the determination of the parameters of the cosmological model.

Assuming that the Hubble constant and the density of the universe are observationally fixed, the evolutionary age is still very sensitive to the redshift at stellar formation in many cases. Allowing the value of z_{birth} to be determined somehow, the evolutionary age can be used at last to calculate the Brans-Dicke coupling constant ω. However, for low-density universes the effects of a Brans-Dicke theory can barely be detected for even $\omega < 3$. Although it is possible to test Brans-Dicke theory with globular clusters, it is improbable that such tests will be decisive.

TABLE 1. STD MODELS (Y,Z) = (0.25,0.0001)

Mass	Point	Age(Gyr)	log T_{eff}	log $L/L_\odot$
0.9 $M_\odot$	ZAMS	0.0	3.7908	-0.074
	X_c = 0.480	3.055	3.8025	+0.038
	= 0.208	5.693	3.8155	+0.167
	= 0.0002	9.640	3.8505	+0.574
	M_c = 0.20	10.501	3.6981	+1.060
	= 0.22	10.556	3.6900	+1.213
0.8 $M_\odot$	ZAMS	0.0	3.7594	-0.309
	X_c = 0.481	4.554	3.7707	-0.198
	= 0.210	8.728	3.7830	-0.059
	= 0.0002	14.876	3.8049	+0.401
	M_c = 0.20	16.058	3.6954	+0.985
	= 0.22	16.133	3.6890	+1.142
0.7 $M_\odot$	ZAMS	0.0	3.7245	-0.582
	X_c = 0.482	7.233	3.7374	-0.472
	= 0.212	14.356	3.7524	-0.319
	= 0.0002	24.547	3.7723	+0.207

TABLE 2. BDI MODELS (Y,Z) = (0.25,0.0001)

Mass	Point	Age(Gyr)	log T_{eff}	log $L/L_\odot$	log G/G_0
0.9 $M_\odot$	ZAMS	0.0	3.8576	+0.226	+0.0472
0.8 $M_\odot$	ZAMS	0.0	3.8116	-0.003	+0.0472
	X_c = 0.480	2.859	3.7925	-0.063	+0.0205
	= 0.209	6.076	3.7935	+0.004	+0.0100
	= 0.0002	11.704	3.8073	+0.409	+0.0017
	M_c = 0.20	12.883	3.6953	+0.989	+0.0006
	= 0.22	12.957	3.6889	+1.147	+0.0006
0.7 $M_\odot$	ZAMS	0.0	3.7732	-0.270	+0.0472
	X_c = 0.481	4.871	3.7507	-0.382	+0.0130
	= 0.211	11.071	3.7550	-0.303	+0.0023
	= 0.0002	21.413	3.7694	+0.188	-0.0042
	M_c = 0.20	23.171	3.6952	+0.860	-0.0048
	= 0.22	23.281	3.6901	+1.023	-0.0049

TABLE 3. TURN-OFF MASSES FOR BRANS-DICKE COSMOLOGY

$(Y,Z) = (0.25,0.0001)$, $H_0 = 55$ km/s/Mpc, $z_{birth} = 5$

	Ω = 0.028	0.200	0.600	1.000	2.000
ω = 3	0.791	0.744	0.689	0.662	0.633
6	0.796	0.776*	0.757	0.750	0.746
12	0.800	0.797	0.799	0.804	0.821
∞	0.805	0.822†	0.848	0.868	0.902

* BDI case
† STD case

TABLE 4. TURN-OFF MASSES FOR BRANS-DICKE COSMOLOGY

$(Y,Z) = (0.25,0.0001)$, $H_0 = 55$ km/s/Mpc, $\omega = 6$

z_{birth}	Ω = 0.028	0.200	1.000	2.000
2	0.848	0.835	0.814	0.811
3	0.821	0.804	0.781	0.777
4	0.806	0.787	0.762	0.758
5	0.796	0.776*	0.750	0.746
6	0.790	0.768	0.741	0.737
8	0.781	0.758	0.730	0.726
10	0.776	0.751	0.722	0.718

* BDI case

IV. References

Cox, A.N. and J.N. Stewart 1970, Ap.J.Suppl.No.174, 19, 261.

Fowler, W.A., G.R.Caughlan and B.A. Zimmerman 1975, O.A.P., No. 380.

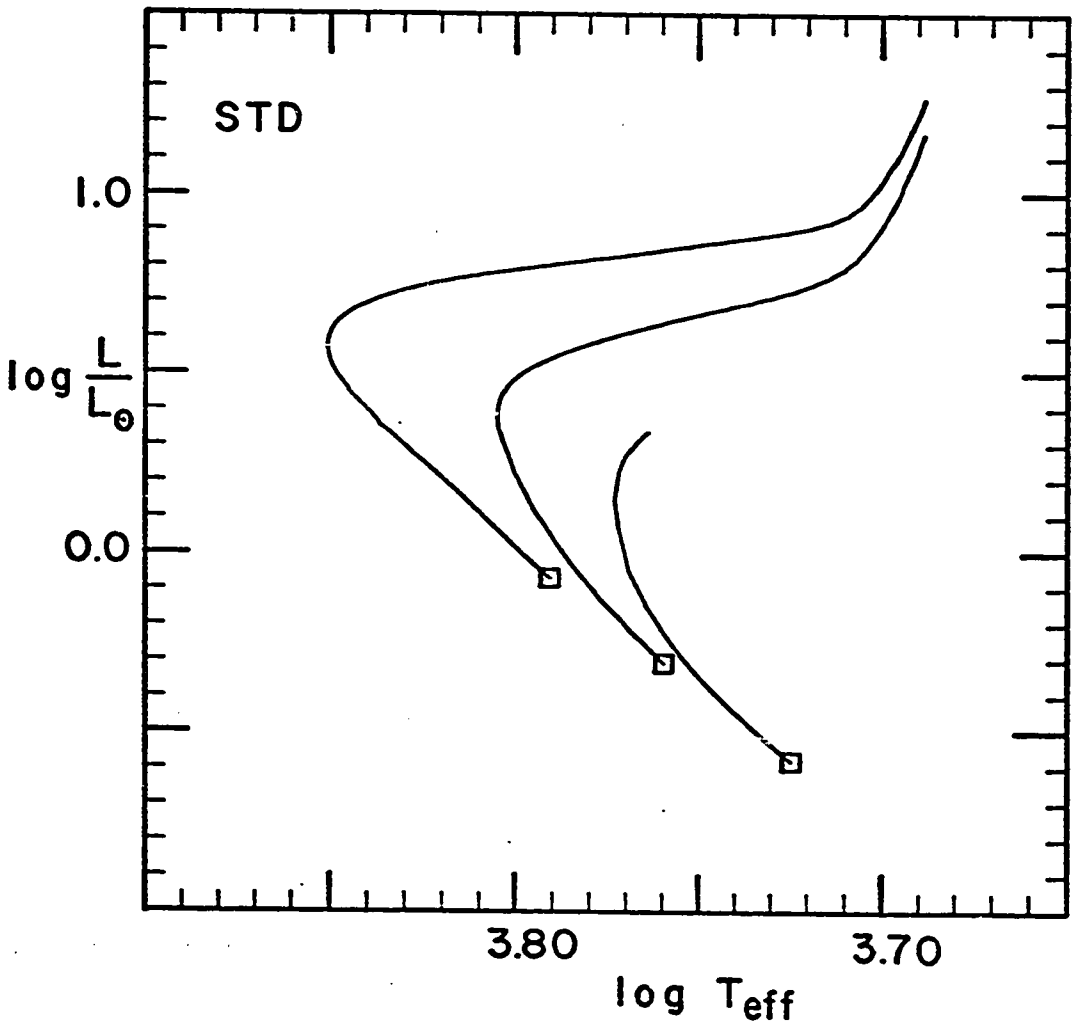

Fig.1.---Log $L/L_\odot$ vs. log T_{eff} for STD models. The evolution from the zero-age main sequence (box) to the base of the giant branch is shown for 0.7, 0.8 and 0.9 $M_\odot$ models with composition (Y,Z) = (0.25,0.0001) and G = G_0.

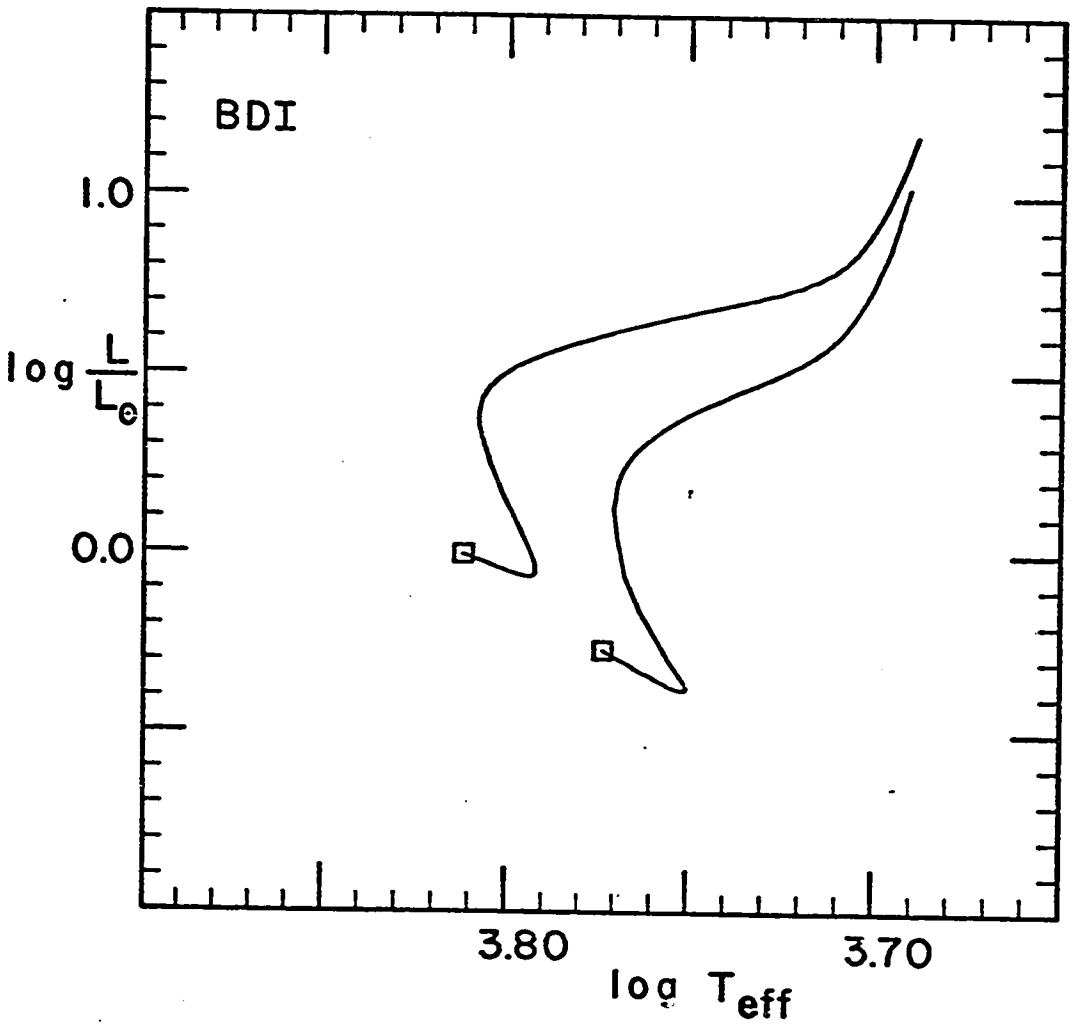

Fig.2.---Log $L/L_\odot$ vs. log T_{eff} for BDI models. The evolution from the ZAMS (box) to the base of the GB is shown for 0.7 and 0.8 $M_\odot$ models with composition (Y,Z) = (0.25,0.0001). The BDI models assume a Brans-Dicke cosmology with $\omega = 6$, $H_0 = 55$ km/s/Mpc, $\Omega = 0.20$ and $z_{birth} = 5$.

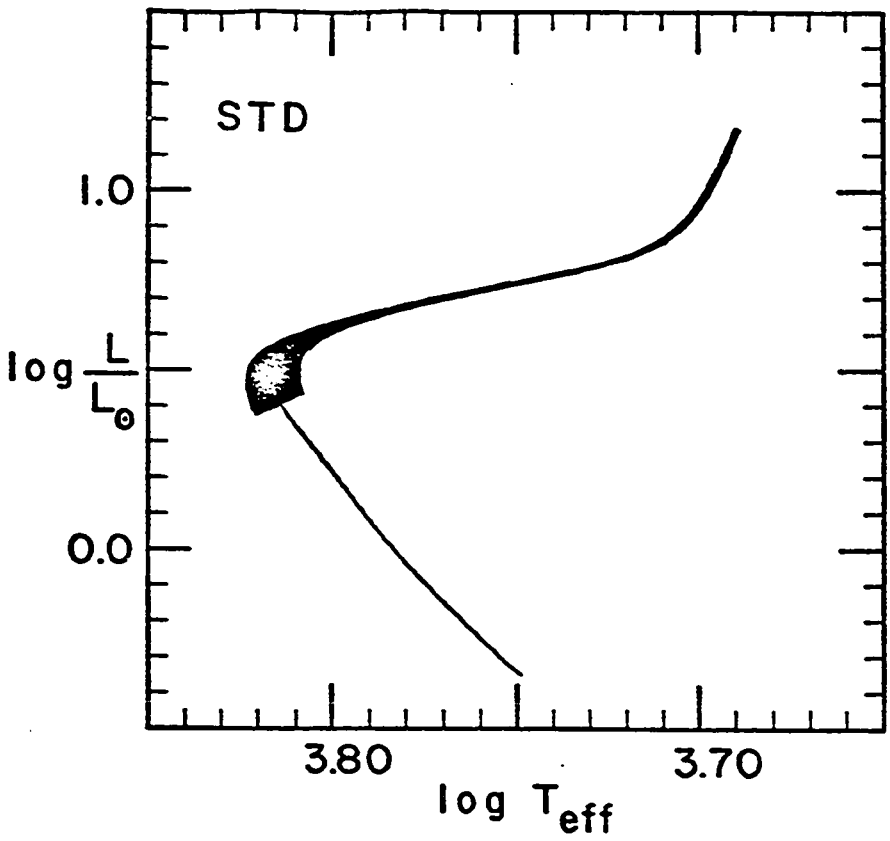

Fig.3.---Isochrone of STD cluster. The present appearance of a cluster of composition (Y,Z) = (0.25,0.0001) is shown in the (log L, log T_{eff})-diagram. The cluster is assumed to have formed at redshift z_{birth} = 5 in a general relativistic universe with H_0 = 55 km/s/Mpc and Ω = 0.20 which corresponds to an age of 13.5 Gyr. The thickness of the isochrone above the turn-off is proportional to the expected number density of stars for a constant initial mass function.

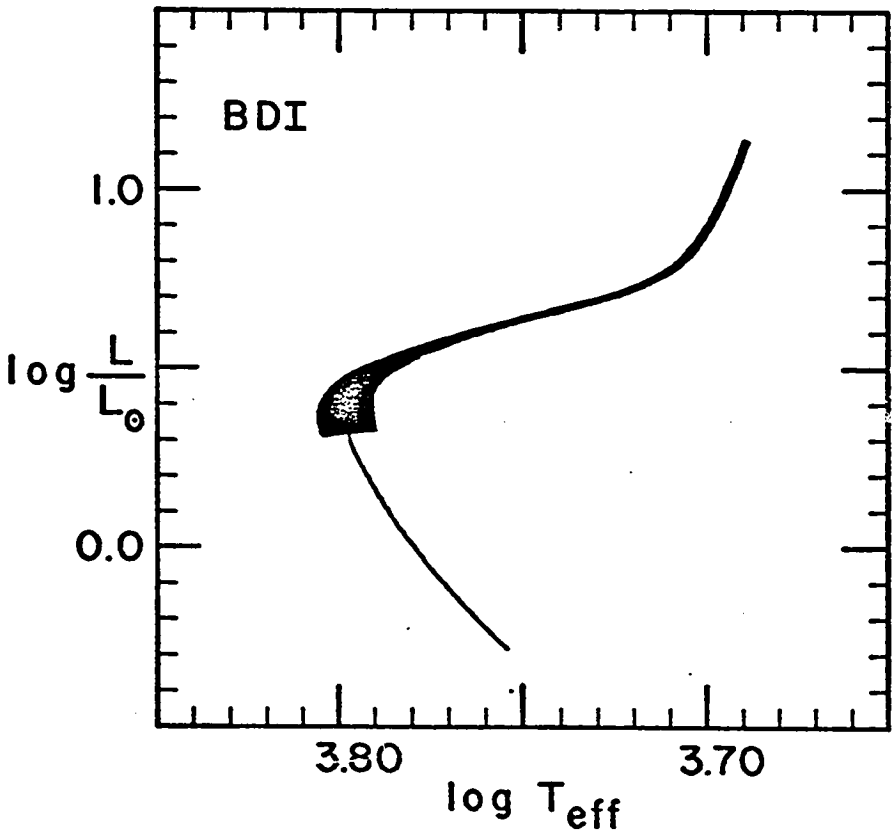

Fig.4.---Isochrone of BDI cluster. This figure is the same as Fig. 3 except that a Brans-Dicke cosmology with $\omega = 6$ is assumed which corresponds to an age of 13.6 Gyr.

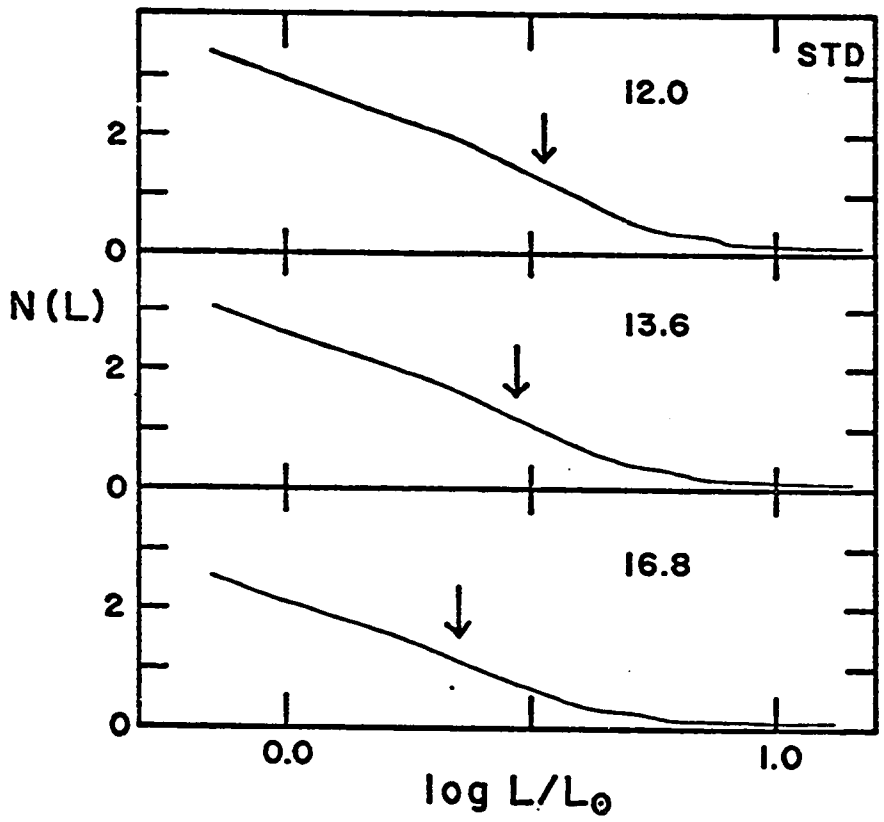

Fig.5.---Luminosity functions for STD metal-poor cluster. The expected number of stars per unit interval in log L (N(L) has an arbitrary scale) is plotted as a function of $\log(L/L_\odot)$ for a constant initial mass function. The ages in Gyr of the hypothetical clusters are given in each box and the arrows denote the luminosity at the maximum log T_{eff}.

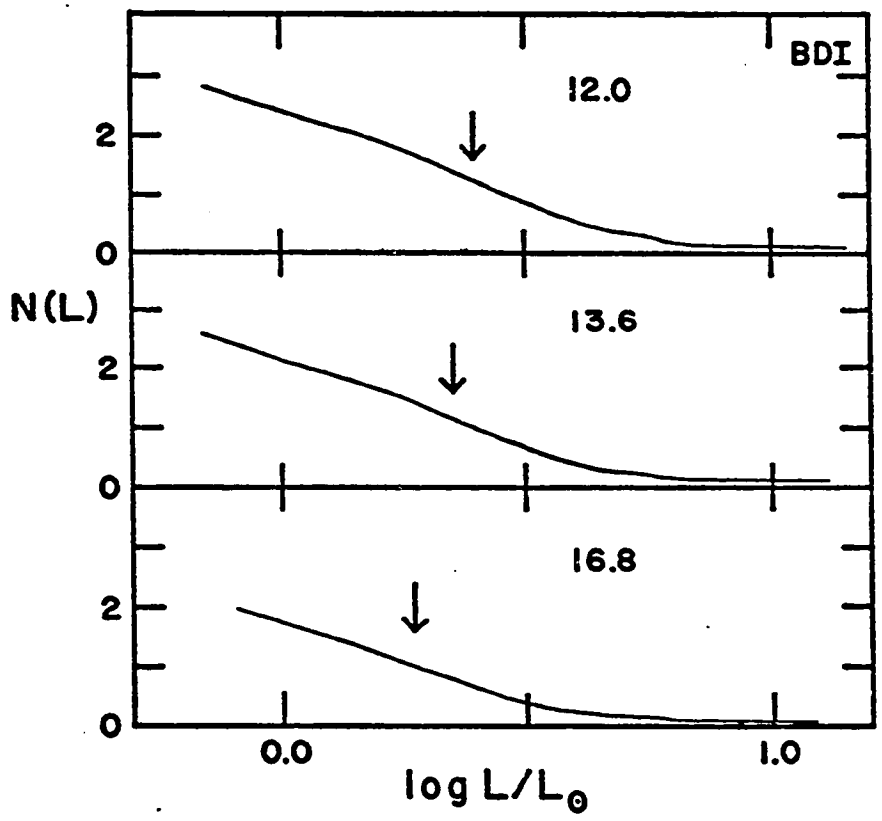

Fig.6.---Luminosity functions for BDI metal-poor clusters. This figure is the same as Fig. 5 but uses the BDI models.

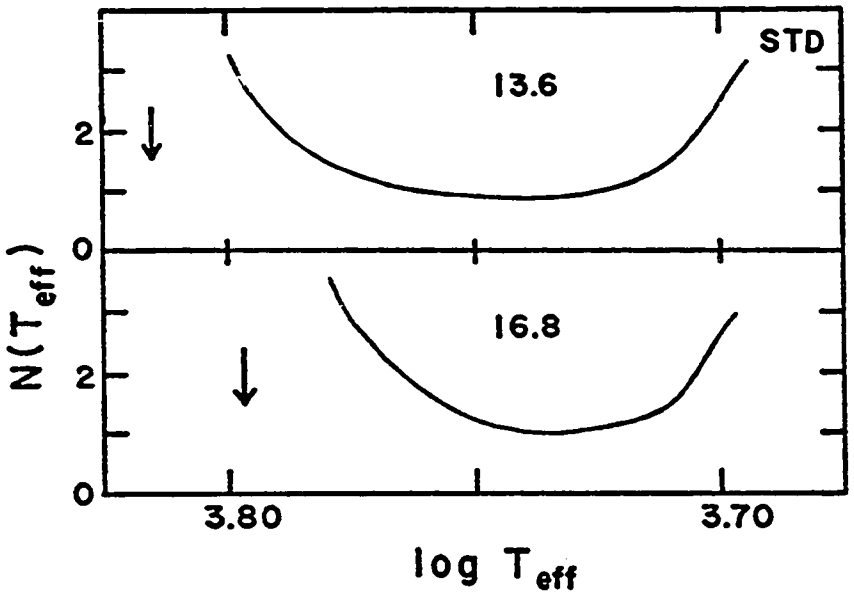

Fig.7.---Color functions for STD metal-poor clusters. The expected number of stars across the sub-giant branch (from the turn-off to the base of the giant branch) per unit interval in log T_{eff} is plotted against log T_{eff}. The scale of $N(T_{eff})$ is arbitrary. The ages in Gyr of the cluster is given in each box and the point of maximum T_{eff} is denoted by an arrow. The initial mass function is assumed to be constant.

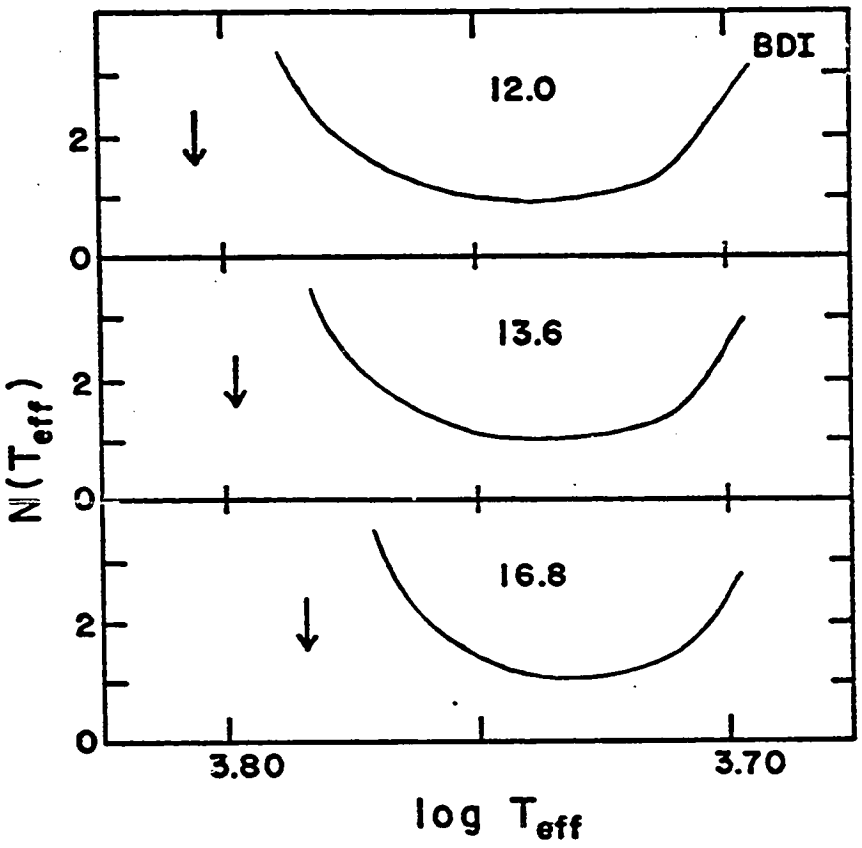

Fig.8.---Color functions for BDI metal-poor clusters. This figure is the same as Fig. 7 but uses the BDI models.

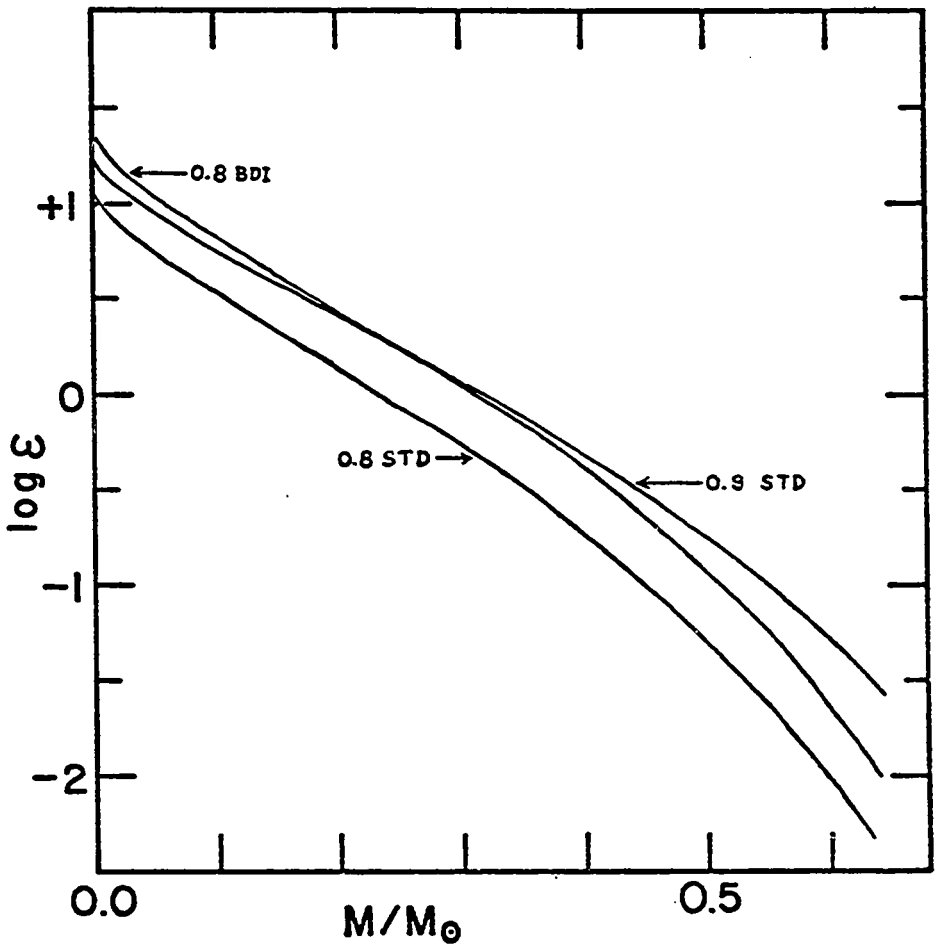

Fig.9.---Log ε vs. M/M_θ. The log of the energy generation rate ε (erg/gm/s) throughout the ZAMS model is plotted as a function of the interior mass. Two STD models (0.8 and 0.9 M_θ) and one BDI model (0.8 M_θ) of composition (Y,Z) = (0.25,0.0001) are shown.

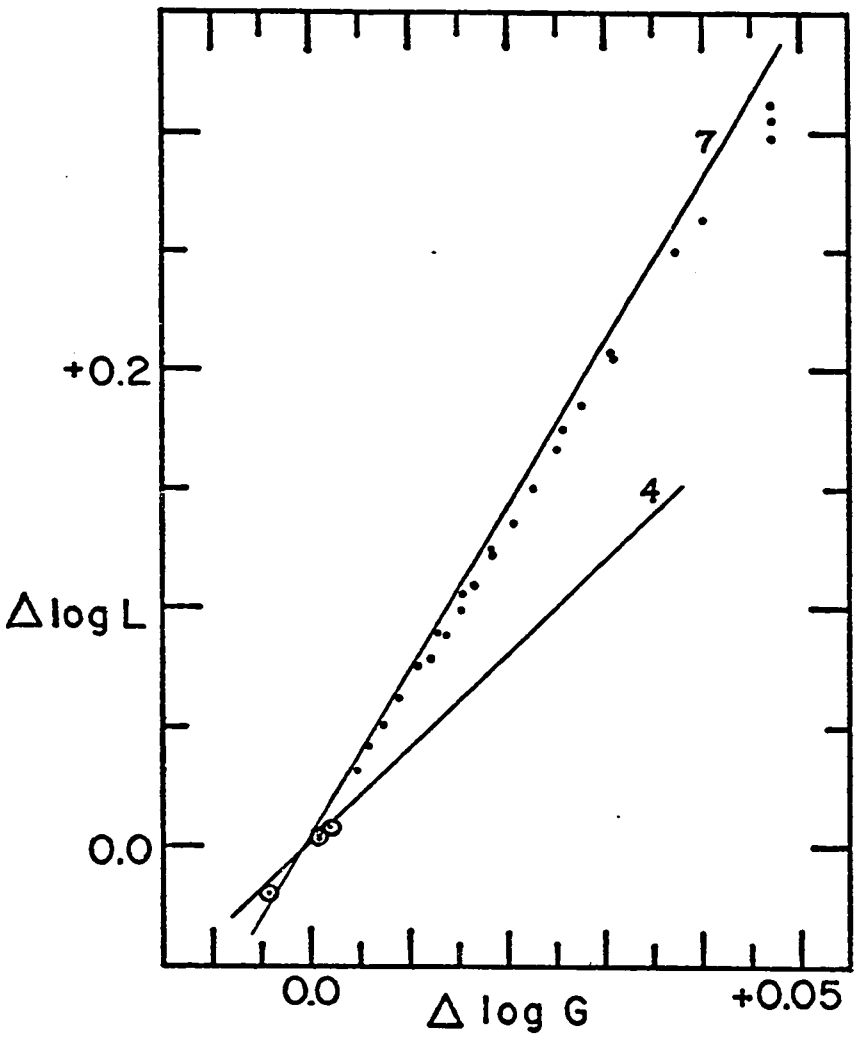

Fig.10.---Δlog L vs. Δlog G. The change in log L is plotted against $\log(G/G_0)$ for models of composition (Y,Z) = (0.25,0.0001). The value of Δlog L is determined by comparing the BDI models with the STD models which are at an equivalent evolutionary phase. The dots represent models with $X_c > 0.10$; the circled dots, $X_c < 0.01$. For comparison, lines showing the relationships $L \sim G^7$ and $L \sim G^4$ are drawn and so labelled.

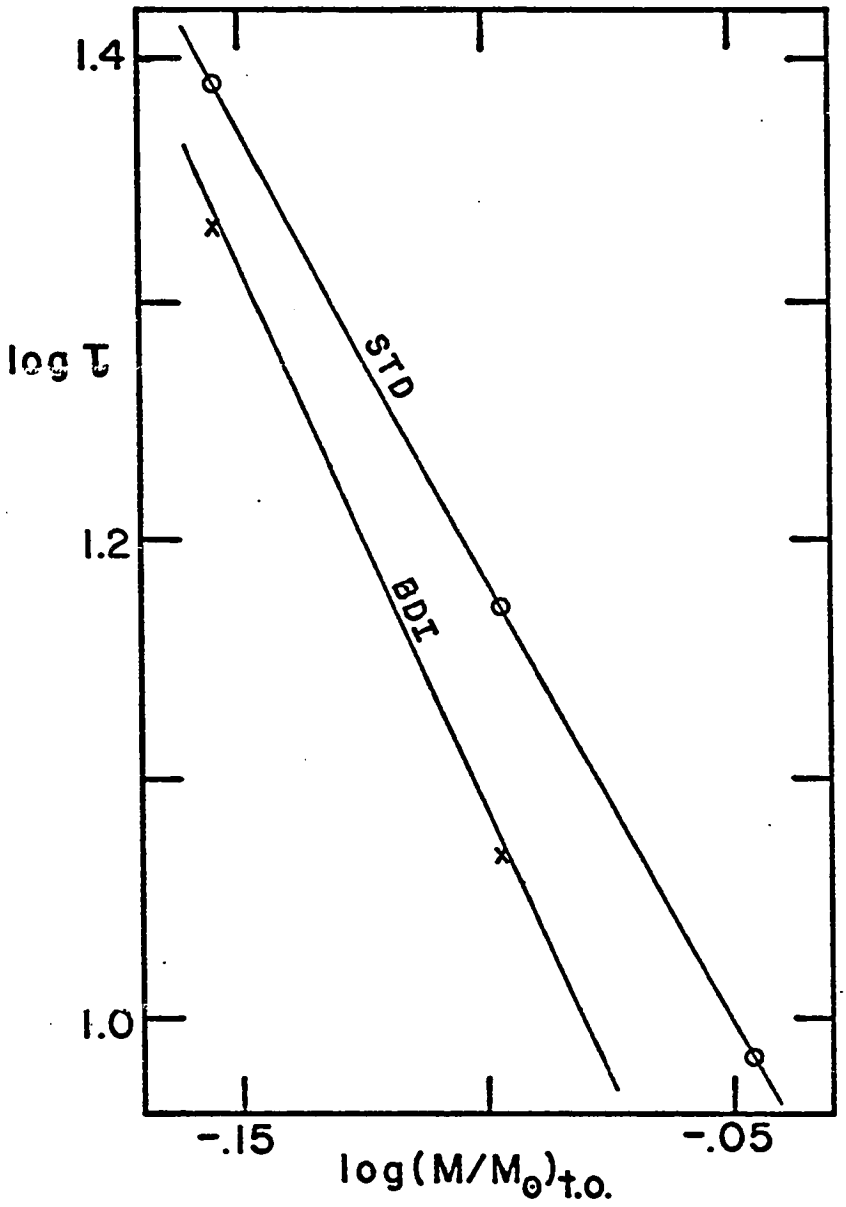

Fig.11.---Log τ(Gyr) vs. log($M/M_\odot$) at the turn-off for (Y,Z) = (0.25,0.0001) models. The turn-off point is defined as X_c = 0.0002 and corresponds roughly to the maximum T_{eff}. The STD age-mass relationship is so labelled. The STD models are plotted as circles and the BDI models as X's. The line labelled BDI is the relationship predicted from the STD values and from the estimated BDI evolution time defined as $\tau_{BD} \equiv \int (G/G_0)^{6.6}\, dt$.

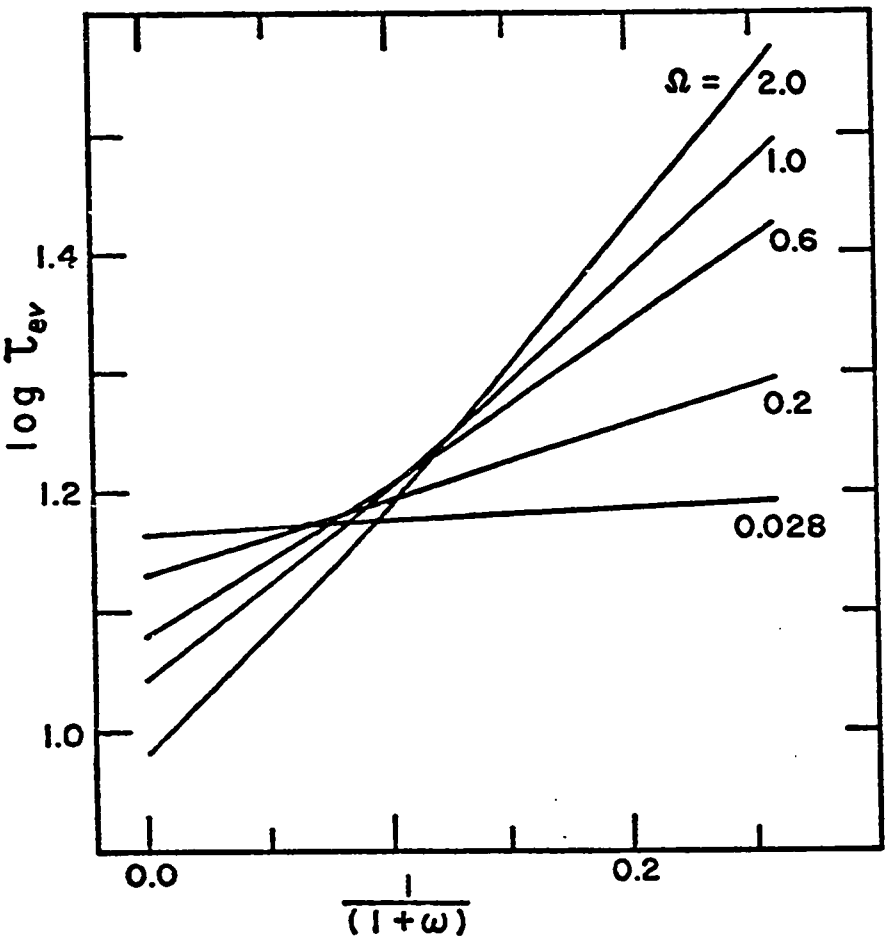

Fig.12.---Log τ_{ev}(Gyr) vs. $1/(1+\omega)$. The evolution time, as defined by $\tau_{ev} \equiv \int_{z_b}^{z=0} (G/G_0)^{6.6}\, dt$, is shown for different densities Ω and different Brans-Dicke coupling parameters ω for $z_b = 5$. The values of τ_{ev} at $1/(1+\omega) = 0$ are the general relativistic look-back times to $z = 5$. These calculations are for $H_0 = 55$ km/s/Mpc, but τ_{ev} scales as H_0^{-1}.

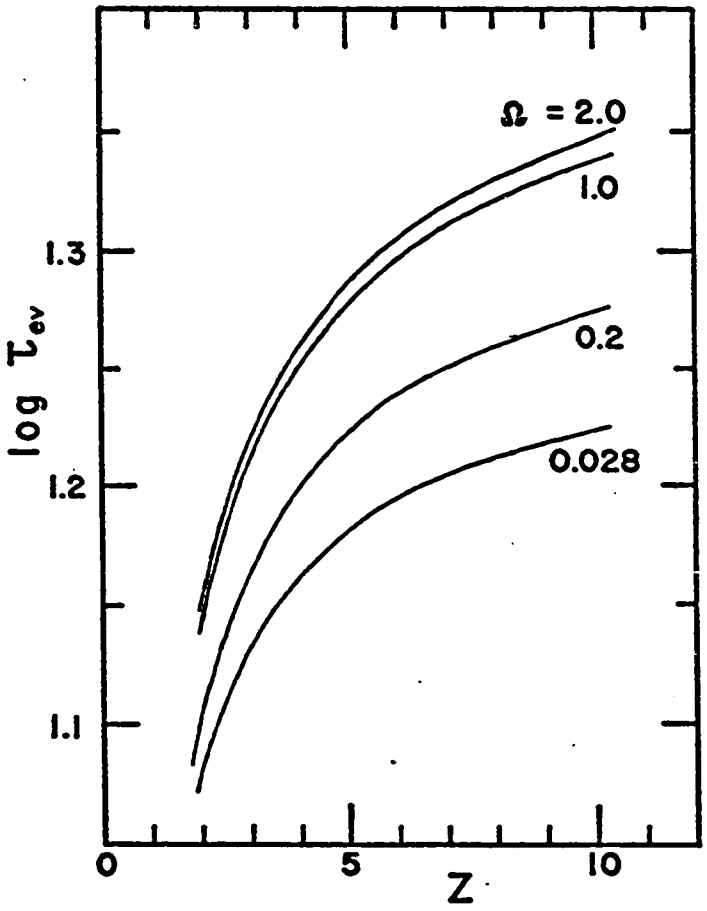

Fig.13.---Log τ_{ev}(Gyr) vs. redshift z. The variation of evolution time (see Fig. 12) from a given z to the present time is shown for different density Ω universes. The assumed Brans-Dicke cosmology has $\omega = 6$ and $H_0 = 55$ km/s/Mpc. The time τ_{ev} scales as H_0^{-1}.

CHAPTER V. GALAXY SYNTHESIS AND EVOLUTION

§1. Parameters of the Galactic Models

In this chapter the evolution of galactic magnitudes and colors is examined. Systematic evolution of galactic magnitudes is important in determining the cosmological world model, notably the deceleration parameter q_0, because galaxies are used as standard candles for the cosmic distance scale. The evolution of galactic colors is directly observable as a function of redshift, independent of absolute magnitude, and can be used to test the galactic models. I shall consider only single generation models, galaxies in which all star formation occurred simultaneously at some early epoch in the history of the universe. This approximation seems valid for giant elliptical galaxies (Larson 1974) and has been applied to such models by other authors (Tinsley 1972a, Rose and Tinsley 1974).

The galactic models are synthesized from the STD and BDI stellar tracks which are described in Chapter III. Thus these models are restricted to one composition, (Y,Z) = (0.25,0.02), and will have neither spatial gradients nor variations in metallicity. The contribution of globular clusters as a separate population to the integrated light of the galactic models is ignored. These single-generation, single-population galactic models are constructed like isochrones which are described in Appendix B. The theoretical quantities (log L, log T_{eff}) are converted into the observable

broad-band UBVRIJK-magnitudes (Johnson 1966) through the color-color and T_{eff}-color calibrations described in Appendix C. The T_{eff}-color relationship was calibrated so that the ZAMS would reproduce the (M_V, B-V) main sequence in the solar neighborhood and that the 1.2 $M_\odot$ giant branch would coincide with the (M_V, B-V) and (M_I, R-I) giant branches for the old disk population. In deriving the integrated magnitudes and colors of the galactic models, I shall ignore any effects of absorption or reddening within the galaxy. Also, I shall not consider the U-colors since the presence of relatively few, young, massive stars will greatly influence the integrated U-magnitude.

In spite of all the simplifying assumptions which have just been made, there still remain three free parameters in describing these galactic models. First, the age τ of the galaxy must be specified. In cases where a specific cosmological model is chosen, a knowledge of the redshift z is sufficient if a redshift at stellar formation is specified.

Second, a mass distribution of the stars in the galaxy, the initial mass function (IMF), must be defined. I have chosen a one-parameter exponential IMF of the form $N(m) = m^{-s}$ where $N(m) \cdot dm$ is the number of stars in the mass interval (m, m+dm). My parameter s will cover the range (0,4) and is similar to Tinsley's (1972a) x = s-1. This range includes the classic Salpeter (1955) mass spectrum s = 2.35 as well as recent values for open clusters (s = 2.74, Taff 1974) and for the young disk population (s $\approx$ 0, Eggen 1974). Even if

the mass spectrum in the solar neighborhood were well defined, it would not necessarily apply to the initial burst of star formation in a giant elliptical. I shall not be concerned with the upper or lower mass limits which normalize the IMF since I am not interested in mass-to-light ratios which may be greatly influenced by non-luminous matter.

Ideally, the third and last parameter of the galactic models should be determined from the theoretical models: L_{max}, the maximum luminosity attained during the hydrogen- and helium-shell burning on the asymptotic giant branch before the envelope mass is lost. My own stellar evolution code is unable to follow the evolution to this stage, and the present research in this field (Wood 1974, Kutter and Sparks 1974, Smith and Rose 1972) is limited to individual models with no conclusive general results. Thus, I shall allow L_{max} to vary over the range $\log L_{max}/L_{\theta} = 3.60\text{-}4.40$ as a free parameter in the galactic models. The (luminosity, core mass)-relation derived from Sweigart's (1975) data is employed, and the values are listed in table 1.

The isochrone program includes all stars from the tip of the asymptotic giant branch down to a lower-main-sequence mass of 0.5 M_{θ}. The stellar masses below 0.5 M_{θ} are excluded because they are outside the range of my evolutionary tracks. For a turn-off mass of approximately 1 M_{θ}, the fraction which these low-mass stars contribute to the main-sequence bolometric luminosity can be estimated from $L \sim M^{4.7}$ (see Chapter III)

$$L(M < 0.5\ M_{\theta})/L(\text{main sequence}) \approx 2^{s-5.7} . \qquad (1)$$

Thus, the omission of the low-mass stars will affect the main-sequence fraction of the total luminosity by at most 30% in the worst case of s = 4.

§2. The Standard Galaxy

In this section I shall consider only standard ($G \equiv G_0$) galaxy models and their evolution as a function of age, independent of the cosmological model. The models are constructed from the STD evolutionary tracks (see Chapter III) and cover the age range τ = 6-16 Gyr. The corresponding asymptotic giant branch masses range from 1.23 M_θ to 0.94 M_θ.

First, I shall examine the questions of where most of the stars are with regard to evolutionary status and from what stars does most of the light come. In figure 1 the relative number of stars N and the bolometric and BVRIJK luminosity contributions of the stars are plotted as a function of the bolometric luminosity for a standard model galaxy at an age of 14 Gyr. The solid lines represent the extremely steep IMF of s = 4; and the dotted lines, the flat IMF of s = 0. The numbers in brackets represent the relative contribution of both the main sequence and the part of the asymptotic giant branch which is more luminous than the giant branch maximum. These numbers in figure 1 are for the cases s=0/s=4 and refer to the case $\log L_{max}/L_\theta = 4.40$. The effects of a reduced L_{max} can be estimated by truncating the graph.

With regard to numbers of stars, it is obvious that the main sequence dominates for all ranges of IMF's and that the

horizontal branch stars (also called clump giants, Faulkner and Cannon 1973) represent a major giant constituent. With regard to the bolometric luminosity, the importance of the main sequence is reduced (16-28%), and the upper giant branch and very luminous asymptotic giant branch stars become extremely important (35-41%). As one proceeds to longer wavelengths (V →K), the red, luminous stars of the giant branch and the asymptotic giant branch become increasingly more important.

The effects of varying L_{max} upon the magnitudes and colors of the galactic models are almost independent of the IMF and the age, and they are given in table 2. The increase in L_{max} by 1.0 bolometric magnitude yields a negligible increase in the B, V and R magnitudes ($\lesssim 0^m.03$), but has a substantial effect on the redder colors. The behavior of the models with regard to the IMF parameter s is much more complicated and exhibits a strong age interdependence. The obvious--but trivial--effect of s upon the static models is to increase the importance of the main sequence.

Knowledge of the time evolution of the absolute visual magnitude M_V of giant elliptical galaxies is necessary in order to determine the cosmological deceleration parameter q_0. The value of q_0 is determined to first order in redshift z by (Weinberg 1972, pp. 441-451)

$$m_V = M_V - 5 \cdot \log H_0 + 5 \cdot \log z + 1.086 \cdot z \cdot \{1 - (q_0 + 0.92 \cdot H_0^{-1} \cdot dM_V/dt)\} + \text{constants} + \text{corrections}. \qquad (2)$$

The effect of galactic magnitude evolution is to produce a difference δq_0 between the true deceleration parameter q_0^{true} and the deceleration parameter q_0^{obs} which is observed by examining the deviation from linearity of the (m_V, log z)-relation. This value of δq_0 is related to the magnitude evolution by

$$\delta q_0 = q_0^{obs} - q_0^{true} = -0.92 \cdot \{M_V(z) - M_V(0)\}/z$$
$$\approx 0.92 \cdot H_0^{-1} \cdot dM_V/dt = 9.0 \cdot h^{-1} \cdot dM_V/dt(Gyr) \ , \qquad (3)$$

where $h \equiv H_0/100$ km/s/Mpc.

For the standard model galaxies the magnitude evolution was found to be (i) almost independent of L_{max}, (ii) partially dependent upon the age in no simply definable manner, (iii) strongly dependent upon the IMF, and (iv) always decreasing in luminosity with age for all IMF's ($0 \leq s \leq 4$).

$$dM_V/dt(Gyr) = \begin{cases} 0.130 - 0.020 \cdot s & (12<\tau<16 \text{ Gyr}) \\ 0.195 - 0.035 \cdot s & (6<\tau<8 \text{ Gyr}) \end{cases} \qquad (4)$$

Thus, assuming a value of $H_0 = 55$ km/s/Mpc, the value of q_0^{obs} is greater than the true value by as little as 0.8 (s=4, $\tau \approx 14$ Gyr) and as much as 3.2 (s=0, $\tau \approx 7$ Gyr).

The integrated galactic colors as functions of the model parameters are shown in tables 3 (B-V), 4 (V-R), 5 (V-I), 6 (V-J) and 7 (V-K). For all of these colors the evolution is minimal except in the age range 6-8 Gyr. The integrated (B-V) is almost independent of L_{max} and evolves at a rate which depends only on the value of (B-V).

$$d(B-V)/d\log\tau = \begin{cases} 0.24 + 1.6 \cdot \{1.00-(B-V)\} & (0.90<B-V<1.00) \\ 0.24 - 4.0 \cdot \{(B-V)-1.00\} & (1.00<B-V<1.04) \end{cases} \qquad (5)$$

The later colors also evolve towards the red and tend to level off for ages greater than 10 Gyr. For these old galaxies the value of (V-R) is roughly constant with age and IMF, varying solely with L_{max}. As one progresses to (V-K), the asymptotic values of the colors become more dependent upon L_{max} (see table 2) and increasingly more sensitive to the IMF ($d(V-K)/ds \approx -0\overset{m}{.}03$).

Assuming that the color calibrations (Appendix C) are accurate, I can compare the observed colors for giant ellipticals which are listed in table 8 with those from my models in tables 3-7. From Sandage's (1973) (B-V) color nothing can be ascertained about L_{max}, but IMF-age limitations can be derived: for $\tau = 8$, $s \lesssim 2$; for $\tau = 14$, $s \gtrsim 2$. The observed (V-R) places an upper limit on $\log L_{max}/L_{\odot} \lesssim 4.40$. Grasdalen's (1975) (V-K) color puts a lower limit on $\log L_{max}/L_{\odot} \gtrsim 4.00$. Frogel et al.'s (1975) value for (V-K) is out of the range of acceptable L_{max} because of core mass limitations ($\log L_{max}/L_{\odot} > 4.40$ implies $M_{core} > 0.93\ M_{\odot} \approx M_{max}$). Combining Frogel et al.'s value of (J-K) with Grasdalen's (V-K) gives a (V-J) which places only minor limitations on the model parameters: if $\log L_{max}/L_{\odot} = 4.40$, then $s \gtrsim 2$. The only reported evolution of galactic colors is for (B-V). For (B-V) = 0.98±0.03 the models' (B-V) evolution ($d(B-V)/d\log\tau = 0.26\pm0.06$) falls within the rather broad observational limits of Sandage (1973) and Crane (1975).

The observed colors do not adequately limit the model parameters. If one further assumes an open universe with

H_0 = 55 km/s/Mpc, then one can set bounds on the present age of the universe, $12 < t_0 < 18$ Gyr. Thus for giant ellipticals formed early in the universe, some limits on the model parameters can be set: $10 < \tau < 16$ Gyr, $4.00 \lesssim \log L_{max}/L_0 \lesssim 4.40$, and $s \gtrsim 2$. The magnitude evolution of the galaxies is then non-negligible,

$$dM_V/dt = 0^m.03\text{-}0^m.09\ \text{Gyr}^{-1}, \quad (5>s\gtrsim 2) \tag{6}$$

and the corresponding effect on δq_0 is quite large but still not well defined,

$$\delta q_0 = 1 \pm \tfrac{1}{2} \tag{7}$$

These values are similar to those obtained by Tinsley (1972a) and re-enforce the importance of galactic evolution in the determination of the cosmological model.

§3. Brans-Dicke Galaxy Evolution

In this section the evolution of standard ($G \equiv G_0$) and Brans-Dicke (Brans and Dicke 1961) model galaxies will be examined for a specific cosmological model: H_0 = 55 km/s/Mpc, $\Omega = 0.20$, $z_{birth} = 5$, and the Brans-Dicke $\omega = 6$. With these two cosmologies (STD and BDI, see Chapter II), the evolution of magnitudes and colors is compared as a function of an observable quantity, the redshift z. Isochrones in the (log L, log T_{eff})-diagram of the STD and BDI galaxies are shown in figures 2 and 3 both for the present epoch (z=0) and for a redshift z = 0.8. The only obvious difference between the two models is the comparably older appearance of the BDI models at both redshifts. This difference is due to the higher G

values in the early history of the BDI model which cause a substantially faster aging of the stars.

The backward evolution with redshift of the integrated colors and magnitudes of the STD and BDI models is shown in figure 4 for an IMF of s = 2 and log L_{max}/L_{θ} = 4.20. The effect of L_{max} upon the magnitudes and colors of the BDI model is the same as for the STD model and has been given in table 2. Upon examining figure 4, one notes that the evolution of the BDI model runs parallel to that of the STD model with the exception of M_{max}, the mass of the most highly evolved stars on the asymptotic giant branch.

The bolometric magnitude of the BDI model does not decrease (i.e., increase in luminosity) quite as rapidly as the STD model. This is the opposite of what might be naively expected since G is increasing with z and $L \sim G^7$ for individual main sequence stars. The effects of this increase in G upon M_{bol} for a non-evolving BDI galaxy are shown with the M_{bol} evolution in figure 4. The BDI model does not demonstrate this additional increase in luminosity because the evolution of the turn-off mass as indicated by M_{max} is proceeding at a slower rate as compared with the STD models. The net result is that the BDI model looks slightly older and redder but evolves at approximately the same rate as the STD model when examined in the BVRIJK colors.

The dependence of the evolution of the colors and the V-magnitude upon the model parameters, including the effects of BDI, has been determined by a crude factor analysis and is

listed in table 9. The color evolution for all models is always towards the blue but is small compared with the magnitude evolution. The BDI model evolves more rapidly towards the blue, especially in the later colors (e.g., V-K). It does not brighten as quickly as the STD model unless the IMF parameter $s > 3$.

The V-magnitude evolution is important in determining the difference between the observed deceleration parameter and the true one. If dM_V/dz depends on redshift, then the value of δq_0 will also depend on the redshift at which q_0^{obs} is evaluated. Sample values of δq_0 are given in table 10 for the STD model, the BDI model, and a non-evolving BDI model with $L_V \sim G^7$. As expected from the V-magnitude evolution, the difference in δq_0 between the BDI and STD models is in the opposite sense to the difference expected from $L \sim G^7$. This difference disappears entirely for an $s \simeq 3$ IMF.

Thus, the effect of a higher G in the past, as predicted by Brans-Dicke theory, actually reduces the luminosity evolution with increased redshift (i.e., higher G). The evolution towards the blue of the integrated galactic colors proceeds slightly faster in the BDI model but is intrinsically small for all models. There is very little net difference between the STD and BDI models except for the greater apparent age of the BDI model which is due to the lower value of the main sequence turn-off mass.

§4. Discussion

In this study of galaxy synthesis and evolution, my galactic models are limited to a single generation of solar-abundance stars from a complete set of self-consistent evolutionary tracks. The transformation of the theoretical effective temperatures into observable broad-band colors is not based upon the T_{eff}-color calibrations in the literature but is designed to reproduce observed sequences of the disk population with my own T_{eff}'s. While changes in metallicity will certainly influence the actual values of the integrated galactic colors, they will be unlikely to change the evolution pattern of the colors and magnitudes. The inclusion of a large number of metal-poor stars, especially on the horizontal branch, would greatly increase the blue light from the models. This proposition seems unlikely in view of the rapid metal enrichment in the early phases of stellar formation which is found by Larson (1974). The adopted power-law IMF applies only to the stars with mass greater than 0.5 $M_\odot$. If the ignored, low-mass stars exhibit a very steep IMF, then the redder colors of the galaxy models will be affected. With these limitations in mind, let me examine these models with regard to the evolution of colors and magnitudes, the determination of the model parameters through observation, the effect of a Brans-Dicke variable-G universe, and the similar single-generation galactic models of Tinsley (1972a, 1972b) and Rose and Tinsley (1974).

The evolution of the integrated galactic V-magnitude is quite substantial for all of my models. As can be seen in figure 1, the V-light is independent of both the maximum luminosity of the asymptotic giant branch and the lower main sequence; and thus the V-magnitude evolution will depend solely on the IMF about the turn-off (0.8-1.2 $M_\odot$). The V-luminosity always decreases with age for an IMF parameter $0 < s < 4$, but by extrapolating my results, this trend could be reversed for an extremely steep IMF of $s > 6$. Unlike Tinsley (1972a) I do not find that $(t \cdot dM_V/dt)$ is independent of the age of the models (see equation 4). We both concur that dM_V/dt is linear with respect to the power-law IMF parameter s. Our results agree exactly if I take the mean of my values at an age of 10 Gyr,

$$(t \cdot dM_V/dt)_{10\ Gyr} = 1.6 - 0.28 \cdot s \qquad (8)$$
$$\simeq 1.3 - 0.3 \cdot x \quad \text{(Rose and Tinsley 1974)}$$

where x(Tinsley) = s - 1.

The evolution of M_V causes an error in the observational determination of the deceleration parameter q_0. The value of this error δq_0 (equation 3) depends on both dM_V/dt and the cosmological model. For the particular model in this study ($H_0 = 55$, $\Omega = 0.20$), the observed deceleration parameter should be reduced by $\delta q_0 = 1 \pm \frac{1}{2}$ for a reasonable range of IMF's.

The evolution of the integrated galactic colors is quite small when compared with the magnitude evolution (see table 9). With the exception of (V-R), all of the colors evolve slowly

to the red and approach a constant value as the galaxy ages from 6 to 16 Gyr. The later colors, especially (V-K), tend to evolve more rapidly in the younger galaxies. While Rose and Tinsley (1974) claim that (V-R) always evolves to the red, I find that (V-R) (i) has the slowest evolution of all the colors, (ii) is almost constant for ages greater than 12 Gyr, and (iii) sometimes exhibits a small turnover towards the blue for ages greater than 14 Gyr. This latter phenomenom does not occur in the specific cosmological model which was examined because the galactic ages in this model are less than 13.5 Gyr.

The observations of nearby galaxies should be able to restrict the range of the model parameters. Knowledge of the IMF parameter s is crucial in determining the magnitude evolution. Rose and Tinsley (1974) claim that s = 2 produces galactic colors which are too blue for ages less than 11 Gyr and that s = 4 models are too red at longer wavelengths. I find that for s = 2 my models are within the observed range of (B-V) for ages as young as 8 Gyr. My models for s = 4 are not too red, but I have ignored stars below 0.5 $M_\odot$. However, from figure 1, these low-mass stars could not contribute substantially to the integrated light for any colors earlier than K or possibly J (1.25μ). Even then, the IMF would have to extend very steeply ($s \gtrsim 4$) to stars well below 0.5 $M_\odot$. Based upon age limitations (open universe with $H_0 \simeq 50$ km/s/Mpc) and the observations given in table 8, I can only place weak bounds on the value of s, $2 \lesssim s < 5$. The most recently

observed value of s = 2.74 (Taff 1974) for open clusters produces acceptable galaxy models.

The other important model parameter is the maximum luminosity--or core mass--which is reached by the asymptotic giant branch stars in the final stage of evolution which is considered in this study. The value of L_{max} does not affect (B-V) but has a successively larger effect on the later colors (table 2). The limitations on L_{max} based upon my models and the observations, $4.00 \lesssim \log L_{max}/L_{\theta} \lesssim 4.40$, correspond to a core mass range of 0.65-0.93 M_{θ}. This large range in L_{max} is due to the large range of observed values in the late-type colors such as (V-K). The results of Rose and Tinsley (1974) indicate that core masses in excess of 0.7 M_{θ} produce galaxy models which are too red at a wavelength of 1.0μ. My models have acceptable J-colors (1.25μ) for core masses up to 0.9 M_{θ}, and I could find no I-color (0.9μ) observations to test the models.

Tighter restrictions on the parameters of the galactic models could certainly be made with more accurate observations of the mean colors of giant elliptical galaxies. This is especially true in the red colors which are sensitive to the value of L_{max}. The IMF from the turn-off to the lower main sequence could be more accurately fixed from observations of luminosity sensitive lines from the V through K colors. The contribution of the main sequence to the total luminosity in a given wavelength region can be used with figure 1 to estimate the IMF. While improvements in the model parameters

can be derived in this manner, there comes a point at which errors in the initial color calibrations become important. The color calibration of the most luminous, very red stars is difficult because of the relatively small number of such stars which are observed. Their theoretical effective temperatures are unreliable since the radius--if such a quantity can be defined--depends sensitively on the theory of convection. The assumption of a single generation of stars will adequately define the present appearance of the galaxy, if the stars were formed over a period of 1-2 Gyr in the early universe. However, the assumption of uniform solar abundances is certainly not exact, and variations in metallicity will cause a range of turn-off masses (e.g., the metal-poor stars about 1 $M_\odot$ evolve faster than their solar-abundance counterparts) in addition to changing the color calibrations from the main sequence to the asymptotic giant branch. Thus, an absolute determination of the model parameters from galaxy synthesis would require more realistic galactic models with correspondingly accurate color calibrations.

My approach to the problem of galaxy evolution in a Brans-Dicke universe is to assume that the present values of the expansion rate, the mean density, and the redshift at galaxy formation are known. Then the evolution of a standard Friedmann-cosmology galaxy is compared with that of a galaxy which is evolved in the corresponding Brans-Dicke cosmological model with $\omega = 6$. The Brans-Dicke galaxy undergoes a greater effective evolution because of the higher values of G in its

past history, and thus at the present epoch, it has a smaller turn-off mass and appears slightly redder than the standard galaxy (e.g., +0.035 in (B-V)). The color evolution of the Brans-Dicke galaxy roughly parallels that of its standard counterpart, but its V-magnitude evolution is slightly slower for an IMF of $0 < s < 3$.

These results are opposite to those of Tinsley's (1972b) analytical model in which an $L \sim G^7$ contribution is added onto the standard model's magnitude evolution. If one assumes that both models are at the same evolutionary stage at the present time, then this addition of $L \sim G^7$ (not true for giant branch and helium-burning stars) may be valid. But, this assumption requires the two models to have evolved in different universes (e.g., $H_0(BD) < H_0(standard)$).

However, both Tinsley and I agree that the difference in magnitude evolution between the Brans-Dicke and standard models is undetectable at the present time. If one believes in the approximate accuracy of the cosmological parameters ($H_0 \simeq 50$ km/s/Mpc, $\Omega \simeq 0.2$, $z_{birth} \simeq 5$), then one can probably rule out a much stronger G dependence (e.g., Brans-Dicke with $\omega < 3$) which would result in an excessively evolved galaxy. Choosing between the Brans-Dicke model with $\omega = 6$ and the standard model, based upon the redder appearance of the former, places too great a burden on the accuracy of the T_{eff}-color calibration and on the assumption of solar abundances.

TABLE 1. CARBON/OXYGEN CORE MASSES

$\log L/L_\theta$	M_{core}/M_θ
3.6	0.575*
3.8	0.598*
4.0	0.654
4.2	0.760
4.4	0.926

* Not on linear portion:

$$L/L_\theta = 55500 \cdot (M_c - 0.474)$$

TABLE 2. INTEGRATED GALACTIC EFFECTS OF INCREASING THE MAXIMUM LUMINOSITY

$\log L_{max}/L_{\theta} = 3.80 \rightarrow 4.20$

Quantity	ΔQuantity
M_{bol}	-0.25±0.03
M_V	-0.01
B-V	+0.005±0.001
V-R	+0.024±0.003
V-I	+0.09±0.01
V-J	+0.14±0.01
V-K	+0.20±0.01

TABLE 3. STANDARD GALAXY (B-V) COLORS

IMF	Age(Gyr)					
	6	8	10	12	14	16
s = 0	0.94	0.98	1.00	1.02	1.03	1.04
2	0.91	0.96	0.98	1.00	1.01	1.02
4	0.89	0.94	0.97	0.99	1.01	1.02

Add + $0.015 \cdot (\log L_{max}/L_{\theta} - 4.00)$

TABLE 4. STANDARD GALAXY (V-R) COLORS

$\log \frac{L_{max}}{L_\theta}$	IMF	Age(Gyr)					
		6	8	10	12	14	16
4.40	s = 0	0.86	0.88	0.89	0.90	0.90	0.90
	2	0.83	0.86	0.88	0.89	0.89	0.90
	4	0.81	0.84	0.86	0.88	0.89	0.89
4.00	s = 0	0.82	0.84	0.86	0.86	0.87	0.87
	2	0.80	0.82	0.84	0.85	0.86	0.87
	4	0.78	0.81	0.84	0.85	0.86	0.87
3.60	s = 0	0.80	0.82	0.84	0.85	0.86	0.86
	2	0.78	0.81	0.83	0.84	0.85	0.85
	4	0.77	0.80	0.82	0.84	0.85	0.86

TABLE 5. STANDARD GALAXY (V-I) COLORS

$\log \frac{L_{max}}{L_\odot}$	IMF	Age (Gyr)					
		6	8	10	12	14	16
4.40	s = 0	1.64	1.67	1.70	1.71	1.71	1.71
	2	1.58	1.62	1.66	1.67	1.68	1.68
	4	1.53	1.58	1.62	1.65	1.66	1.66
4.00	s = 0	1.48	1.53	1.55	1.57	1.57	1.58
	2	1.44	1.49	1.52	1.54	1.55	1.56
	4	1.41	1.47	1.51	1.53	1.55	1.56
3.60	s = 0	1.42	1.47	1.49	1.51	1.52	1.53
	2	1.38	1.44	1.47	1.49	1.51	1.51
	4	1.37	1.42	1.46	1.49	1.51	1.52

TABLE 6. STANDARD GALAXY (V-J) COLORS

$\log \frac{L_{max}}{L_0}$	IMF	Age (Gyr)					
		6	8	10	12	14	16
4.40	s = 0	2.20	2.24	2.27	2.29	2.29	2.28
	2	2.12	2.18	2.22	2.24	2.25	2.24
	4	2.05	2.12	2.17	2.20	2.21	2.21
4.00	s = 0	1.98	2.03	2.06	2.08	2.09	2.09
	2	1.92	1.98	2.02	2.05	2.06	2.06
	4	1.88	1.95	2.00	2.03	2.05	2.06
3.60	s = 0	1.89	1.95	1.98	2.00	2.01	2.02
	2	1.84	1.90	1.95	1.97	1.99	2.00
	4	1.81	1.88	1.93	1.96	1.99	2.00

TABLE 7. STANDARD GALAXY (V-K) COLORS

$\log \frac{L_{max}}{L_\theta}$	IMF	Age (Gyr)					
		6	8	10	12	14	16
4.40	s = 0	3.11	3.16	3.20	3.21	3.21	3.20
	2	3.01	3.08	3.12	3.15	3.15	3.14
	4	2.90	2.99	3.05	3.08	3.10	3.10
4.00	s = 0	2.80	2.86	2.90	2.92	2.93	2.93
	2	2.72	2.79	2.84	2.87	2.89	2.89
	4	2.65	2.74	2.80	2.84	2.86	2.87
3.60	s = 0	2.67	2.73	2.78	2.80	2.82	2.82
	2	2.60	2.68	2.73	2.76	2.78	2.79
	4	2.55	2.64	2.70	2.74	2.77	2.78

TABLE 8. OBSERVED COLORS FOR GIANT ELLIPTICAL GALAXIES

$\langle B-V \rangle$	= 0.98±0.03	Sandage 1973
$\langle V-R \rangle$	= 0.86±0.03	Sandage 1973
$\langle V-K \rangle$	= 2.9-3.2	Grasdalen 1975
	= 3.2-3.4	Frogel et al. 1975
$\langle J-K \rangle$	= 0.97	Frogel et al. 1975
$\frac{\partial (B-V)}{\partial \log t}$	< 0.3	Sandage 1973
	= 0.17±0.15	Crane 1975

TABLE 9. MEAN COLOR EVOLUTION <∂COLOR/∂z>

STD MODEL OVER RANGE z = 0.0 → z = 0.1

WITH s = 0 AND log L_{max}/L_{θ} = 4.20

Color	Basic Rate	Additional Terms IMF	z=0→ z=0.5	log L_{max} =3.8	BDI
(B-V)	-0.09	-0.01•s	-0.02	0.00	-0.01
(V-R)	-0.05	-0.01•s	-0.01	-0.01	-0.01
(V-I)	-0.05	-0.02•s	-0.04	-0.02	-0.03
(V-J)	-0.06	-0.02•s	-0.05	-0.03	-0.04
(V-K)	-0.05	-0.03•s	-0.06	-0.04	-0.05
V	-2.16	+0.34•s	*0.83†	0.00	+0.23 -0.07•s

†Multiplicative factor

TABLE 10. δq_0 BASED UPON EVOLUTION OF M_V

Model	Initial Mass Function			
	s = 0	1	2	3
STD	1.69±0.30*	1.40±0.27	1.12±0.23	0.85±0.20
BDI	1.52±0.25	1.30±0.23	1.08±0.20	0.86±0.17
BDI with $L \sim G^7$ (No Evolution)	0.214±0.012			

* Values are $0.92 \cdot \Delta M_V/z$ for a range $z = 0.0 \rightarrow z = 0.4$
+ refers to range $z = 0.0 \rightarrow z = 0.1$
- refers to range $z = 0.0 \rightarrow z = 1.0$

V. References

Brans, C. and R.H. Dicke 1961, Phys.Rev., 124, 925.

Crane, P. 1975, Ap.J.(Letters), 198, L9.

Eggen, O.J. 1974, P.A.S.P., 86, 697.

Faulkner, D.J. and R.D. Cannon 1973, Ap.J., 180, 435.

Frogel, J.A., S.E. Persson, M. Aaronson, E.E. Becklin, K. Matthews and G. Neugebauer 1975, Ap.J.(Letters), 195, L15.

Grasdalen, G.L. 1975, Ap.J., 195, 605.

Johnson, H.L. 1966, Ann.Rev.Ast.& Ap., 4, 193.

Kutter, G.S. and W.M. Sparks 1974, Ap.J., 192, 447.

Larson, R.B. 1974, M.N.R.A.S., 166, 585.

Rose, W.K. and B.M. Tinsley 1974, Ap.J., 190, 243.

Salpeter, E.E. 1955, Ap.J., 121, 161.

Sandage, A. 1973, Ap.J., 183, 711.

Smith, R.L. and W.K. Rose 1972, Ap.J., 176, 395.

Sweigart, A. 1975, private communication.

Taff, L.G. 1974, A.J., 79, 1280.

Tinsley, B.M. 1972a, Ap.J.(Letters), 173, L93.

---------- 1972b, Ap.J.(Letters), 174, L119.

Weinberg, S. 1972, Gravitation and Relativity, (New York: Wiley & Sons), Chapters 15 & 16.

Wood, P.R. 1974, Ap.J., 190, 609.

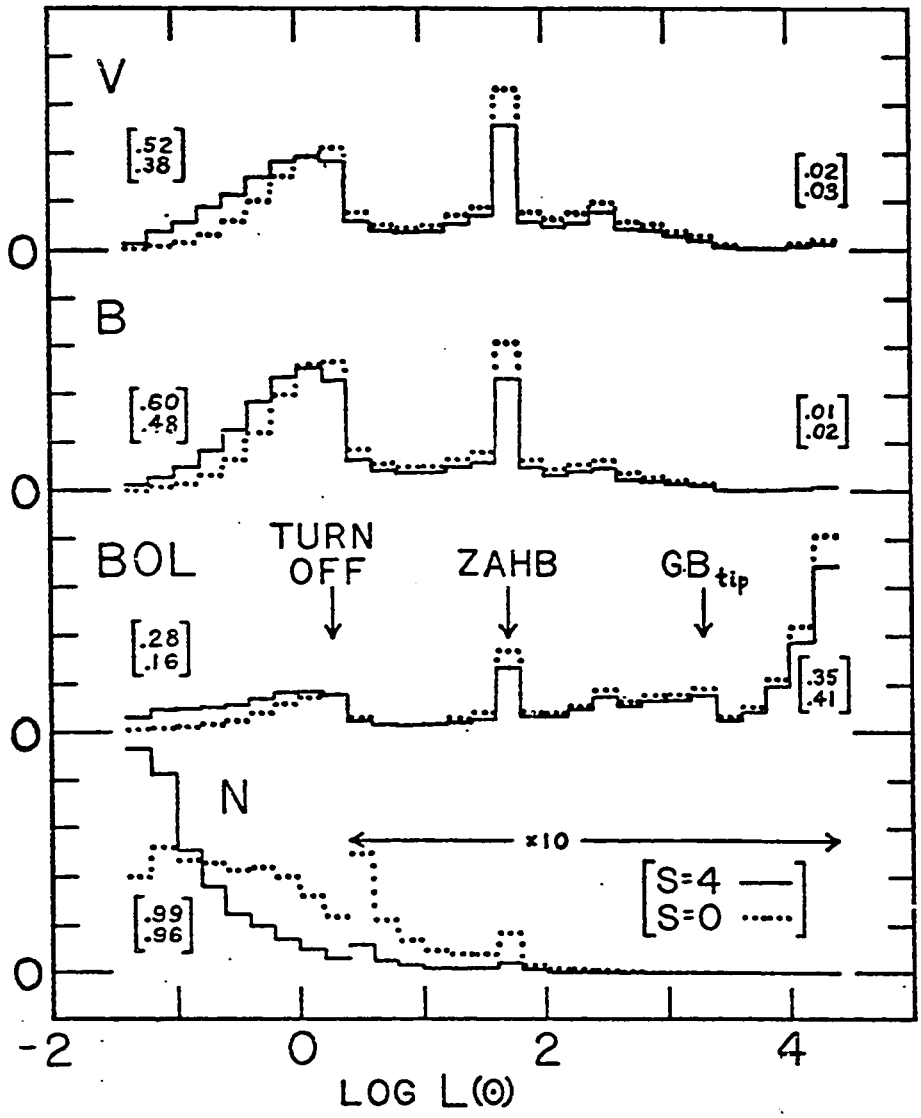

Fig.1a.---Distribution of light and numbers of stars as a function of luminosity for a standard model galaxy of age 14 Gyr and with $\log(L_{max}/L_0) = 4.4$. The vertical scale is arbitrary and represents the relative contribution for each interval of 0.2 in log L. N is the number of stars, BOL is the bolometric luminosity, and BVRIJK are the broad-band luminosities. The solid line is for an exponential IMF of s = 4; the dotted line, s = 0. The luminosities of the main-sequence turn-off, { → Fig.1b}

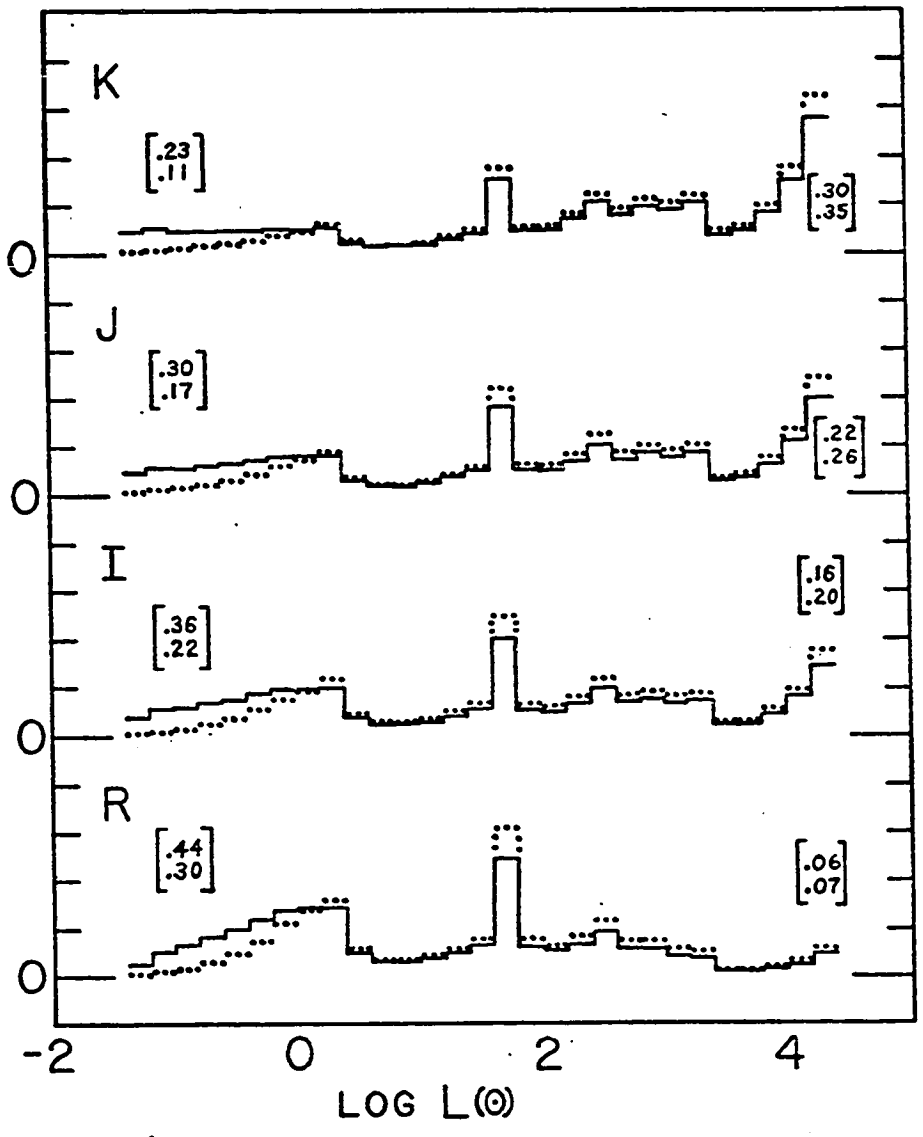

Fig.1b.---{continued} the zero-age horizontal branch (ZAHB), and the tip of the giant branch are denoted. The numbers in parentheses refer to the (s=4/s=0) fraction of the particular quantity which is due to the main sequence (left side) or to the upper asymptotic giant branch (right side).

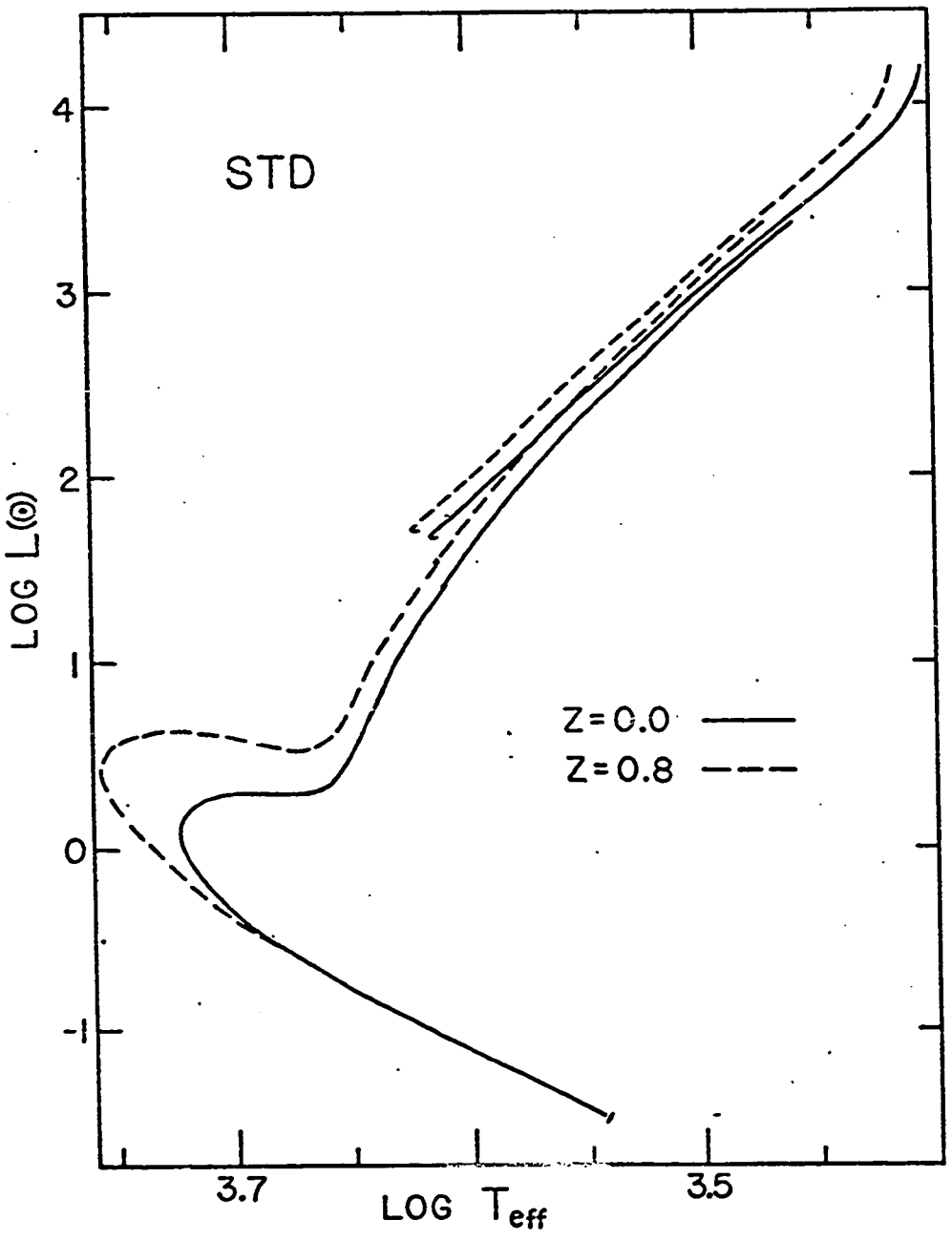

Fig.2.---Isochrone for STD model galaxy. The position in the (log L, log T_{eff})-diagram of the stars which were formed at a redshift of z_{birth} = 5 in a universe with H_0 = 55 km/s/Mpc and Ω = 0.20. The solid line is for the present epoch (z=0); the dashed line, for z = 0.8.

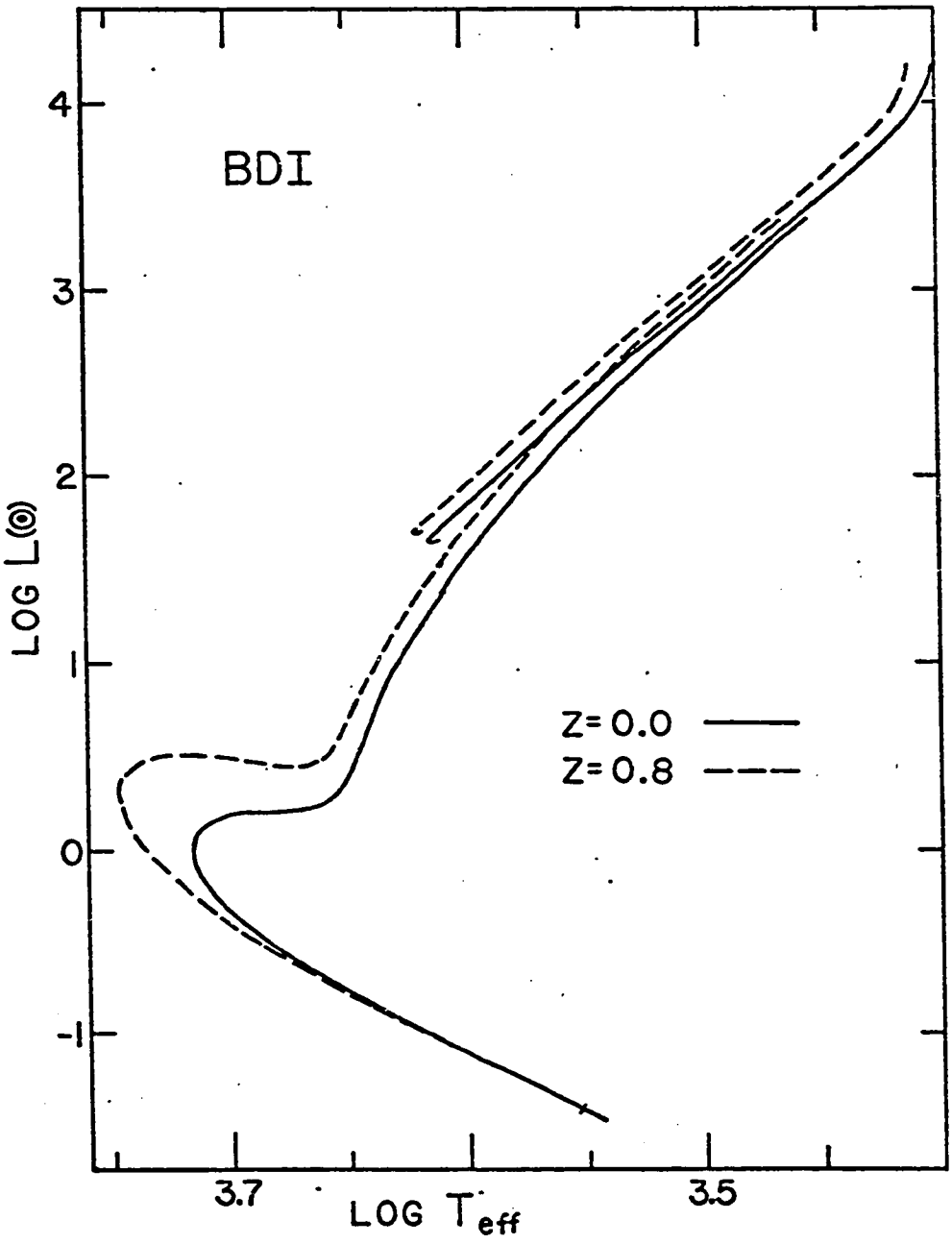

Fig.3.---Isochrone for BDI model galaxy. This figure is the same as Fig. 2 except that the universe is Brans-Dicke with $\omega = 6$.

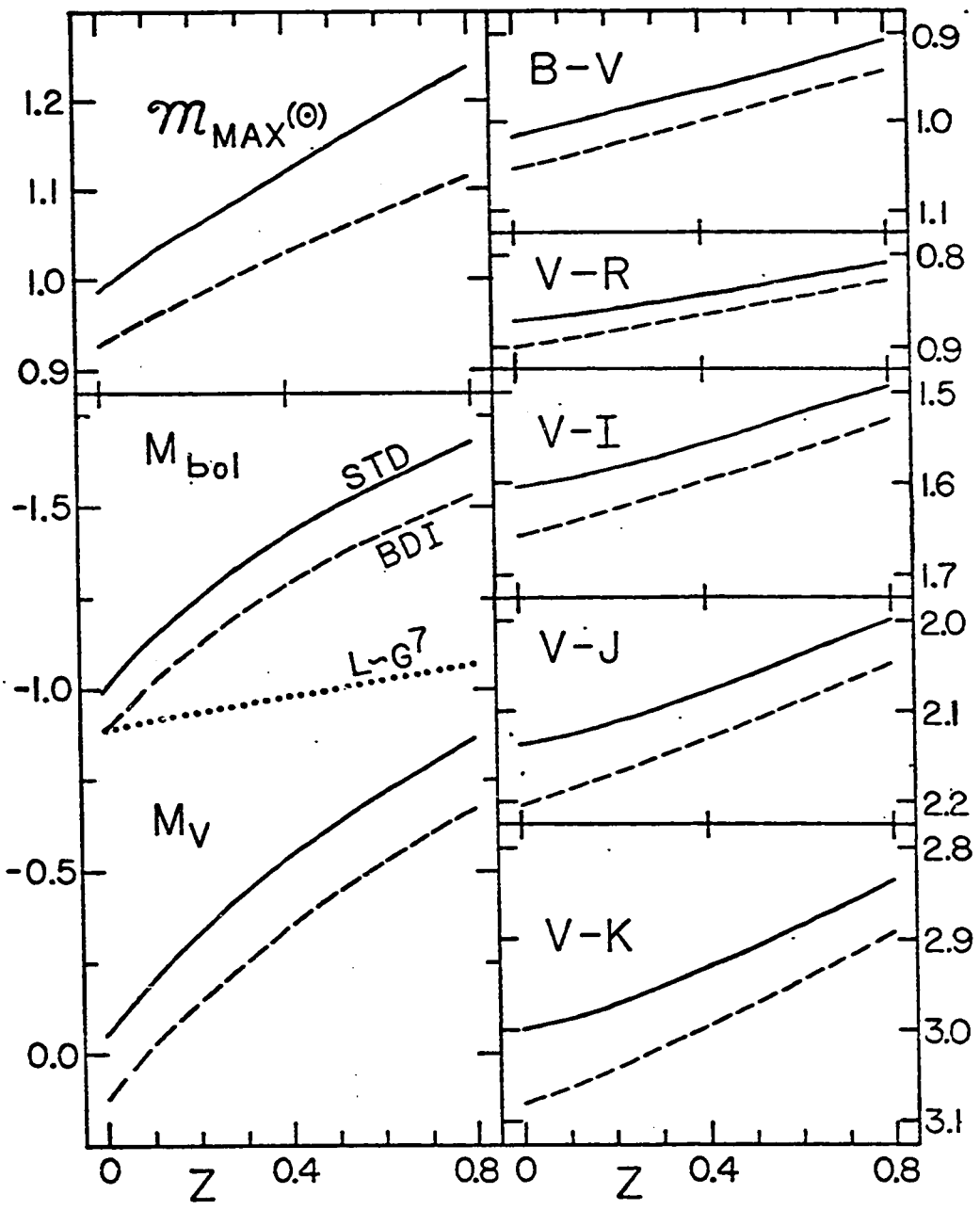

Fig.4.---Galactic evolution with redshift. The evolution of maximum mass, M_{bol}, M_V, and BVRIJK colors is shown as a function of redshift for STD (solid lines) and BDI (dashed lines) galaxies with s = 2 and $\log(L_{max}/L_\theta) = 4.2$. The maximum mass refers to the most highly evolved stars on on the asymptotic giant branch. The absolute scale of the M_{bol} and M_V magnitudes is arbitrary but the relative differences are correct. The magnitude evolution in the BDI universe with only $L \sim G^7$ (dotted line) is also shown.

CHAPTER VI. IS BRANS-DICKE OBSERVABLE?

In this thesis I have examined in detail the effects of a Brans-Dicke universe upon the evolution of both individual stars and the integrated galactic properties of a conglomerate of stars. The cosmological models assume that the universe is matter-dominated with a zero cosmological constant and, for the Brans-Dicke models, that $\dot{\phi}R^3 \to 0$ as $R \to 0$. In Brans-Dicke the local gravitational coupling coefficient G is a function of the redshift and, as such, is independent of the Hubble constant H_0. The function G(z) increases more steeply with redshift as either the fractional closure density Ω increases or the Brans-Dicke coupling parameter ω decreases. For very low density universes ($\Omega \leq 0.02$) with $\omega = 6$, the increase in G up to a redshift $z = 10$ is negligible. If the universe is not very dense ($\Omega \leq 1$), the age-redshift relation for the Brans-Dicke models is almost identical to that for the corresponding Friedmann models of general relativity theory.

In order to compute the stellar evolution tracks, a specific Brans-Dicke cosmological model (BDI) was selected: $H_0 = 55$km/s/Mpc, $\Omega = 0.2$, $z_{birth} = 5$, $\omega = 6$. The resulting variable-G stellar models were compared with models evolved under a constant G, and the BDI galaxy models were compared with galaxy models evolved with the corresponding Friedmann cosmology (STD). Although the maximum value of G in the BDI models may seem small ($\log G(z = 5)/G_0 = +0.047$), it

does yield an increase in the stellar luminosities of up to one full magnitude.

From the BDI stellar models in the mass range $0.5 - 1.1 M_{\odot}$ with composition (Y,Z) = (0.25, 0.02), the following dependences upon G for the main sequence stars were determined.

$$L(\text{main sequence star}) \sim G^{6.3-7.0} \cdot M^{4.7}$$

$$T_{eff}(\text{main sequence star}) \sim G^{1.0-1.5}$$

These relations can also be derived from homology arguments. If one examines the main sequence as a whole instead of following an individual star, then the main sequence which is observed at a given luminosity has little G dependence in either the effective temperature or the surface gravity.

$$T_{eff}(MS) \sim G^{+0.2}$$

$$g(MS) \sim G^{+0.4}$$

Since the amount of hydrogen consumed on the main sequence appears to be independent of G, the main sequence lifetime of an individual star is reduced by

$$\tau(\text{main sequence star}) \sim G^{-6.6}.$$

However, for $G > G_0$ the star is imitating a higher mass, more luminous star which has a shorter lifetime. If the amount of core burned out on the main sequence is proportional to the stellar mass, then the main sequence lifetime at a given luminosity is reduced by

$$\tau(MS) \sim G^{-2\pm1}.$$

The individual stars on the giant branch are also greatly affected by G if they are compared at equivalent

core masses.

$$L(\text{giant branch star}) \sim G^{7-10}$$

However, the value of the core mass at helium ignition is reduced by an increase in G, and hence, the maximum luminosity of the giant branch is almost independent of G.

$$L_{max}(GB) \sim G^{-1\pm1}$$

The shift in effective temperature of the giant branch as a whole is also minor.

$$T_{eff}(GB) \sim G^{<0.2}$$

The reduced core mass with increased G does cause a reduction in the giant branch lifetimes.

$$\tau(GB) \sim G^{-2\pm1}$$

Likewise, the individual stars with helium-core burning on the zero-age horizontal branch are greatly affected by G.

$$L_{He}(\text{ZAHB stars}) \sim G^{6.5} \cdot M_{core}^{4.6}$$

$$L_{H}(\text{ZAHB stars}) \sim G^{3.0} \cdot M_{core}^{2.0} \cdot M_{star}^{0.5}$$

But, the reduced core mass from the giant branch almost cancels out the horizontal branch's dependence upon G. The effective temperature of the horizontal branch with respect to the giant branch is independent of G to the accuracy of the models. In spite of the reduced core mass, the high-G star still has a reduced horizontal-branch lifetime when compared to the higher core-mass star which evolved from the giant branch with a constant $G = G_0$.

$$\tau(HB) \sim G^{-2\pm1}$$

I am unable to derive the G-dependences of the post-horizontal-branch phases since my evolution code cannot follow stars beyond helium-core exhaustion.

Consider now what effects one could possibly detect by observing an old cluster of solar-abundance stars which are subject to a uniform but higher value of G. The main sequence shifts upwards in luminosity and towards the blue, but this merely looks like a younger cluster with more massive stars at the main sequence turn-off. Unless one has an accurate calibration of the turn-off mass and the composition, no discrepancy can be detected. The luminosity range of the giant branch is only slightly reduced, and the small blueward shift of the giant branch is in the direction expected from the "higher mass" turn-off stars. The luminosity and effective temperature of the clump of stars at the horizontal branch is also unaffected. Furthermore, the time scales for these three evolutionary stages are reduced by the same factor so that the relative number densities of stars in each of these stages is unchanged. Consequently, we would be unable to detect a higher value of G in a nearby cluster.

A series of metal-poor BDI stellar tracks were computed from the main sequence to the base of the giant branch in order to examine in detail the effects of BDI on the turn-off and sub-giant regions of globular clusters. At the present epoch ($G = G_0$) there were no detectable differences between the BDI and STD model globular clusters except for the apparent ages. The BDI model ages faster because of the higher G in its early history and, at the present, looks exactly like a slightly older STD model.

Both STD and BDI galaxies were synthesized from the stellar tracks assuming a single generation of solar-abundance stars and the same cosmological model--where applicable--for both types of galaxies. The BDI galaxy ages faster than the STD one and appears redder in all colors at the present epoch. Both models can be fitted to the observed broad-band colors of giant ellipticals, and both exhibit almost parallel evolution of these colors with redshift. The V-magnitude evolution with redshift of both models is nearly the same for steep initial functions, but the BDI model brightens more slowly for shallower initial mass functions. In the latter case the difference in magnitude evolution runs counter to that expected from $L \sim G^{+a}$. Although the true deceleration parameter in these cosmological models is $q_0^{true} \simeq \frac{1}{2} \cdot \Omega = 0.1$, the observed value will be $q_0^{obs} = 1.1 \pm 0.5$ because the luminosity of both model galaxies increases with redshift.

Thus, the Brans-Dicke cosmological models with higher values of G in the past history of the universe do not behave in a simple manner. In fact, many of the G-effects cancel with one another and leave a very small net effect upon the observable quantities. In comparing a star or a galaxy of stars evolved under a higher G with those evolved under a constant G, the only definitive statement which can be made is that the high-G system has evolved faster and appears older.

APPENDIX A. THE STELLAR EVCLUTION CODE

§1. Linearization of the Stellar Structure Equations

The equations of stellar structure (Schwarzschild 1958) are solved for a one-dimensional stellar model. The dependent variables to be solved for are pressure P, temperature T, radius R, and luminosity L; the independent variable is chosen to be $s \equiv \log(\text{mass})$. The differential equations can then be expressed as,

$$\underline{P} \equiv \partial \log P/\partial s = -Gm^2/4\pi PR^4 \qquad (1)$$

$$\underline{T} \equiv \partial \log T/\partial s = \nabla \cdot \partial \log P/\partial s$$

$$\nabla \equiv \partial \ell n T/\partial \ell n P = \nabla_c \quad \text{(convective, see §4.d)} \qquad (2)$$

$$\nabla_r = (3L_\theta/16\pi ac)\cdot(\kappa LP/GmT^4) \quad \text{(radiative)}$$

$$\underline{R} \equiv \partial \log R/\partial s = m/4\pi\rho R^3 \qquad (3)$$

$$\underline{L} \equiv \partial L/\partial s = \ell n 10 \cdot (m/L_\theta)\cdot(\varepsilon - T\cdot dS/dt)\ . \qquad (4)$$

All units are in cgs, except for the luminosity which is in solar units ($L_\theta = 3.90\cdot 10^{33}$ erg/s). All other symbols have their conventional meanings.

The construction of a stellar model begins by dividing the star into M mass shells which are assigned a value $s_i = \log m_i$, where m_i is the interior mass at the midpoint of shell i. A starting--or previous in evolutionary time--model is supplied with a run of ($\log P_i$, $\log T_i$, $\log R_i$, L_i) for i = 1 to M. The differential equations of stellar structure are then linearized with respect to first-order changes in the dependent variables. A set of corrections, ($\delta \log P_i$,

$\delta\log T_i$, $\delta\log R_i$, $\delta\Gamma_i$) for i = 1 to M, is then calculated and applied; the mass and composition remaining fixed at each point. The procedure is iterated until a numerically or physically suitable convergence is reached.

The partial derivatives of the differential equations are required for the linearization. By defining the shorthand notation $\partial_X Y \equiv \partial Y/\partial X$, one can calculate the derivatives as follows.

$$\begin{aligned}
\partial_{\log R}\underline{\underline{P}} &= -4\cdot\ell n10\cdot\underline{\underline{P}} \\
\partial_{\log P}\underline{\underline{P}} &= -\ell n10\cdot\underline{\underline{P}} \\
\partial_{\log T}\underline{\underline{P}} &= \partial_L\underline{\underline{P}} = 0
\end{aligned} \tag{5}$$

$$\begin{aligned}
\partial_{\log R}\underline{\underline{T}}_c &= +\ell n10\cdot\{(\partial\ell n\nabla_c/\partial\ell nR) - 4\}\cdot\underline{\underline{T}}_c \\
\partial_L\underline{\underline{T}}_c &= 0 \qquad \text{(convective)} \\
\partial_{\log P}\underline{\underline{T}}_c &= -\ell n10\cdot\{1 - (\partial\ell n\nabla_c/\partial\ell nP)\}\cdot\underline{\underline{T}}_c \\
\partial_{\log T}\underline{\underline{T}}_c &= +\ell n10\cdot(\partial\ell n\nabla_c/\partial\ell nT)\cdot\underline{\underline{T}}_c
\end{aligned} \tag{6}$$

$$\begin{aligned}
\partial_{\log R}\underline{\underline{T}}_r &= -4\cdot\ell n10\cdot\underline{\underline{T}}_r \\
\partial_L\underline{\underline{T}}_r &= \underline{\underline{T}}_r/L \qquad \text{(radiative)} \\
\partial_{\log P}\underline{\underline{T}}_r &= +\ell n10\cdot(\partial\ell n\kappa/\partial\ell nP)_T\cdot\underline{\underline{T}}_r \\
\partial_{\log T}\underline{\underline{T}}_r &= +\ell n10\cdot\{(\partial\ell n\kappa/\partial\ell nT)_P - 4\}\cdot\underline{\underline{T}}_r
\end{aligned} \tag{6'}$$

$$\begin{aligned}
\partial_{\log R}\underline{\underline{R}} &= -3\cdot\ell n10\cdot\underline{\underline{R}} \\
\partial_L\underline{\underline{R}} &= 0 \\
\partial_{\log P}\underline{\underline{R}} &= -\ell n10\cdot(\partial\ell n\rho/\partial\ell nP)_T\cdot\underline{\underline{R}} \\
\partial_{\log T}\underline{\underline{R}} &= -\ell n10\cdot(\partial\ell n\rho/\partial\ell nT)_P\cdot\underline{\underline{R}}
\end{aligned} \tag{7}$$

$$\begin{aligned}
\partial_{\log R}\underline{\underline{L}} &= \partial_L\underline{\underline{L}} = 0 \\
\partial_{\log P}\underline{\underline{L}} &= \ell n10\cdot\frac{m}{L\theta}\cdot\ell n10\cdot\{(\partial\varepsilon/\partial\ell nP)_T + (\partial\tilde{S}/\partial\ell nP)_T/\Delta t\} \\
\partial_{\log T}\underline{\underline{L}} &= \ell n10\cdot\frac{m}{L\theta}\cdot\ell n10\cdot\{(\partial\varepsilon/\partial\ell nT)_P + (\partial\tilde{S}/\partial\ell nT)_P/\Delta t\}
\end{aligned} \tag{8}$$

The various partial derivatives of the physical quantities are calculated as follows. The equation of state returns ρ, $(\partial\ell n\rho/\partial\ell nT)_P$, c_P, ∇_{ad} and the pressure and temperature derivatives of these quantities. The values of the two partial derivatives of ρ are used directly in equation (7). The opacity routine returns the values of κ, $(\partial\ell n\kappa/\partial\ell nT)_\rho$ and $(\partial\ell n\kappa/\partial\ell n\rho)_T$ from which

$$(\partial\ell n\kappa/\partial\ell nT)_P = (\partial\ell n\kappa/\partial\ell nT)_\rho + (\partial\ell n\kappa/\partial\ell n\rho)_T \cdot (\partial\ell n\rho/\partial\ell nT)_P$$

$$(\partial\ell n\kappa/\partial\ell nP)_T = (\partial\ell n\kappa/\partial\ell n\rho)_T \cdot (\partial\ell n\rho/\partial\ell nP)_T$$

are calculated and used in equation (6'). The energy generation subroutine returns ε, $(\partial\varepsilon/\partial\ell nT)_\rho$ and $(\partial\varepsilon/\partial\ell n\rho)_T$ from which

$$(\partial\varepsilon/\partial\ell nT)_P = (\partial\varepsilon/\partial\ell nT)_\rho + (\partial\varepsilon/\partial\ell n\rho)_T \cdot (\partial\ell n\rho/\partial\ell nT)_P$$

$$(\partial\varepsilon/\partial\ell nP)_T = (\partial\varepsilon/\partial\ell n\rho)_T \cdot (\partial\ell n\rho/\partial\ell nP)_T$$

are calculated and used in equation (8). The derivatives of the convective gradient ∇_c which are used in equation (6) are calculated in the temperature gradient subroutine (§4.d).

The entropy term in the luminosity equations (4 & 8) contains the only explicit reference to any time-dependence in the stellar structure equations. It can be reformulated as follows (Sweigart 1975),

$$\begin{aligned}\tilde{S} &\equiv \Delta t \cdot (-T \cdot dS/dt) \\ &= \Delta t \cdot \{-c_P \cdot dT/dt - (\partial\ell n\rho/\partial\ell nT)_P \cdot (dP/dt)/\rho\} \\ &= \Delta t \cdot \frac{P}{\rho} \cdot (\partial\ell n\rho/\partial\ell nT)_P \cdot \{(d\ell nT/dt)/\nabla_{ad} - (d\ell nP/dt)\} \\ &= \frac{P}{\rho} \cdot (\partial\ell n\rho/\partial\ell nT)_P \cdot \ell n10 \cdot (\Delta\log T/\nabla_{ad} - \Delta\log P),\end{aligned}$$

where Δt is the time elapsed and ($\Delta\log P$, $\Delta\log T$) are the changes between successive models. This formulation has the advantage

that one need not store any quantities from the previous model, but must keep only the sum of the corrections to (log P, log T). The partial derivatives of $\tilde{S}$ are used in equation (8),

$$(\partial\tilde{S}/\partial \ell nT)_P = \tilde{S}\cdot\{-q + (\partial \ell nq/\partial \ell nT)_P\} + (Pq/\rho\nabla_{ad})\cdot\{1 - (\partial \ell n\nabla_{ad}/\partial \ell nT)_P\cdot \ell n10\cdot\Delta \log T\}$$

$$(\partial\tilde{S}/\partial \ell nP)_T = \tilde{S}\cdot\{1 - (\partial \ell n\rho/\partial \ell nP)_T + (\partial \ell nq/\partial \ell nP)_T\} + (Pq/\rho)\cdot\{-1 - (\partial \ell n\nabla_{ad}/\partial \ell nP)_T\cdot \ell n10\cdot\Delta \log T/\nabla_{\ldots}\}$$

where $q \equiv (\partial \ell n\rho/\partial \ell nT)_P$.

For the rest of this section and the following section I shall adopt the shorthand notation of P = log(pressure), T = log(temperature) and R = log(radius). One now sets up and solves the difference equations for corrections to the dependent variables of the starting model (Henyey, Forbes and Gould 1964). Ideally, one wants the differences in (P,T,R,L) between two successive mass points to be determined by the stellar structure differential equations (1-4), e.g.,

$$(P_i - P_{i-1})/(s_i - s_{i-1}) \simeq \tfrac{1}{2}\{(dP/ds)_i + (dP/ds)_{i-1}\} \simeq \tfrac{1}{2}\cdot(\underline{\underline{P}}_i + \underline{\underline{P}}_{i-1}) \qquad 1<i\leq M.$$

Thus, one can define a set of functions for every pair of adjacent mass points,

$$F_P^i \equiv (P_i - P_{i-1}) - \tfrac{1}{2}\Delta s_i\cdot(\underline{\underline{P}}_i + \underline{\underline{P}}_{i-1}) \tag{9}$$

$$F_T^i \equiv (T_i - T_{i-1}) - \tfrac{1}{2}\Delta s_i\cdot(\underline{\underline{T}}_i + \underline{\underline{T}}_{i-1}) \tag{10}$$

$$F_R^i \equiv (R_i - R_{i-1}) - \tfrac{1}{2}\Delta s_i\cdot(\underline{\underline{R}}_i + \underline{\underline{R}}_{i-1}) \tag{11}$$

$$F_L^i \equiv (L_i - L_{i-1}) - \tfrac{1}{2}\Delta s_i\cdot(\underline{\underline{L}}_i + \underline{\underline{L}}_{i-1}) \ , \tag{12}$$

where $\Delta s_i \equiv (s_i - s_{i-1})$ and i = 2 to M. One wants then to solve for the set of (P_i, T_i, R_i, L_i) such that $F_P^i = F_T^i = F_R^i = F_L^i = 0$ The linearization of equations (9-12) with respect to

$(\delta P_i, \delta T_i, \delta R_i, \delta L_i)$ yields 4M-4 equations for the 4M unknowns. The 4 additional equations are supplied by the boundary conditions at the center,

$$s = 3\cdot R + \log(4\pi\rho/3) \;\rightarrow\; F_R^1 \equiv R_1 - \{s_1 - \log(4\pi\rho/3)\}/3 \tag{13}$$

$$L\cdot L_\theta = m\cdot(\varepsilon - T\cdot dS/dt) \;\rightarrow\; F_L^1 \equiv L_1 - \frac{m}{L_\theta}\cdot(\varepsilon - T\cdot dS/dt)_1$$

$$= L_1 - \underline{L}_1/\ell n10 \,, \tag{14}$$

and those at the surface (§3),

$$F_R^{M+1} \equiv R_M - a_1\cdot P_M - a_2\cdot T_M - a_3 \tag{15}$$

$$F_L^{M+1} \equiv L_M\cdot \ell n10\cdot(\log L_M - a_4\cdot P_M - a_5\cdot T_M - a_6). \tag{16}$$

The F equations are linearized,

$$\sum_{j=1}^{M}\left(\frac{\partial F^i}{\partial R_j}\cdot\delta R_j + \frac{\partial F^i}{\partial L_j}\cdot\delta L_j + \frac{\partial F^i}{\partial P_j}\cdot\delta P_j + \frac{\partial F^i}{\partial T_j}\cdot\delta T_j\right) = -F^i \tag{16}$$

where i = 2 to M and the summation over j has non-zero terms only for j = i-1,i. Including the boundary equations, one now calculates the corrections to the previous model by solving a system of 4M equations in 4M unknowns.

§2. Solution of the Linearized Equations

Rather than solving the 4M by 4M system of equations directly, one takes advantage of the specific form of the equations and especially of the large number of zero elements in the matrix (i.e., only 8 by 4M elements are non-zero at most). The matrix is reduced in a forward direction (i=2→M) as the coefficients are defined and is then solved in the backward direction (i=M→1) for the corrections $(\delta P_i, \delta T_i, \delta R_i, \delta L_i)$.

The linearized form of the central boundary conditions (equations 13 & 14) and of the F equations (9-12) is shown

explicitly in figure 1.a; that of the surface boundary conditions, in figure 1.b. The matrix form of the first set of these equations is outlined schematically in figure 2.a, where the zeros and ones are written explicitly and the x's denote any possible non-zero number. The reduction procedure begins: (i) using the boundary conditions, eliminate the first two columns; (ii) continue diagonalizing the four bottom rows; (iii) store the right-hand side and the elements in the two rightmost columns. This method is outlined in figure 2. After this reduction is completed, the bottom two rows become the "boundary equations" for the F equations of the next pair of mass points. The method is repeatedly applied until the surface is reached, whereupon the surface boundary conditions complete the set of 4M equations. For the back solution (i) the values of $(\delta P_M, \delta T_M)$ are first calculated, (ii) then the values of $(\delta R_i, \delta L_i, \delta P_{i-1}, \delta T_{i-1})$ for i = M to 2 are calculated using the stored elements of the array and $(\delta P_i, \delta T_i)$, (iii) and finally the values of $(\delta R_1, \delta L_1)$ are computed from the central boundary condition and the values of $(\delta P_1, \delta T_1)$. This procedure for a 3-point stellar model is outlined in figure 3.

The set of corrections just computed $(\delta P_i, \delta T_i, \delta R_i, \delta L_i)$--or a fraction thereof--are applied to the dependent variables. The entire procedure is repeated until either the corrections or the right-hand side (i.e., the F functions) fall below a preassigned level. At this point the model is assumed to be converged.

The reduction procedure is outlined in full since the technique is not clearly explained in most references. The form chosen for the F equations (9-12) is different from most other methods which use the form,

$$F_P^{i\,\prime} = (P_i - P_{i-1})/(s_i - s_{i-1}) - \tfrac{1}{2}(\underline{\underline{P}}_i + \underline{\underline{P}}_{i-1}).$$

While both the F and F' equations are mathematically identical, the form used here has numerical advantages. For example, the value of $\underline{\underline{P}}$ ranges several orders of magnitude from the center of the star to the surface while the value of P = log(pressure) has a range less than an order of magnitude (similarly with $\underline{\underline{T}}$ and T, $\underline{\underline{R}}$ and R). Hence, when one is near the correct solution (F = F' = 0), the non-zero values of F and F' due to numerical round-off will be of order $\varepsilon \cdot P$ for F and $\varepsilon \cdot \underline{\underline{P}}$ for F' where ε is the relative machine accuracy. Thus, it is difficult to apply a simple test for convergence of the model on F' throughout the star, but the value of F can be reliably tested (e.g., $|F_P^i| < 20 \cdot \varepsilon$ for i=1,M). This test will determine when the model has converged to the best accuracy possible on a given computer and thus save both the time taken for the back solution and the application of numerically questionable corrections.

Henceforth, the shorthand notation will be dropped, and I shall revert to the notation P = pressure, T = temperature, R = radius and L = luminosity (in solar units as usual).

$$
\begin{pmatrix}
1 & 0 & \frac{1}{3}\left(\frac{\partial \ell n\rho}{\partial \ell nP}\right)_{T,1} & \frac{1}{3}\left(\frac{\partial \ell n\rho}{\partial \ell nT}\right)_{P,1} & 0 & 0 & 0 & 0 \\
0 & 1 & -\frac{1}{\ell n10}\cdot\partial_P \underline{L}_1 & -\frac{1}{\ell n10}\cdot\partial_T \underline{L}_1 & 0 & 0 & 0 & 0 \\
-\sigma\cdot\partial_R \underline{P}_1 & 0 & -\sigma\cdot\partial_P \underline{P}_1 - 1 & 0 & -\sigma\cdot\partial_R \underline{P}_2 & 0 & -\sigma\cdot\partial_P \underline{P}_2 + 1 & 0 \\
-\sigma\cdot\partial_R \underline{T}_1 & -\sigma\cdot\partial_L \underline{T}_1 & -\sigma\cdot\partial_P \underline{T}_1 & -\sigma\cdot\partial_T \underline{T}_1 - 1 & -\sigma\cdot\partial_R \underline{T}_2 & -\sigma\cdot\partial_L \underline{T}_2 & -\sigma\cdot\partial_P \underline{T}_2 & -\sigma\cdot\partial_T \underline{T}_2 + 1 \\
-\sigma\cdot\partial_R \underline{R}_1 - 1 & 0 & -\sigma\cdot\partial_P \underline{R}_1 & -\sigma\cdot\partial_T \underline{R}_1 & -\sigma\cdot\partial_R \underline{R}_2 + 1 & 0 & -\sigma\cdot\partial_P \underline{R}_2 & -\sigma\cdot\partial_T \underline{R}_2 \\
0 & -1 & -\sigma\cdot\partial_P \underline{L}_1 & -\sigma\cdot\partial_T \underline{L}_1 & 0 & 1 & -\sigma\cdot\partial_P \underline{L}_2 & -\sigma\cdot\partial_T \underline{L}_2
\end{pmatrix}
\cdot
\begin{pmatrix}
\delta R_1 \\ \delta L_1 \\ \delta P_1 \\ \delta T_1 \\ \delta R_2 \\ \delta L_2 \\ \delta P_2 \\ \delta T_2
\end{pmatrix}
= -
\begin{pmatrix}
F_R^1 \\ F_L^1 \\ F_P^2 \\ F_T^2 \\ F_R^2 \\ F_L^2
\end{pmatrix}
$$

$$\{\ \sigma \equiv \tfrac{1}{2}\cdot(s_2 - s_1)\ \}$$

(a)

$$
\begin{aligned}
1\cdot\delta R_M \quad &+0\cdot\delta L_M \quad -a_1\cdot\delta P_M \quad -a_2\cdot\delta T_M = -F_R^{M+1} \\
0\cdot\delta R_M \quad &+1\cdot\delta L_M \quad -L_M\cdot\ell n10\cdot a_4\cdot\delta P_M \quad -L_M\cdot\ell n10\cdot a_5\cdot\delta T_M = -F_L^{M+1}
\end{aligned}
$$

(b)

Fig.1.---The linearized stellar structure equations for (a) the interior boundary with the first two Henyey points and for (b) the surface boundary at the outermost Henyey point.

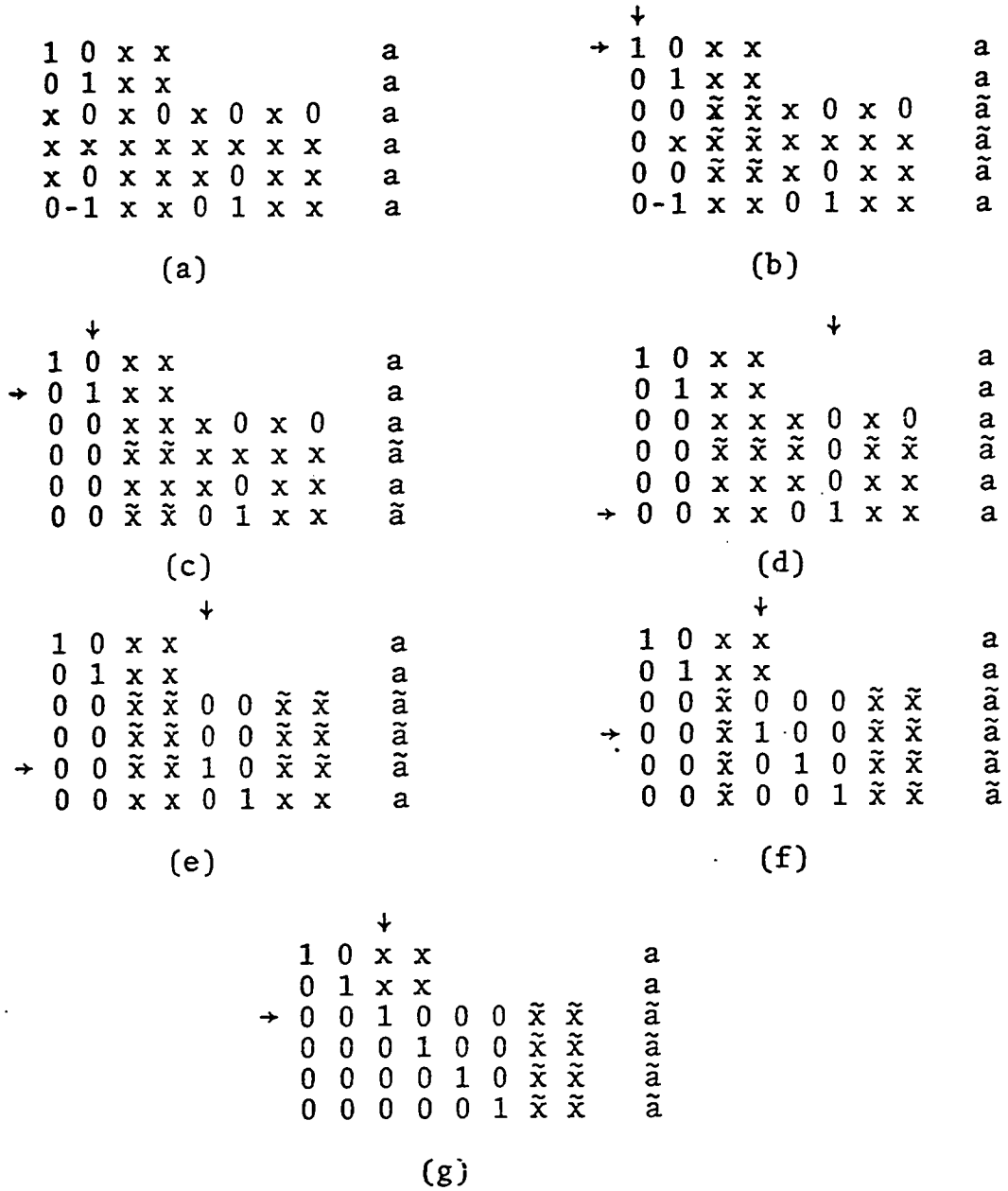

Fig.2.---The reduction algorithm. This technique is applied to the linearized equations for each pair of interior mass points from the center to the surface. The matrix block is denoted by 0's, 1's, and x's ($0 \neq x \neq 1$); the right-hand side,by a's. The first two lines are either the central boundary condition or the last two lines from the previous reduction. The scheme proceeds from (a) through (g). The pivotal element is denoted by arrows; the elements changed through pivoting, by $\tilde{x}$ or $\tilde{a}$.

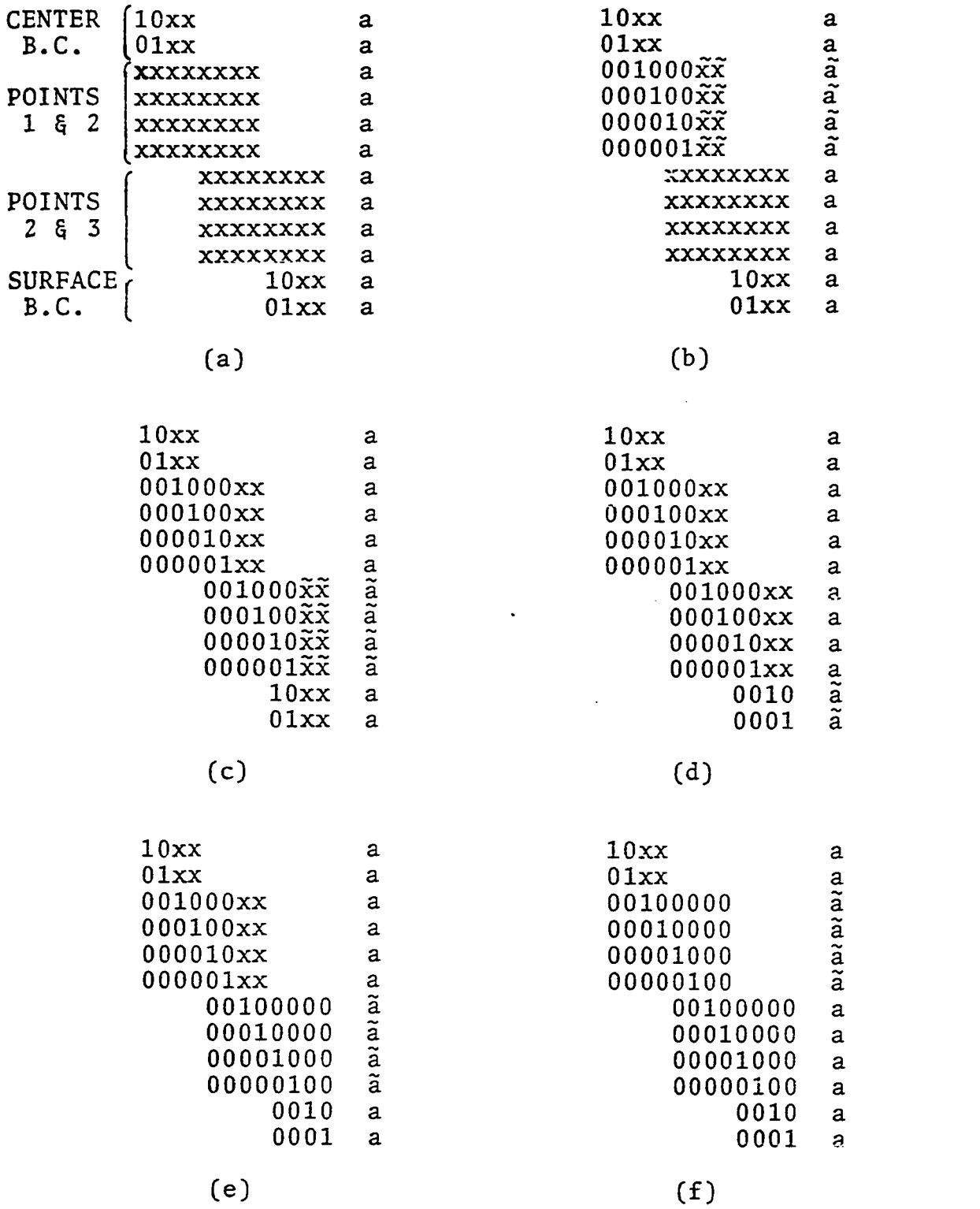

Fig.3.---Schematic Henyey solution for a 3-point star. The notation is the same as in fig. 2. The final reduction to the identity matrix is not shown.

§3. The Boundary Conditions and the Envelope Integrations

The application of the central boundary conditions has been described explicitly in the previous sections and is based upon a first-order integration at the center of the star. The radius equation is calculated from

$$dm = 4\pi\rho R^2 dR \rightarrow \int_0^{m_1} dm = 4\pi\rho_1 \int_0^{R_1} R^2 dR$$

$$\rightarrow m_1 = \frac{4\pi}{3}\cdot\rho_1 R_1^3 ,$$

assuming that $\rho = \rho_1$ is constant for $0 < m < m_1$. Likewise, the luminosity equation assumes that $(\varepsilon + T\cdot dS/dt)$ is constant.

$$dL\cdot L_\theta = (\varepsilon + T\cdot dS/dt)dm \rightarrow L_1 = \frac{m}{L_\theta}\cdot(\varepsilon + T\cdot dS/dt)_1$$

The surface boundary conditions are more complicated and require the integration of model atmospheres and envelopes. Given the (log L, log T_{eff}) and the total mass M, the radius at the base of the atmosphere ($\tau \simeq 2/3$) is determined by $L\cdot L_\theta = 4\pi R^2\cdot\sigma T_{eff}^4$, and the surface gravity is calculated from $g = GM/R^2$. The atmospheric values of P are computed by integrating log P vs. log τ from $\tau << 1$ to $\tau = 2/3$ for a plane parallel atmosphere.

$$d\log P/d\log\tau = gP/\kappa\tau \qquad (17)$$

The atmosphere is assumed to obey a scaled solar $T(\tau)$ relation, which in this case is assumed to be that given by Krishna-Swamy (1966).

$$T^4(\tau) = \frac{3}{4}\cdot T_{eff}^4\cdot(\tau + 1.39 - 0.815\cdot\exp\{-2.54\cdot\tau\} - 0.025\cdot\exp\{-30.0\cdot\tau\}) \qquad (18)$$

The starting values of (P_0, τ_0) are chosen by selecting a small density ρ_0 and then computing,

$$P_0 = (a/3)\cdot T_0^4 + \rho_0 \mathcal{R} T_0 \ .$$

where $T_0 \equiv T(\tau=0)$. Then (P_0, T_0) gives ρ_1 which gives $\kappa_0(\rho_1, T_0)$ which gives $\tau_0 = \kappa_0 P_0/g$. This method could be iterated upon by redefining $T_1 = T(\tau_0)$ and so forth, but sufficient accuracy was achieved in the atmosphere integration by choosing a small enough ρ_0 (e.g., $\rho_0 = 10^{-10}$) such that $\tau < 10^{-4}$.

The envelope integration continues the atmosphere integration deeper into the star using the spherical stellar structure equations (Schwarzschild 1958) with log P as the independent variable and assuming a constant luminosity.

$$d\log T/d\log P = \nabla \qquad (19)$$

$$d\log R/d\log P = -PR/Gm\rho \qquad (20)$$

$$d\log m/d\log P = -4\pi R^4 P/Gm^2 \qquad (21)$$

The values of (P,T) at the base of the atmosphere, the value of R from (log L, log T_{eff}), and the total mass M are used for starting values. The integration is continued inward until the mass value of the outermost point in the model is reached.

The integration procedure of Bulirsch and Stoer (1966) was adopted for both integrations. This method uses polynomial extrapolation based on the mid-point rule. It is self-starting and automatically readjusts the present step size and estimates the subsequent step size in order to comply with the specified accuracy. Since the entire code with the exception of the s = log(mass) values is in single precision, the best feasible relative accuracy was found by experiment to be $\varepsilon \simeq 3\cdot 10^{-4}$ for both the atmosphere and the envelope.

The values of (P,T,R) at the base of the envelope for three envelope calculations are needed in order to compute the surface boundary coefficients (Kippenhahn 1967). One solves the following system,

$$\begin{pmatrix} \log P_1 & \log T_1 & 1 \\ \log P_2 & \log T_2 & 1 \\ \log P_3 & \log T_3 & 1 \end{pmatrix} \cdot \begin{pmatrix} a_1 & a_4 & a_7 \\ a_2 & a_5 & a_8 \\ a_3 & a_6 & a_9 \end{pmatrix} = \begin{pmatrix} \log R_1 & \log L_1 & \log T_{eff_1} \\ \log R_2 & \log L_2 & \log T_{eff_2} \\ \log R_3 & \log L_3 & \log T_{eff_3} \end{pmatrix} \quad (22)$$

for the a_i's which are used for the surface boundary conditions,

$$\log R = a_1 \cdot \log P + a_2 \cdot \log T + a_3 \quad (23)$$

$$\log L = a_4 \cdot \log P + a_5 \cdot \log T + a_6 \quad (24)$$

and for the calculation of the effective temperature,

$$\log T_{eff} = a_7 \cdot \log P + a_8 \cdot \log T + a_9 \ . \quad (25)$$

Here, the (log P, log T) refer to the values at the outermost mass point in the model.

The initial model with an estimated (log L*, log T_{eff}*) is triangulated in the (log L, log T_{eff})-plane by constructing three envelopes of the form

E1: (log L* - ½Δ_L, log T_{eff}* + ½Δ_T)

E2: (log L* - ½Δ_L, log T_{eff}* - ½Δ_T)

E3: (log L* + ½Δ_L, log T_{eff}*) .

If subsequent models or if the model itself during convergence moves significantly out of the triangle, the triangle is flipped until it once again contains the model. The decision as to which point of the triangle should be flipped--if any--can be made by testing,

$$c_i = f \cdot \{(\log L_{i+1} - \log L_{i+2}) \cdot (\log T_{eff} - \log T_{eff_{i+1}}) + (\log T_{eff_{i+2}} - \log T_{eff_{i+1}}) \cdot (\log L - \log L_{i+1})\},$$

where $f = \pm 1$ is the orientation of the triangle (e.g., in the example given $f = +1$) and $\{i,i+1,i+2\}$ is $\{123\}$, $\{231\}$ or $\{312\}$. The value of c_i is tested against $\varepsilon \cdot \Delta_L \cdot \Delta_T$ where setting $\varepsilon = 0$ gives exact triangulation and $\varepsilon > 0$ allows the point (log L, log T_{eff}) to be at most ε of a triangle outside. Begin testing with $i = 1$ to 3, if $c_i < -\varepsilon \cdot \Delta_L \cdot \Delta_T$ then flip point i,

$$\log L_i = \log L_{i+1} + \log L_{i+2} - \log L_i$$

$$\log T_{eff_i} = \log T_{eff_{i+1}} + \log T_{eff_{i+2}} - \log T_{eff_i}$$

$$f = -f$$

and repeat the testing again starting with $i = 1$ until c_i passes for $i = 1$ to 3. The envelopes that have been flipped are then recomputed as are all the coefficients a_i. The flipping of the triangle instead of the recomputation of three new envelopes about the projected values of (log L*, log T_{eff}*) often allows previous envelope calculations to be used in the new triangle, thus saving costly envelope integrations. However, if any overall parameter such as the mass value of the outermost point or the gravitational constant changes significantly between models, then all three envelopes in the new triangle must be recomputed.

The consistency of the envelope integrations with respect to the interior solution has been tested by shifting the outermost point in the model by over two decades in pressure. The resulting model differences are of the order 10^{-4} or less in (log L, log T_{eff}, log R).

4. The Local Physics

a) Saha Equation

In solving the Saha equation for ionization of the stellar material, I followed the notation of Baker and Kippenhahn (1962). The form of the solution and the linearization is due to Sweigart (1974). Define the following quantities,

$x_i^r \equiv$ fraction of atoms of type i in r^{th} ionization state,

$\nu_i \equiv$ number fraction of atoms of type i,

$U_i^r \equiv$ degeneracy of r^{th} ionization state of atom i,

$\chi_i^r \equiv$ ionization energy of r^{th} ionization state of atom i,

$E \equiv$ number of free electrons per nucleus,

$$K_i^r \equiv \frac{U_i^{r+1}}{U_i^r} \cdot \frac{2}{\beta P} \cdot \frac{(2\pi m_e)^{3/2} (kT)^{5/2}}{h^3} \cdot \exp\{-\chi_i^r/kT\}$$

then it follows that

$$\frac{x_i^r}{x_i^r} \cdot \frac{E}{E+1} = K_i^r \qquad (a.1)$$

$$\sum_{r=0} x_i^r = 1 \qquad (a.2)$$

$$E = \sum_{i=1}^{N} \{\nu_i \cdot \sum_{r=0} r \cdot x_i^r\} \; . \qquad (a.3)$$

In the solution presented here, the formation of H_2 and H^- as well as pressure ionization will ignored. All metals will be considered as only singly ionized at most, and thus hydrogen can be treated as a metal. Henceforth, the subscript z shall refer to all metals and hydrogen--everything but helium.

Using equations (a.1-a.3), one can derive the following expressions,

$$x_z^0 + x_z^1 = 1$$

$$x_y^0 + x_y^1 + x_y^2 = 1$$

where y refers to helium,

$$x_z^1 \cdot \frac{E}{1+E} = K_z^0 \cdot (1 - x_z^1) \qquad (a.4)$$

$$x_y^1 \cdot \frac{E}{1+E} = K_y^0 \cdot (1 - x_y^1 - x_y^2) \qquad (a.5)$$

$$x_y^2 \cdot \frac{E}{1+E} = K_y^1 \cdot x_y^1 \ . \qquad (a.6)$$

$$E = \nu_y \cdot (x_y^1 + 2 \cdot x_y^2) + \sum_z \nu_z x_z^1 \ . \qquad (a.7)$$

Equations (a.4-a.7) give (3+N) equations for the (3+N) unknowns: E, x_y^1, x_y^2, x_z^1, where there are N metals including hydrogen. Since the values of K are fixed for a given (P,T), the values of x_z^1 can be solved for directly as a function of E.

$$x_z^1 = K_z^0/(K_z^0 + E/(1+E)) \qquad (a.8)$$

We now have three equations to solve.

$$0 = E - \{\nu_y \cdot (x_y^1 + 2 \cdot x_y^2) + \sum_z \nu_z x_z\} \qquad (a.9)$$

$$0 = K_y^0 \cdot (1 - x_y^1 - x_y^2) - x_y^1 \cdot E/(1+E) \qquad (a.10)$$

$$0 = K_y^1 \cdot x_y^1 - x_y^2 \cdot E/(1+E) \qquad (a.11)$$

Given initial estimates of (E, x_y^1, x_y^2), one can linearize equations (a.9-a.11) and solve for corrections to the initial (E, x_y^1, x_y^2). The variation of the x_z^1 can be expressed as changes in E by

$$\partial x_z^1/\partial E = (1+E)^{-2} \cdot x_z^1/(K_z^0 + E/(1+E))$$

$$= x_z^1 \cdot (1 - x_z^1)/(E \cdot (1+E)) \ . \qquad (a.12)$$

Care must be taken so that $(1 - x_z^1)$ is numerically well defined in the limit of full ionization, i.e.,

$$(1 - x_z^1) = E/\{(1+E)\cdot(K_z^0 + E/(1+E))\}.$$

One then has the following matrix equation.

$$\begin{bmatrix} 2\cdot\nu_y & \nu_y & -1-\sum_z \nu_z x_z^1(1-x_z^1)/(E\cdot(1+E)) \\ K_y^0 & K_y^0+E/(1+E) & x_y^1/(1+E)^2 \\ E/(1+E) & -K_y^1 & x_y^2/(1+E)^2 \end{bmatrix} \times \begin{bmatrix} \Delta x_y^2 \\ \Delta x_y^1 \\ \Delta E \end{bmatrix}$$

$$= \begin{bmatrix} E - \{\nu_y\cdot(x_y^1 + 2\cdot x_y^2) + \sum_z \nu_z x_z^1\} \\ K_y^0\cdot(1 - x_y^1 - x_y^2) - x_y^1\cdot E/(1+E) \\ K_y^1\cdot x_y^1 - x_y^2\cdot E/(1+E) \end{bmatrix} \qquad \text{(a.13)}$$

After iteratively solving equation (a.13) until convergence, one now needs the temperature derivatives of the basic quantities and their linearization with respect to P and T for the overall Henyey scheme. Since we have solved for the correct values of (E, x_y^1, x_y^2) which satisfy equations (a.9-a.11), we may differentiate the equations to solve for the derivatives of (E, x_y^1, x_y^2). Let q be any arbitrary variable and $\partial_q \equiv \partial/\partial q$, then

$$\nu_y\cdot\partial_q x_y^1 + 2\cdot\nu_y\cdot\partial_q x_y^2 - \partial_q E + \sum_z \nu_z\cdot\partial_q x_z^1 = 0 \qquad \text{(a.14)}$$

$$(K_y^0+E/(1+E))\cdot\partial_q x_y^1 + K_y^0\cdot\partial_q x_y^2 + x_y^1\cdot(1+E)^{-2}\cdot\partial_q E = (1 - x_y^1 - x_y^2)\cdot\partial_q K_y^0 \qquad \text{(a.15)}$$

$$-K_y^1\cdot\partial_q x_y^1 + E\cdot(1+E)^{-1}\cdot\partial_q x_y^2 + x_y^2\cdot(1+E)^{-2}\cdot\partial_q E = x_y^1\cdot\partial_q K_y^1 \ . \qquad \text{(a.16)}$$

By substituting the value of

$$\partial_q x_z^1 = x_z^1\cdot(1 - x_z^1)\cdot\{\partial_q \ell n K_z^0 - \partial_q E/(E\cdot(1+E))\} \qquad \text{(a.17)}$$

into equation (a.14), one sees that the coefficient matrix C of $(\partial x_y^2/\partial q,\ \partial x_y^1/\partial q,\ \partial E/\partial q)$ is the same as the initial coefficient matrix of equation (a.13).

$$C \times \begin{bmatrix} \partial x_y^2/\partial q \\ \partial x_y^1/\partial q \\ \partial E/\partial q \end{bmatrix} = \begin{bmatrix} -\sum_z \{\nu_z x_z^1 (1 - x_z^1) \cdot (\partial \ell n K_z^0/\partial q)\} \\ +K_y^0 \cdot (1 - x_y^1 - x_y^2) \cdot (\partial \ell n K_y^0/\partial q) \\ +K_y^1 \cdot x_y^1 \cdot (\partial \ell n K_y^1/\partial q) \end{bmatrix} \quad (a.18)$$

Thus, one can use the matrix reduction which was previously calculated in the final iteration of equation (a.13) with the new right-hand side of equation (a.18) to solve for the derivatives.

The second derivatives can also be calculated as follows.

$$\nu_y \cdot (\partial/\partial p(\partial x_y^1/\partial q)) + 2 \cdot \nu_y \cdot (\partial/\partial p(\partial x_y^2/\partial q)) - (\partial/\partial p(\partial E/\partial q)) + \sum_z \{\nu_z \cdot (\partial/\partial p(\partial x_z^1/\partial q))\} = 0 \quad (a.19)$$

$$\{K_y^0 + E/(1+E)\} \cdot (\partial/\partial p(\partial x_y^1/\partial q)) + K_y^0 \cdot (\partial/\partial p(\partial x_y^2/\partial q)) + (1+E)^{-2} \cdot x_y^1 \cdot (\partial/\partial p(\partial E/\partial q)) = (1-x_y^1-x_y^2) \cdot (\partial/\partial p(\partial K_y^0/\partial q)) - (\partial x_y^1/\partial p + \partial x_y^2/\partial p) \cdot (\partial K_y^0/\partial q) - (\partial x_y^1/\partial q + \partial x_y^2/\partial q) \cdot (\partial K_y^0/\partial p) + (1+E)^{-2} \cdot \{(1+E)^{-1} \cdot 2 \cdot x_y^1 \cdot (\partial E/\partial p) \cdot (\partial E/\partial q) - (\partial x_y^1/\partial p) \cdot (\partial E/\partial q) - (\partial x_y^1/\partial q) \cdot (\partial E/\partial p)\} \quad (a.20)$$

$$-K_y^1 \cdot (\partial/\partial p(\partial x_y^1/\partial q)) + E \cdot (1+E)^{-1} \cdot (\partial/\partial p(\partial x_y^2/\partial q)) + (1+E)^{-2} \cdot x_y^2 \cdot (\partial/\partial p(\partial E/\partial q)) = x_y^1 \cdot (\partial/\partial p(\partial K_y^1/\partial q)) + (\partial x_y^1/\partial p) \cdot (\partial K_y^1/\partial q) + (\partial x_y^1/\partial q) \cdot (\partial K_y^1/\partial p) + (1+E)^{-2} \cdot \{(1+E)^{-1} \cdot 2 \cdot x_y^2 \cdot (\partial E/\partial p) \cdot (\partial E/\partial q) - (\partial x_y^2/\partial p) \cdot (\partial E/\partial q) - (\partial x_y^2/\partial q) \cdot (\partial E/\partial p)\} \quad (a.21)$$

Once again, by substituting

$$(\partial/\partial p(\partial x_z^1/\partial q) = x_z^1 \cdot (1-x_z^1) \cdot \{E \cdot (1+E)\}^{-2} \cdot \{-(\partial/\partial p(\partial E/\partial q)) + (1+2E) \cdot (\partial E/\partial p) \cdot (\partial E/\partial q) + (\partial/\partial p(\partial \ell n K_z^0/\partial q))\} + (1-2x_z^1) \cdot (\partial x_z^1/\partial p) \cdot \{\partial \ell n K_z^0/\partial q - (\partial E/\partial q)/(E+E^2)\} \quad (a.22)$$

into equation (a.19), one arrives at the matrix equation for the second derivatives.

$$C \times \begin{Vmatrix} (\partial/\partial p(\partial x_y^2/\partial q)) \\ (\partial/\partial p(\partial x_y^1/\partial q)) \\ (\partial/\partial p(\partial E/\partial q)) \end{Vmatrix} =$$

$$\begin{Vmatrix} -\sum_z \nu_z \cdot \left(x_z^1 \cdot (1-x_z^1) \cdot \{(\partial/\partial p(\partial \ell nK_z^0/\partial q)) + (1+2E) \cdot (E+E^2)^{-2} \cdot (\partial E/\partial p) \right. \\ \left. \cdot (\partial E/\partial q)\} + (1-2x_z^1) \cdot (\partial x_z^1/\partial p) \cdot \{(\partial \ell nK_z^0/\partial q) \right. \\ \left. - (\partial E/\partial q)/(E+E^2)\}\right) \\ \\ (1-x_y^1-x_y^2) \cdot (\partial/\partial p(\partial K_y^0/\partial q)) - (\partial x_y^1/\partial p + \partial x_y^2/\partial p) \cdot (\partial K_y^0/\partial q) \\ - (\partial x_y^1/\partial q + \partial x_y^2/\partial q) \cdot (\partial K_y^0/\partial p) + (1+E)^{-2} \cdot \{(1+E)^{-1} \cdot 2 \cdot x_y^1 \\ \cdot (\partial E/\partial p) \cdot (\partial E/\partial q) - (\partial x_y^1/\partial p) \cdot (\partial E/\partial q) - (\partial x_y^1/\partial q) \cdot (\partial E/\partial p)\} \\ \\ x_y^1 \cdot (\partial/\partial p(\partial K_y^1/\partial q)) + (\partial x_y^1/\partial p) \cdot (\partial K_y^1/\partial q) + (\partial x_y^1/\partial q) \cdot (\partial K_y^1/\partial p) \\ + (1+E)^{-2} \cdot \{(1+E)^{-1} \cdot 2 \cdot x_y^2 \cdot (\partial E/\partial p) \cdot (\partial E/\partial q) \\ - (\partial x_y^2/\partial p) \cdot (\partial E/\partial q) - (\partial x_y^2/\partial q) \cdot (\partial E/\partial p)\} \end{Vmatrix} \tag{a.23}$$

The derivatives of K which are used in the previous equations can be easily found,

$$(\partial \ell nK/\partial \ell nT) = 5/2 + 4(1-\beta)/\beta + \chi/kT \tag{a.24}$$

$$(\partial \ell nK/\partial \ell nP) = -1 - (1-\beta)/\beta = -1/\beta \tag{a.25}$$

$$(\partial/\partial \ell nT(\partial \ell nK/\partial \ell nT)) = 16(1-\beta)/\beta^2 - \chi/kT \tag{a.26}$$

$$(\partial/\partial \ell nP(\partial \ell nK/\partial \ell nT)) = -4(1-\beta)/\beta^2 \ ,$$

and can be put in the form

$$(\partial/\partial p(\partial K/\partial q)) = K \cdot \{(\partial/\partial p(\partial \ell nK/\partial q)) + (\partial \ell nK/\partial p) \cdot (\partial \ell nK/\partial q)\}. \tag{a.27}$$

The previous derivations will now allow one to calculate all the necessary properties of a non-degenerate gas for a given (P,T) and composition, including their linearization with respect to (P,T). Let μ_a be the mean atomic weight per

atom and μ_e be the mean weight per electron, then the total mean molecular weight μ can be expressed as

$$\frac{1}{\mu} = \frac{1}{\mu_a} + \frac{1}{\mu_e} = \frac{1}{\mu_a} + \frac{E}{\mu_a} = \frac{(1+E)}{\mu_a} \quad . \tag{a.28}$$

Since μ_a is fixed for a given composition, the density can be calculated from

$$\beta P = \mathcal{R}\cdot\rho\cdot T\cdot(1+E)/\mu_a \tag{a.29}$$

where β has the usual definition,

$$\beta \equiv P_{gas}/P = 1 - (a/3)\cdot T^4/P \quad . \tag{a.30}$$

The first and second derivatives of the density are readily calculable.

$$(\partial \ell n\rho/\partial \ell nT)_P = -1 - 4(1-\beta)/\beta - (\partial E/\partial \ell nT)_P/(1+E) \tag{a.31}$$

$$(\partial \ell n\rho/\partial \ell nP)_T = 1/\beta - (\partial E/\partial \ell nP)_T/(1+E) \tag{a.32}$$

$$(\partial/\partial \ell nT(\partial \ell n\rho/\partial \ell nT)_P)_P = -16(1-\beta)/\beta^2 + (\partial E/\partial \ell nT)_P^2/(1+E)^2 - (\partial/\partial \ell nT(\partial E/\partial \ell nT)_P)_P/(1+E) \tag{a.32}$$

$$(\partial/\partial \ell nP(\partial \ell n\rho/\partial \ell nT)_P)_T = +4(1-\beta)/\beta^2 + (\partial E/\partial \ell nP)_T\cdot(\partial E/\partial \ell nT)_P/(1+E)^2 - (\partial/\partial \ell nP(\partial E/\partial \ell nT)_P)_T/(1+E) \tag{a.33}$$

The internal energy of the gas per unit mass is a combination of the gas pressure, the radiation pressure and the ionization energy.

$$U = (\tfrac{3}{2}\cdot P_{gas} + 3\cdot P_{rad} + \sum_i \sum_{r=1} n_i^r \chi'^r_i)/\rho \tag{a.34}$$

n_i^r = number of i-atoms in r^{th} ionization state

$$= \nu_i\cdot x_i^r\cdot\frac{\mathcal{R}}{\mu_a}\cdot\rho\cdot\frac{1}{k}$$

χ'^r_i = total energy of r^{th} state above the ground level

$$= \chi_i^0 + \chi_i^1 + \ldots + \chi_i^{r-1}$$

By noting that $P_{rad} = P_{gas} \cdot (1-\beta)/\beta$ and letting $T_i^r \equiv \chi'^r_i/k$ be the temperature corresponding to the ionization energy, one can express the internal energy as

$$U = \frac{\mathcal{R}}{\mu_a} \cdot \{(3/2 + 3\cdot(1-\beta)/\beta)\cdot(1+E)\cdot T + \sum_i \nu_i \sum_{r=1} x_i^r \cdot T_i^r\} \tag{a.35}$$

and its temperature derivative as

$$(\partial U/\partial T)_P = \frac{\mathcal{R}}{\mu_a} \cdot \{(1+E)\cdot(3/2 + 3\cdot(1-\beta)/\beta + 12\cdot(1-\beta)/\beta^2) + (3/2 + 3\cdot(1-\beta)/\beta)\cdot(\partial E/\partial \ell n T)_P + \sum_i \nu_i \sum_{r=1} (\partial x_i^r/\partial \ell n T)_P \cdot T_i^r/T\}. \tag{a.36}$$

The derivatives of $(\partial U/\partial T)_P$ with respect to ℓn P and ℓn T are then given by

$$\begin{aligned}(\partial/\partial \ell n P(\partial U/\partial T)_P)_T = \frac{\mathcal{R}}{\mu_a} \cdot \Big(& -(1+E)\cdot(24-9\beta)\cdot(1-\beta)/\beta^3 \\ & +(3/2 + 3\cdot(1-\beta)\cdot(4+\beta)/\beta^2)\cdot(\partial E/\partial \ell n P)_T \\ & -3\cdot(1-\beta)\cdot(\partial E/\partial \ell n T)_P/\beta^2 \\ & +(3/2 + 3\cdot(1-\beta)/\beta)\cdot(\partial/\partial \ell n P(\partial E/\partial \ell n T_P)_T \\ & + \sum_i \nu_i \sum_{r=1} (\partial/\partial \ell n P(\partial x_i^r/\partial \ell n T)_P)_T \cdot T_i^r/T \Big)\end{aligned} \tag{a.37}$$

$$\begin{aligned}(\partial/\partial \ell n T(\partial U/\partial T)_P)_P = \frac{\mathcal{R}}{\mu_a} \cdot \Big(& (1+E)\cdot 4\cdot(24-9\beta)\cdot(1-\beta)/\beta^3 \\ & +(3/2 + 3\cdot(1-\beta)\cdot(8+\beta)/\beta^2)\cdot(\partial E/\partial \ell n T)_P \\ & +(3/2 + 3\cdot(1-\beta)/\beta)\cdot(\partial/\partial \ell n T(\partial E/\partial \ell n T)_P)_P \\ & + \sum_i \nu_i \sum_{r=1} \{(\partial/\partial \ell n T(\partial x_i^r/\partial \ell n T)_P)_P - (\partial x_i^r/\partial \ell n T)_P\} \cdot T_i^r/T \Big).\end{aligned} \tag{a.38}$$

The specific heat c_p and the adiabatic gradient ∇_{ad} along with their derivatives are then calculated.

$$c_p = (\partial U/\partial T)_P - (P/\rho T)\cdot(\partial \ell n \rho/\partial \ell n T)_P \tag{a.39}$$

$$\begin{aligned}(\partial \ell n c_p/\partial \ell n P)_T = c_p^{-1} \cdot \{ & (\partial/\partial \ell n P(\partial U/\partial T)_P)_T \\ & -(P/\rho T)\cdot(\partial \ell n \rho/\partial \ell n T)_P \cdot (1 - (\partial \ell n \rho/\partial \ell n P)_T) \\ & -(P/\rho T)\cdot(\partial/\partial \ell n P(\partial \ell n \rho/\partial \ell n T)_P)_T\}\end{aligned} \tag{a.40}$$

$$(\partial \ell n c_p/\partial \ell n T)_p = c_p^{-1} \cdot \{(\partial/\partial \ell n T(\partial U/\partial T)_p)_p + (P/\rho T) \cdot (\partial \ell n \rho/\partial \ell n T)_p \cdot (1 + (\partial \ell n \rho/\partial \ell n T)_p) - (P/\rho T) \cdot (\partial/\partial \ell n T(\partial \ell n \rho/\partial \ell n T)_p)_p\} \quad (a.41)$$

$$\nabla_{ad} = -(P/\rho T) \cdot (\partial \ell n \rho/\partial \ell n T)_p/c_p \quad (a.42)$$

$$(\partial \ell n \nabla_{ad}/\partial \ell n P)_T = 1 - (\partial \ell n \rho/\partial \ell n P)_T - (\partial \ell n c_p/\partial \ell n P)_T + (\partial/\partial \ell n P(\partial \ell n \rho/\partial \ell n T)_p)_T/(\partial \ell n \rho/\partial \ell n T)_p \quad (a.43)$$

$$(\partial \ell n \nabla_{ad}/\partial \ell n T)_p = -1 - (\partial \ell n \rho/\partial \ell n T)_p - (\partial \ell n c_p/\partial \ell n T)_p + (\partial/\partial \ell n T(\partial \ell n \rho/\partial \ell n T)_p)_p/(\partial \ell n \rho/\partial \ell n T)_p \quad (a.44)$$

In the computation of the mean atomic weight, the physical scale of weights is chosen in which $\mathcal{R} = 8.317 \cdot 10^7$ erg/°K/mole. The abundance of metals is taken from the abundances given in the opacity tables of Cox and Stewart (1970).

Element	Z	A	Abundance by Weight Z = .01	Z = .02
H	1	1.0083	-----	-----
He	2	4.0039	-----	-----
C	6	12.0150	0.00141	0.00282
N	7	14.0112	0.00046	0.00092
O	8	16.0045	0.00420	0.00840
Ne	10	20.190	0.00298	0.00597
Na	11	22.997	0.00001	0.00003
Mg	12	24.320	0.00018	0.00036
Al	13	26.990	0.00001	0.00003
Si	14	28.10	0.00026	0.00053
Ar	18	39.960	0.00039	0.00078
Fe	26	55.865	0.00008	0.00017
			Σ = 0.00998	0.02001

The constants used for computing the K's are taken from Allen (1963, p.35).

Element	Z	χ_i^r(e.v.)	$\chi_i^r/k(^0K)$	$\log(2\cdot U^{r+1}/U^r)$*
H	1	13.595	157800	0.00
He	2	24.581	285270	0.60
He^+	2	54.403	631370	0.00
C	6	11.256	130630	0.11
N	7	14.53	168630	0.64
O	8	13.614	158000	-0.04
Ne	10	21.559	250200	1.03
Na	11	5.138	59630	-0.01
Mg	12	7.644	88710	0.60
Al	13	5.984	69450	-0.47
Si	14	8.149	94570	0.08
Ar	18	15.775	183080	0.99
Fe	26	7.87	91330	0.49

* for T = 5040 ^{0}K

b) Fully Ionized Equation of State

The calculation of the density of a fully ionized gas from the pressure, temperature and mean weights (μ_a, μ_e) becomes successively more complex as the electrons become partially degenerate and also partially relativistic. Since the radiation pressure is simply calculable and the nuclei are always assumed to be non-degenerate and non-relativistic, one is left with the calculation of the electron pressure, its derivatives and the internal energy. The method in general is an iterative one which uses an initial estimate of the density to predict an electron pressure and hence a total pressure. The initial density estimate is corrected according to the difference between the given pressure and the predicted pressure.

The equation of state used by this code is taken entirely from the work of Dr. Allen Sweigart (1974) to whom I am greatly indebted. It employs moderately large tables (4300 values) which cover the temperature range log T = 5.20-9.00. The equation of state is correct in the region of partially degenerate, partially relativistic electrons as well as in all the other limiting cases.

The notation and formulation which follow are taken from Sweigart and also from Cox and Giuli (1968). The subscript $_a$ refers to atoms or nuclei; the subscript $_e$, to electrons; and the subscript $_r$, to radiation. By defining,

$$F_N(\eta,\beta) \equiv \int_0^\infty \frac{x^N(1+\frac{1}{2}\beta x)^{\frac{1}{2}}dx}{1+\exp\{-\eta+x\}} \quad , \quad N > -1 \qquad \text{(b.1)}$$

and $\beta \equiv kT/m_e c^2$ (for this section $\beta_r = 1 - (a/3)\cdot T^4/P$) the values of the electron number density n_e, the electron pressure P_e and the electron internal energy per unit mass U_e can be derived.

$$n_e = 4\pi(2m_e kT)^{3/2}h^{-3}\cdot\{F_{1/2}(\eta,\beta) + \beta\cdot F_{3/2}(\eta,\beta)\}$$
$$= C_1\cdot T^{3/2}\cdot\phi(\eta,\beta) \qquad \text{(b.2)}$$

$$P_e = \frac{8\pi}{3}kT(2m_e kT)^{3/2}h^{-3}\cdot\{F_{3/2}(\eta,\beta) + \tfrac{1}{2}\beta\cdot F_{5/2}(\eta,\beta)\}$$
$$= C_2\cdot T^{5/2}\cdot\lambda(\eta,\beta) \qquad \text{(b.3)}$$

$$\rho U_e = \frac{4\pi}{3}kT(2m_e kT)^{3/2}h^{-3}\cdot\{F_{3/2}(\eta,\beta) + \beta\cdot F_{5/2}(\eta,\beta)\}$$
$$= C_3\cdot T^{5/2}\cdot\psi(\eta,\beta) \qquad \text{(b.4)}$$

Then, $\rho/\mu_e = C_4\cdot T^{3/2}\cdot\phi(\eta,\beta)$ where $C_4 = C_1\cdot M_u$ (M_u = mass unit) and

$$\log(\rho/\mu_e) = \log C_4 + \frac{3}{2}\log T + \log\phi(\eta,\beta) \qquad \text{(b.5)}$$

$$\log P_e = \log C_2 + \frac{5}{2}\log T + \log\lambda(\eta,\beta) \qquad \text{(b.6)}$$

$$\log(\mu_e \cdot U_e) = \log C_3 + \frac{5}{2}\log T + \log \psi(\eta,\beta) - \log(\rho/\mu_e) \qquad (b.7)$$

By using the definition of (ρ/μ_e) and β, one can derive

$$(\partial \ell n\beta/\partial \ell nT)_\rho = 1 \quad \text{and} \quad (\partial \ell n\beta/\partial \ell n\rho)_T = 0 \qquad (b.8)$$

and also

$$(\partial \ell n\eta/\partial \ell nT)_\rho = -(3/2 + (\partial \ell n\phi/\partial \ell n\beta)_\eta)/(\partial \ell n\phi/\partial \ell n\eta)_\beta \qquad (b.9)$$

$$(\partial \ell n\eta/\partial \ell n\rho)_T = 1/(\partial \ell n\phi/\partial \ell n\eta)_\beta \qquad (b.10)$$

where

$$(\partial\phi/\partial\eta)_\beta = (\partial F_{1/2}/\partial\eta)_\beta + \beta\cdot(\partial F_{3/2}/\partial\eta)_\beta \qquad (b.11)$$

$$(\partial\phi/\partial\beta)_\eta = (\partial F_{1/2}/\partial\beta)_\eta + F_{3/2} + \beta\cdot(\partial F_{3/2}/\partial\beta)_\eta \qquad (b.12)$$

are readily calculable given the values of η and β. The derivatives of P_e and U_e can then be calculated.

$$(\partial \ell nP_e/\partial \ell nT)_\rho = 5/2 + (\partial \ell n\lambda/\partial \ell nT)_\rho \qquad (b.13)$$
$$= 5/2 + (\partial \ell n\lambda/\partial \ell n\eta)_\beta\cdot(\partial \ell n\eta/\partial \ell nT)_\rho + (\partial \ell n\lambda/\partial \ell n\beta)_\eta$$

$$(\partial \ell nP_e/\partial \ell n\rho)_T = (\partial \ell n\lambda/\partial \ell n\rho)_T$$
$$= (\partial \ell n\lambda/\partial \ell n\eta)_\beta\cdot(\partial \ell n\eta/\partial \ell n\rho)_T \qquad (b.14)$$

$$(\partial \ell nU_e/\partial \ell nT)_\rho = 5/2 + (\partial \ell n\psi/\partial \ell nT)_\rho \qquad (b.15)$$
$$= 5/2 + (\partial \ell n\psi/\partial \ell n\eta)_\beta\cdot(\partial \ell n\eta/\partial \ell nT)_\rho + (\partial \ell n\psi/\partial \ell n\beta)_\eta$$

The following five tables are set up

1. $\log P_e$
2. $\log(\mu_e U_e)$
3. $\log\{P_e\cdot(\partial \ell nP_e/\partial \ell nT)_\rho\}$
4. $(\partial \ell nP_e/\partial \ell n\rho)_T$
5. $\log\{\mu_e U_e\cdot(\partial \ell nU_e/\partial \ell nT)_\rho\}$

These tables are two-dimensional in $X \equiv \log(\rho/\mu_e) - \frac{3}{2}\cdot\log(T)$ and in $Y \equiv \log(T)$. A given (X,Y) value implies a unique (η,β) value from which the $F_N(\eta,\beta)$ functions and their derivatives

may be calculated. These five tables are cross-tabulated at 20 equal intervals in Y from 5.20 to 9.00 and in 43 unequal intervals in X from -16.00 to -3.00. The unequal intervals in X were selected by Sweigart in order best to describe the variations of the five quantities and to achieve maximum accuracy in the tabular interpolation.

Interpolation within the tables uses three points in both X and Y. To calculate a value of F(X,Y) where F is one of the tabulated functions, assume that one has located the bounding table values of X and Y,

$$X_1 \leq X < X_2 < X_3$$

$$Y_1 \leq Y < Y_2 < Y_3$$

and let $F_{ij} \equiv F(X_i,Y_j)$. Since the spacing in Y is uniform, $H \equiv \Delta Y = Y_2-Y_1 = Y_3-Y_2$, one uses Newton's forward interpolation formula,

$$\underline{F}_i = F_{i1} + u\cdot\Delta F_{i1} + \tfrac{1}{2}u(u-1)\cdot\Delta^2 F_{i1} \qquad \text{(b.16)}$$

where

$$u \equiv (Y - Y_1)/H$$

$$\Delta F_{i1} \equiv F_{i2} - F_{i1}, \quad \Delta F_{i2} \equiv F_{i3} - F_{i2}$$

$$\Delta^2 F_{i1} \equiv \Delta F_{i2} - \Delta F_{i1} .$$

Since the spacing in X is non-uniform, one uses Lagrange's interpolation formula,

$$F = L_1\cdot\underline{F}_1 + L_2\cdot\underline{F}_2 + L_3\cdot\underline{F}_3 \qquad \text{(b.17)}$$

where

$$L_i \equiv \{(X - X_{i+1})(X - X_{i+2})\}/\{(X_i - X_{i+1})(X_i - X_{i+2})\}$$

$$\{i \quad i+1 \quad i+2\} = \{123\}, \{231\}, \{312\}$$

One now has the functional value F at (X,Y). The derivatives of F follow from the interpolation formulae used to calculate F.

$$(\partial F/\partial Y)_X = L_1 \cdot (\partial \underline{\underline{F}}_1/\partial Y)_X + L_2 \cdot (\partial \underline{\underline{F}}_2/\partial Y)_X + L_3 \cdot (\partial \underline{\underline{F}}_3/\partial Y)_X$$

$$(\partial \underline{\underline{F}}_i/\partial Y)_X = H^{-1} \cdot \{\Delta F_{i1} + (u-\tfrac{1}{2}) \cdot \Delta^2 F_{i1}\} \qquad (b.18)$$

$$(\partial F/\partial X)_Y = \underline{\underline{F}}_1 \cdot (\partial L_1/\partial X) + \underline{\underline{F}}_2 \cdot (\partial L_2/\partial X) + \underline{\underline{F}}_3 \cdot (\partial L_3/\partial X)$$

$$(\partial L_i/\partial X) = \{(X-X_{i+1}) + (X-X_{i+2})\}/\{(X_i-X_{i+1})(X_i-X_{i+2})\} \qquad (b.19)$$

$$(\partial^2 F/\partial X^2)_Y = \underline{\underline{F}}_1 \cdot (\partial^2 L_1/\partial X^2) + \underline{\underline{F}}_2 \cdot (\partial^2 L_2/\partial X^2) + \underline{\underline{F}}_3 \cdot (\partial^2 L_3/\partial X^2) \qquad (b.20)$$

$$(\partial^2 L_i/\partial X^2) = 2/\{(X_i-X_{i+1})(X_i-X_{i+2})\}$$

The derivatives with respect to ρ and T are then,

$$(\partial F/\partial \log T)_\rho = (\partial F/\partial Y)_X - \tfrac{3}{2} \cdot (\partial F/\partial X)_Y \qquad (b.21)$$

$$(\partial F/\partial \log \rho)_T = (\partial F/\partial X)_Y \qquad (b.22)$$

$$(\partial^2 F/\partial \log \rho^2)_T = (\partial^2 F/\partial X^2)_Y \; . \qquad (b.23)$$

By using the first table ($F = \log P_e$), one can calculate the density derivatives of $\log P_e$ and hence, the density derivatives of the total pressure P.

$$(\partial \log P/\partial \log \rho)_T = \{P_a + P_e \cdot (\partial \log P_e/\partial \log \rho)_T\}/P \qquad (b.24)$$

$$(\partial^2 \log P/\partial \log \rho^2)_T = \ell n 10 \cdot \left[\{P_a + P_e \cdot (\partial \log P_e/\partial \log \rho)_T^2 + P_e \cdot (\partial^2 \log P_e/\partial \log \rho^2)_T/\ell n 10\}/P - (\partial \log P/\partial \log \rho)_T^2\right] \qquad (b.25)$$

Corrections to the initial density estimate are made by using these derivatives and the difference between the given pressure P_0 and the pressure predicted from the estimated density,

$$P = P_a + P_e + P_r$$

$$= \frac{\mathcal{R}}{\mu_a} \rho T + P_e + (1-\beta_r) \cdot P_0 \; . \qquad (b.25)$$

The first-order correction to the density by the Newton-Raphson formula is

$$\Delta_1\{\log(\rho/\mu_e)\} = -(\log P - \log P_0)/(\partial \log P/\partial \log\rho)_T \quad \text{(b.26)}$$

and the second-order correction is

$$\Delta_2\{\log(\rho/\mu_e)\} = \Delta_1 - \tfrac{1}{2}\Delta_1^2\cdot(\partial^2 \log P/\partial \log\rho^2)_T/(\partial \log P/\partial \log\rho)_T. \quad \text{(b.27)}$$

The second-order correction is applied and the process is repeated until the corrections are of the order of the numerical accuracy of the computer.

One now has a value of ρ--and also X and Y--which is consistent with the given (P,T,μ_a,μ_e). The values of P_e, $(\partial \ell n P_e/\partial \ell n T)_\rho$ and $(\partial \ell n P_e/\partial \ell n\rho)_T$ can be computed directly from the tables. Their derivatives,

$$(\partial/\partial \ell n T(P_e\cdot(\partial \ell n P_e/\partial \ell n T)_\rho))_\rho$$

$$(\partial/\partial \ell n\rho(P_e\cdot(\partial \ell n P_e/\partial \ell n T)_\rho))_T$$

$$(\partial/\partial \ell n\rho(\partial \ell n P_e/\partial \ell n\rho)_T)_T$$

can be calculated from the interpolation formulae. One can then compute the first and second derivatives of the total pressure with respect to density and temperature.

$$(\partial \ell n P/\partial \ell n T)_\rho = (P_a + P_e\cdot(\partial \ell n P_e/\partial \ell n T)_\rho)/P + 4\cdot(1-\beta_r) \quad \text{(b.28)}$$

$$(\partial \ell n P/\partial \ell n\rho)_T = (P_a + P_e\cdot(\partial \ell n P_e/\partial \ell n\rho)_T)/P \quad \text{(b.29)}$$

$$(\partial^2 \ell n P/\partial \ell n T^2)_\rho = \{P_a + (\partial/\partial \ell n T(P_e\cdot(\partial \ell n P_e/\partial \ell n T)_\rho))_\rho\}/P + 16\cdot(1-\beta_r) - (\partial \ell n P/\partial \ell n T)_\rho^2 \quad \text{(b.30)}$$

$$(\partial/\partial \ell n\rho(\partial \ell n P/\partial \ell n T)_\rho)_T = (\partial/\partial \ell n T(\partial \ell n P/\partial \ell n\rho)_T)_\rho = \{P_a + (\partial/\partial \ell n\rho(P_e\cdot(\partial \ell n P_e/\partial \ell n T)_\rho))_T\}/P - (\partial \ell n P/\partial \ell n\rho)_T\cdot(\partial \ell n P/\partial \ell n T)_\rho \quad \text{(b.31)}$$

$$(\partial^2 \ell n P/\partial \ell n\rho^2)_T = \{P_a + P_e\cdot((\partial \ell n P_e/\partial \ell n\rho)_T^2 + (\partial \ell n P_e{}^2/\partial \ell n\rho^2)_T)\}/P - (\partial \ell n P/\partial \ell n\rho)_T^2 \quad \text{(b.32)}$$

The derivatives of the density with respect to P and T can then be calculated.

$$(\partial \ell n\rho/\partial \ell nP)_T = 1/(\partial \ell nP/\partial \ell n\rho)_T \tag{b.33}$$

$$(\partial^2 \partial n\rho/\partial \ell nP^2)_T = -(\partial^2 \ell nP/\partial \ell n\rho^2)_T \cdot (\partial \ell n\rho/\partial \ell nP)_T^3 \tag{b.34}$$

$$(\partial \ell n\rho/\partial \ell nT)_P = -(\partial \ell nP/\partial \ell nT)_\rho \cdot (\partial \ell n\rho/\partial \ell nP)_T \tag{b.35}$$

$$(\partial/\partial \ell nP(\partial \ell n\rho/\partial \ell nT)_P)_T = -(\partial \ell nP/\partial \ell nT)_\rho \cdot (\partial^2 \ell n\rho/\partial \ell nP^2)_T - (\partial/\partial \ell n\rho(\partial \ell nP/\partial \ell nT)_\rho)_T \cdot (\partial \ell n\rho/\partial \ell nP)_T^2 \tag{b.36}$$

$$(\partial^2 \ell n\rho/\partial \ell nT^2)_P = -(\partial \ell nP/\partial \ell nT)_\rho \cdot (\partial/\partial \ell nP(\partial \ell n\rho/\partial \ell nT)_P)_T - (\partial \ell n\rho/\partial \ell nP)_T \cdot \{(\partial^2 \ell nP/\partial \ell nT^2)_\rho + (\partial \ell n\rho/\partial \ell nT)_P \cdot (\partial/\partial \ell n\rho(\partial \ell nP/\partial \ell nT)_\rho)_T \tag{b.37}$$

The internal energy, its derivatives, the specific heat and its derivatives can be calculated from the functional values F in tables 2 and 5 and from the previous derivatives of P, ρ and T.

$$U = U_a + U_e + U_r \tag{b.38}$$
$$= \frac{3}{2} \cdot P_a/\rho + U_e + aT^4/\rho = \frac{3}{2} \cdot \frac{\mathcal{R}}{\mu_a} \cdot T + U_e + 3(1-\beta_r) \cdot P/\rho$$

$$(\partial \ell nU/\partial \ell nT)_\rho = (U_a + U_e \cdot (\partial \ell nU_e/\partial \ell nT)_\rho + 4 \cdot U_r)/U \tag{b.39}$$

$$(\partial \ell nU/\partial \ell n\rho)_T = (P/\rho U) \cdot (1 - (\partial \ell nP/\partial \ell nT)_\rho) \tag{b.40}$$

$$(\partial \ell nU/\partial \ell nT)_P = (\partial \ell nU/\partial \ell nT)_\rho + (\partial \ell n\rho/\partial \ell nT)_P \cdot (\partial \ell nU/\partial \ell n\rho)_T \tag{b.41}$$

$$(\partial^2 \ell nU/\partial \ell nT^2)_\rho = \{U_a + (\partial/\partial \ell nT(U_e \cdot (\partial \ell nU_e/\partial \ell nT)_\rho))_\rho + 16 \cdot U_r\}/U - (\partial \ell nU/\partial \ell nT)_\rho^2 \tag{b.42}$$

$$(\partial/\partial \ell n\rho(\partial \ell nU/\partial \ell nT)_\rho)_T = (\partial/\partial \ell nT(\partial \ell nU/\partial \ell n\rho)_T)_\rho$$
$$= (\partial \ell nU/\partial \ell n\rho)_T \cdot \{(\partial \ell nP/\partial \ell nT)_\rho - (\partial \ell nU/\partial \ell nT)_\rho\}$$
$$- (P/\rho U) \cdot (\partial^2 \ell nP/\partial \ell nT^2)_\rho \qquad \text{(b.43)}$$

With the aid of equations (b.40) and (b.41) the specific heat can be expressed in terms which are more convenient for differentiation.

$$c_p = (\partial U/\partial T)_P - (P/\rho T) \cdot (\partial \ell n\rho/\partial \ell nT)_P$$
$$= (U/T) \cdot (\partial \ell nU/\partial \ell nT)_\rho$$
$$-(P/\rho T) \cdot (\partial \ell n\rho/\partial \ell nT)_P \cdot (\partial \ell nP/\partial \ell nT)_\rho \qquad \text{(b.44)}$$

$$(\partial c_p/\partial \ell nT)_P = (U/T) \cdot \Big[(\partial \ell nU/\partial \ell nT)_\rho \cdot \{(\partial \ell nU/\partial \ell nT)_P - 1\}$$
$$+ (\partial^2 \ell nU/\partial \ell nT^2)_\rho + (\partial \ell n\rho/\partial \ell nT)_P \cdot (\partial/\partial \ell n\rho(\partial \ell nU/\partial \ell nT)_\rho)_T\Big]$$
$$- (P/\rho T) \cdot \Big[(\partial \ell n\rho/\partial \ell nT)_P \cdot \{(\partial^2 \ell nP/\partial \ell nT^2)_\rho$$
$$+ (\partial \ell n\rho/\partial \ell nT)_P \cdot (\partial/\partial \ell n\rho\{\partial \ell nP/\partial \ell nT)_\rho)_T\}$$
$$+ (\partial \ell nP/\partial \ell nT)_\rho \cdot \{(\partial/\partial \ell nT(\partial \ell n\rho/\partial \ell nT)_P)_P$$
$$+ (\partial \ell n\rho/\partial \ell nT)_P \cdot (-1 - (\partial \ell n\rho/\partial \ell nT)_P)\}\Big] \qquad \text{(b.45)}$$

$$(\partial c_p/\partial \ell nP)_T = (U/T) \cdot (\partial \ell n\rho/\partial \ell nP)_T \cdot \Big[(\partial/\partial \ell n\rho(\partial \ell nU/\partial \ell nT)_\rho)_T$$
$$+ (\partial \ell nU/\partial \ell nT)_\rho \cdot (\partial \ell nU/\partial \ell n\rho)_T\Big]$$
$$- (P/\rho T) \cdot \Big[(\partial \ell nP/\partial \ell nT)_\rho \cdot \{(\partial/\partial \ell nP(\partial \ell n\rho/\partial \ell nT)_P)_T$$
$$+ (\partial \ell n\rho/\partial \ell nT)_P \cdot (1 - (\partial \ell n\rho/\partial \ell nP)_T\}$$
$$+ (\partial \ell n\rho/\partial \ell nT)_P \cdot (\partial \ell n\rho/\partial \ell nP)_T \cdot (\partial/\partial \ell n\rho(\partial \ell nP/\partial \ell nT)_\rho)_T\Big]$$
$$\text{(b.46)}$$

All of the above quantities on the right-hand side have been derived previously. The values of U_e and $U_e \cdot (\partial \ell nU_e/\partial \ell nT)_\rho$ are taken directly from the tables; the second-order derivative of U_e is calculated from the interpolation method. The adiabatic gradient and its derivatives are the same as in §4.a.

Since the solution of the Saha equations in §4.a allows for only single ionization of the metals, it will not agree with the general equation of state which assumes full ionization of all metals. Thus, it is necessary to choose a regime in which the Saha quantities are merged smoothly with those of the general equation of state. Since the ionization is mainly a function of temperature, I have chosen a temperature region where the helium is fully ionized in most cases to interpolate between the two equations of state. One selects two parameters such that

$$\log T < (\log T_0 - \Delta\log T) \rightarrow \text{Saha only}$$

and $$\log T > (\log T_0) \rightarrow \text{general equation of state only.}$$

In the intermediate region one defines

$$x \equiv (\log T_0 - \log T)/\Delta\log T \ , \qquad \text{(b.47)}$$

where x = 1 in the limit of Saha only, and x = 0 in the limit of no Saha. All of the interpolated quantities should be smooth in this region, and thus, I have selected the lowest order polynomial f(x) such that

$$\begin{aligned} &f(0) = 0 \quad \text{and} \quad f(1) = 1 \\ &f'(0) = f'(1) = 0 \\ &f''(0) = f''(1) = 0 \end{aligned} \qquad \text{(b.48)}$$

which gives

$$f(x) = x^3(6x^2 - 15x + 10) = 1 - f(1-x) \qquad \text{(b.49)}$$

$$f'(x) = 30x^2(1 - x)^2$$

$$f''(x) = 60x(2x^2 - 3x + 1) \ .$$

The interpolation proceeds as follows where subscript $_0$ refers to Saha values and subscript $_1$ refers to general equation of state values.

$$\log \rho = \log \rho_1 + f\cdot(\log \rho_0 - \log \rho_1) \qquad \text{(b.50)}$$

$$(\partial \ell n\rho/\partial \ell nT)_P \equiv \partial^T \qquad \text{(b.51)}$$
$$= \partial_1^T + f\cdot(\partial_0^T - \partial_1^T) - (\log\rho_0 - \log\rho_1)\cdot f'/(\Delta \log T)$$

$$(\partial \ell n\rho/\partial \ell nP)_T \equiv \partial^P \qquad \text{(b.52)}$$
$$= \partial_1^P + f\cdot(\partial_0^P - \partial_1^P)$$

$$(\partial/\partial \ell nT(\partial \ell n\rho/\partial \ell nT)_P)_P \equiv \partial\partial^T \qquad \text{(b.53)}$$
$$= \partial\partial_1^T + f\cdot(\partial\partial_0^T - \partial\partial_1^T) - 2\cdot(\partial_0^T - \partial_1^T)\cdot f'/(\ell n10\cdot\Delta \log T)$$
$$+ (\log\rho_0 - \log\rho_1)\cdot f''/\{\ell n10\cdot(\Delta \log T)^2\}$$

$$(\partial/\partial \ell nP(\partial \ell n\rho/\partial \ell nT)_P)_T \equiv \partial\partial^P \qquad \text{(b.54)}$$
$$= \partial\partial_1^P + f\cdot(\partial\partial_0^P - \partial\partial_1^P) - (\partial_0^P - \partial_1^P)\cdot f'/(\ell n10\cdot\Delta \log T)$$

The adiabatic gradient and the specific heat are treated alike.

$$\nabla_{ad} = \nabla_{ad_1} + f\cdot(\nabla_{ad_0} - \nabla_{ad_1}) \qquad \text{(b.55)}$$

$$(\partial\nabla_{ad}/\partial \ell nT)_P \equiv \partial_{ad}^T \qquad \text{(b.56)}$$
$$= \partial_{ad_1}^T + f\cdot(\partial_{ad_0}^T - \partial_{ad_1}^T)$$
$$- (\nabla_{ad_0} - \nabla_{ad_1})\cdot f'/(\ell n10\cdot\Delta \log T)$$

$$(\partial\nabla_{ad}/\partial \ell nP)_T \equiv \partial_{ad}^P \qquad \text{(b.57)}$$
$$= \partial_{ad_1}^P + f\cdot(\partial_{ad_0}^P - \partial_{ad_1}^P)$$

c) Opacities

The code utilizes five opacity tables. The first two tables are for compositions $(X,Z) = (X_0,Z_0)$ and $(X,Z) = (0,Z_0)$ where X_0 and Z_0 are the initial hydrogen and metal abundances of the homogeneous main sequence model. These radiative

opacities are the Rosseland-mean opacities of Cox and Stewart (1970). Where the value of X_0 is not tabulated, a fourth-order Lagrangian interpolation of κ vs. X is used with the five tables given by Cox and Stewart to compute $\kappa(X_0,Z_0)$. The third opacity table is the radiative opacity for (X,Z) = (0,1) (Iben Mix XX, Cox and Stewart 1970). The last two tables are conductive opacities for (X,Z) = (1,0) and (X,Z) = (0,0). The values of the conductive opacities for $\log \rho \leq 6$ are taken from Hubbard and Lampe (1969) and for $\log \rho > 6$, from Canuto (1970). All of the tables are in the standard form used by Cox and Stewart (1970) with 8 density entries at each of 29 temperature entries. The tabulated values of the last two tables are from Sweigart (1974).

From a given table of $\log \kappa$ vs. ($\log \rho$, $\log T$), the value of the opacity κ and its derivatives are calculated as follows. Locate the "box" which contains ($\log \rho$, $\log T$),

$$\log \rho_1 \leq \log \rho < \log \rho_2$$
$$\log T_1 \leq \log T < \log T_2, \qquad \text{(c.1)}$$

and define

$$\Delta_1 \equiv \log \kappa(\rho_2,T_1) - \log \kappa(\rho_1,T_1)$$
$$\Delta_2 \equiv \log \kappa(\rho_2,T_2) - \log \kappa(\rho_1,T_2) , \qquad \text{(c.2)}$$

which are the density derivatives $(\partial \ell n\kappa/\partial \ell n\rho)_T$ at T_1 and T_2 since $(\log \rho_{i+1} - \log \rho_i) = 1$ for all table entries. Then define

$$\log \kappa_1 \equiv \log \kappa(\rho_1,T_1) + \Delta_1 \cdot (\log \rho - \log \rho_1)$$
$$\log \kappa_2 \equiv \log \kappa(\rho_1,T_2) + \Delta_2 \cdot (\log \rho - \log \rho_1). \qquad \text{(c.3)}$$

The derivatives of the opacity and the value of the opacity can then be interpolated.

$$(\partial \ell n\kappa/\partial \ell n\rho)_T = \Delta_1 + (\Delta_2-\Delta_1)\cdot(\log T - \log T_1)/(\log T_2 - \log T_1) \quad (c.4)$$

$$(\partial \ell n\kappa/\partial \ell nT)_\rho = (\log\kappa_2 - \log\kappa_1)/(\log T_2 - \log T_1) \quad (c.5)$$

$$\log \kappa = \log \kappa_1 + (\partial \ell n\kappa/\partial \ell nT)_\rho \cdot (\log T - \log T_1) \quad (c.6)$$

For the calculation of the radiative opacity a combination of the first two tables or the second and third tables is often needed. In the case of $0 < X < X_0$ and $Z = Z_0$, the value of κ (not $\log \kappa$) is interpolated linearly in X.

$$\kappa(X,Z_0) = (X/X_0)\cdot\kappa(X_0,Z_0) + (1 - X/X_0)\cdot\kappa(0,Z_0) \quad (c.7)$$

The values of the derivatives follow from the method of interpolation,

$$(\partial \ell n\kappa/\partial \ell nq) = \{(X/X_0)\cdot\kappa(X_0)\cdot(\partial \ell n\kappa/\partial \ell nq)_{X_0} + (1 - X/X_0)\cdot\kappa(0)\cdot(\partial \ell n\kappa/\partial \ell nq)_0\}/\kappa(X) \quad (c.8)$$

where q = ρ or T. Likewise, the opacity for $Z_0 < Z < 1$ (assuming X = 0) is interpolated between $\kappa(0,Z_0)$ and $\kappa(0,1)$ with a weighting factor $(1-Z)/(1-Z_0)$.

The value of the conductive opacity is calculated by interpolating linearly in X and then scaling linearly with Z.

$$\kappa_c(X,Z) = (1+Z)\cdot(X\cdot\kappa_c(1,0) + (1-X)\cdot\kappa_c(0,0)) \quad (c.9)$$

The derivatives of κ_c are computed as in equation (c.8) with $X_0 = 1$ and are unaffected by the (1+Z) scaling.

The true opacity is the inverse mean of the radiative opacity κ_r and the conductive opacity κ_c.

$$\frac{1}{\kappa} = \frac{1}{\kappa_r} + \frac{1}{\kappa_c} \rightarrow \kappa = \kappa_r\cdot\kappa_c/(\kappa_r + \kappa_c) \quad (c.10)$$

The derivatives then become,

$$(\partial \ell n \kappa / \partial \ell n q) = \kappa \cdot \{(\partial \ell n \kappa_c / \partial \ell n q)/\kappa_r + (\partial \ell n \kappa_r / \partial \ell n q)/\kappa_c\} \quad \text{(c.11)}$$

where again q = ρ or T.

In the code the calculation of the conductive opacity is turned on when the reduction routine starts calculating the local physics from the interior of the star outward. This calculation of the conductive opacity is switched off by the opacity routine when the value of κ_c/κ_r exceeds a set value ($\simeq 10^4$) and stays switched off until the reduction routine starts at the center of the model again. The conductive opacity is also ignored in the envelope integrations.

d) The Convective Gradient--Mixing Length Theory

The calculation of the convective temperature gradient ∇_c in the envelope of the stellar models employs the mixing length theory (Henyey, Vardya and Bodenheimer 1965, Kippenhahn 1967, Paczynski 1969). There are three free parameters in this theory which are set as follows for my computations.

$$\alpha_1 = \ell/H \equiv 1 \qquad \ell = \text{mixing length}, \; H = \text{pressure scale height} \quad \text{(d.1)}$$

$$\alpha_2 = 1/3 \quad \text{(d.2)}$$

$$\alpha_3 = 16\sqrt{2}\cdot\sigma \quad \text{(d.3)}$$

The latter two parameters have the same values as in Paczynski (1969).

Defining $\delta \equiv \nabla_r - \nabla_{ad}$, the Schwarzschild (1906) criterion is used to determine convection: $\delta > 0 \rightarrow$ convective. In the deep interior convection zones ∇_c is set equal to the adiabatic gradient ∇_{ad}.

In the envelope the evaluation of ∇_c is more complex, and one begins by defining,

$$g \equiv Gm/R^2 \quad (m = \text{mass interior to } R) \tag{d.4}$$

$$H \equiv P/\rho g \tag{d.5}$$

$$\omega \equiv \rho\kappa\ell = \alpha_1 \rho\kappa H = \alpha_1 \kappa P/g \tag{d.6}$$

$$\phi \equiv (1 + \alpha_2\omega^2)^{-1} \tag{d.7}$$

$$a_1 \equiv \alpha_3 \cdot \phi \cdot \frac{\kappa T^3}{c_p}\{-H/g\delta(\partial \ell n\rho/\partial \ell nT)_p\}^{\frac{1}{2}} \tag{d.8}$$

$$a_3 \equiv \frac{3}{4}\phi\omega^2/a_1 \quad . \tag{d.9}$$

The equation $F(x) = a_3x^3 + x^2 + a_1x - 1$ is then solved for $y > 0$ such that $F(y) = 0$. The root y is guaranteed to lie in the interval $(0,+1)$ since $F(0) = -1 < 0$ and $F(1) = a_1 + a_3 > 0$. Further, this root y is unique since the derivative of F, $F'(x) = 3a_3x^2 + 2x + a_1$, is positive definite for $x > 0$. An initial estimate of the root y is made and a second-order Newton-Raphson correction is applied.

$$\Delta y = -(F(y)/F'(y)) - \tfrac{1}{2}(F(y)/F'(y))^2 \cdot F''(y)/F'(y) \tag{d.10}$$

The initial estimate of y is $y = 1/a_1$, unless $a_3 > 10^3$ in which case $y = (1/a_3)^{1/3}$ which follows the asymptotic behavior of the solution in either limit. Given the solution y, the convective gradient is computed.

$$\nabla_c = \nabla_{ad} + (\nabla_r - \nabla_{ad}) \cdot y \cdot (y + a_1) \tag{d.11}$$

The linearization of the convective gradient is cumbersome but can be calculated. I shall consider derivatives with respect to $\ell n\ P$, ℓnT and ℓnR, ignoring the luminosity derivative.

$$(\partial\nabla_c/\partial\ell nx) = (\partial\nabla_{ad}/\partial\ell nx) + y(y+a_1)\cdot(\partial\delta/\partial\ell nx) \quad (d.12)$$
$$+ \delta\cdot\{(2y+a_1)\cdot(\partial y/\partial\ell nx) + a_1 y\cdot(\partial\ell na_1/\partial\ell nx)\}$$

where

$$(\partial\delta/\partial\ell nx) = (\partial(\nabla_r-\nabla_{ad})/\partial\ell nx) \quad (d.13)$$
$$= (\partial\nabla_r/\partial\ell nx) - (\partial\nabla_{ad}/\partial\ell nx).$$

The derivatives of ∇_{ad} come from the equation of state,

$$(\partial\nabla_{ad}/\partial\ell nx) = \nabla_{ad}\cdot(\partial\ell n\nabla_{ad}/\partial\ell nx) \quad (d.14)$$

and are non-vanishing only for x = P or T. The derivatives of

$$\nabla_r = (3/16\pi ac)\cdot(\kappa LP)/(GmT^4) \quad (d.15)$$

are also non-vanishing only for x = P or T.

$$(\partial\nabla_r/\partial\ell nT) = \nabla_r\cdot\{-4 + (\partial\ell n\kappa/\partial\ell nT)_P\} \quad (d.16)$$

$$(\partial\nabla_r/\partial\ell nP) = \nabla_r\cdot\{+1 + (\partial\ell n\kappa/\partial\ell nP)_T\} \quad (d.17)$$

The derivatives of y are functions of a_1 and a_3.

$$(\partial y/\partial\ell nx) = -\{a_1 y\cdot(\partial\ell na_1/\partial\ell nx) + a_3 y^3\cdot(\partial\ell na_3/\partial\ell nx)\}$$
$$/(3a_3y^2 + 2y + a_1) \quad (d.18)$$

The equation (d.12) for the derivatives of ∇_c now becomes

$$(\partial\nabla_c/\partial\ell nx) = (\partial\nabla_{ad}/\partial\ell nx) + y(y+a_1)\cdot(\partial\delta/\partial\ell nx) \quad (d.19)$$
$$+ a_3y^3\delta\cdot\{3a_1\cdot(\partial\ell na_1/\partial\ell nx) - (2y+a_1)\cdot(\partial\ell na_3/\partial\ell nx)\}$$
$$/(3a_3y^2 + 2y + a_1) \quad ,$$

where the only remaining unknown quantities are the derivatives of a_1 and a_3.

$$(\partial\ell na_1/\partial\ell nx) = (\partial\ell n\phi/\partial\ell nx) + (\partial\ell n\kappa/\partial\ell nx) \quad (d.20)$$
$$+ 3\cdot(\partial\ell nT/\partial\ell nx) - (\partial\ell nc_p/\partial\ell nx) + \tfrac{1}{2}\cdot(\partial\ell nH/\partial\ell nx)$$
$$- \tfrac{1}{2}\cdot(\partial\delta/\partial\ell nx)/\delta - \tfrac{1}{2}\cdot(\partial\ell ng/\partial\ell nx)$$
$$- \tfrac{1}{2}\cdot(\partial/\partial\ell nx(\partial\ell n\rho/\partial\ell nT)_P)/(\partial\ell n\rho/\partial\ell nT)_P$$

$$(\partial \ell n a_3/\partial \ell n x) = 2\cdot(\partial \ell n \omega/\partial \ell n x) + (\partial \ell n \phi/\partial \ell n x) - (\partial \ell n a_1/\partial \ell n x) \quad (d.21)$$

The value of $(\partial \delta/\partial \ell n x)$ has been previously calculated and the derivative of $q \equiv (\partial \ell n \rho/\partial \ell n T)_P$ and c_p are computed by the equation of state. By calculating the derivative of ϕ,

$$(\partial \ell n \phi/\partial \ell n x) = -2\alpha_2 \omega^2 \phi\cdot(\partial \ell n \omega/\partial \ell n x), \quad (d.22)$$

and by expressing H and g explicitly, one can gather the terms of equations (d.20-21) to produce,

$$(\partial \ell n a_1/\partial \ell n x) = -2\alpha_2 \omega^2 \phi\cdot(\partial \ell n \omega/\partial \ell n x) - (\partial \ell n c_p/\partial \ell n x) - \tfrac{1}{2}\cdot(\partial \delta/\partial \ell n x)/\delta - \tfrac{1}{2}\cdot(\partial q/\partial \ell n x)/q + \tfrac{1}{2}\cdot(\partial \ell n P/\partial \ell n x) + 3\cdot(\partial \ell n T/\partial \ell n x) + 2\cdot(\partial \ell n R/\partial \ell n x) + (\partial \ell n \kappa/\partial \ell n x) - \tfrac{1}{2}\cdot(\partial \ell n \rho/\partial \ell n x) \quad (d.23)$$

$$(\partial \ell n a_3/\partial \ell n x) = 2\phi\cdot(\partial \ell n \omega/\partial \ell n x) - (\partial \ell n a_1/\partial \ell n x) . \quad (d.24)$$

The derivatives of ω with respect to P, T and R are straightforward.

$$(\partial \ell n \omega/\partial \ell n P) = 1 + (\partial \ell n \kappa/\partial \ell n P)_T \quad (d.25)$$

$$(\partial \ell n \omega/\partial \ell n T) = (\partial \ell n \kappa/\partial \ell n T)_P \quad (d.26)$$

$$(\partial \ell n \omega/\partial \ell n R) = 2 \quad (d.27)$$

e) Energy Generation

The calculation of the energy generation includes the individual rates for the PP-chain (PPI, PPII, PPIII), the CNO-cycle with a simplified NO approach to equilibrium, the triple-alpha process and neutrino losses. The values of intermediate or strong screening are applied to the above energy producing reactions with the exception of the neutrinos.

The coefficients of all of the reaction rates and the formulae for most of them are taken from Fowler, Caughlan and Zimmerman (1975).

The reaction rate for the PP-chain is actually that for the $H^1(p,e^+\nu)D^2$ reaction and assumes that all the other reactions in the chain are relatively instantaneous. The burning rate is then

$$(dX/dt)_{pp} = 4.181\cdot10^{-15}\rho X^2 T_9^{-2/3} f_s \cdot \exp\{-3.380/T_9^{1/3}\} \cdot\phi(\alpha)\cdot(1.0 + 0.123\cdot T_9^{1/3} + 1.09\cdot T_9^{2/3} + 0.938\cdot T_9) \quad \text{sec}^{-1} \qquad \text{(e.1)}$$

where $T_9 = T/10^9{}^0K$, f_s is the screening factor and $\phi(\alpha)$ increases monotonically from $1 \rightarrow 2$ as α increases from $0 \rightarrow \infty$. The above rate is the instantaneous rate of decrease in X (hydrogen abundance by weight) which is also the rate of increase in Y (helium abundance by weight). The function represents the efficiency of the conversion of D^2 into He^4, i.e., $\phi = 1$ for PPI and $\phi = 2$ for PPII-PPIII. The derivation of the different PP-chain energies follows that of Clayton (1968). The division between PPI and PPII-PPIII is determined by

$$\alpha \equiv (S_{34}^2/S_{11}S_{33})\cdot(Y/4X)^2\cdot\exp\{-10.0/T_9^{1/3}\} \qquad \text{(e.2)}$$
$$= 1.93\cdot10^{17}\cdot(Y/4X)^2\cdot\exp\{-10.0/T_9^{1/3}\}$$

where S_{11}, S_{33} and S_{34} are the cross-sections for (pp), (He^3He^3) and (He^3He^4), respectively. The value of ϕ is then

$$\phi(\alpha) \equiv 1 + \alpha\cdot\{(1 + 2/\alpha)^{\frac{1}{2}} - 1\}. \qquad \text{(e.3)}$$

The breakdown between PPII and PPIII is determined by the ratio of Be^7proton capture to Be^7 electron capture.

$$\Gamma \equiv \{Be^7(p,\gamma)B^8\}/\{Be^7(e,\nu\gamma)Li^7\} \qquad (e.4)$$
$$= 10^{15.6837}\cdot X/(1+X)\cdot T_9^{-1/6}\cdot\exp\{-10.262/T_9^{1/3}\}$$

By defining the fraction of reactions due to each chain,

$$f_I = ((1 + 2/\alpha)^{\frac{1}{2}} - 1)/((1 + 2/\alpha)^{\frac{1}{2}} + 3) \qquad (e.5)$$

$$f_{II} = (1 - f_I)/(1 + \Gamma) \qquad (e.6)$$

$$f_{III} = 1 - f_I - f_{II} \ , \qquad (e.7)$$

the total energy of the PP-chain (subtracting the energy of the neutrinos which are produced) is then,

$$\varepsilon_{pp} = 6.398\cdot 10^{18}\cdot\psi\cdot(dX/dt)_{pp} \ \text{ erg/gm/sec} \qquad (e.8)$$

where

$$\psi = 0.979\cdot f_I + 0.960\cdot f_{II} + 0.721\cdot f_{III} \ . \qquad (e.9)$$

In the definitions of α and Γ, the cross-sections of Bahcall and Sears (1972) are used.

The derivatives of ε_{pp} can be found directly.

$$(\partial\varepsilon_{pp}/\partial\ell n\rho)_T = \varepsilon_{pp}\cdot\{1 + (\partial\ell nf_S/\partial\ell n\rho)_T\} \qquad (e.10)$$

$$(\partial\varepsilon_{pp}/\partial\ell nT)_\rho = \varepsilon_{pp}\cdot\{-2/3 + 1.1267/T_9^{1/3} \qquad (e.11)$$
$$+ (\partial\ell nf_S/\partial\ell nT)_\rho + (\partial\ell n\phi/\partial\ell nT)_\rho + (\partial\ell n\psi/\partial\ell nT)_\rho$$
$$+ (0.041\cdot T_9^{1/3} + 0.727\cdot T_9^{2/3} + 0.938\cdot T_9)$$
$$/(1.0 + 0.123\cdot T_9^{1/3} + 1.09\cdot T_9^{2/3} + 0.938\cdot T_9)\}$$

$$(\partial\ell n\phi/\partial\ell nT) = (2/\phi - 1)\cdot(1 + 2/\alpha)^{-\frac{1}{2}}\cdot 3.333/T_9^{1/3} \qquad (e.12)$$

$$(\partial\ell n\psi/\partial\ell nT) = \psi^{-1}\cdot\{(0.258 - 0.239/(1+\Gamma))\cdot(\partial f_I/\partial\ell nT)$$
$$- 0.239\cdot f_{III}/(1+\Gamma)\cdot(\partial\ell n\Gamma/\partial\ell nT)\} \qquad (e.13)$$

$$(\partial\ell n\Gamma/\partial\ell nT) = -1/6 + 3.4207/T_9^{1/3} \qquad (e.14)$$

$$(\partial f_I/\partial\ell nT) = -4\cdot\{\alpha\cdot(1 + 2/\alpha)^{\frac{1}{2}}\cdot((1 + 2/\alpha)^{\frac{1}{2}} + 3)^2\}^{-1}$$
$$\cdot 3.333/T_9^{1/3} \qquad (e.15)$$

The screening factor f_s and its derivatives are described later in this section.

In the calculation of the CNO bi-cycle, CN equilibrium is assumed and the CN cycle is assumed to be the only source of energy. The hydrogen burning rate due to the CN cycle is then

$$(dX/dt)_{CN} = 1.202 \cdot 10^{7} \rho X X_N T_9^{-2/3} f_s \cdot \exp\{-15.228/T_9^{1/3}\} \quad \text{sec}^{-1} \qquad \text{(e.16)}$$

and the energy produced is

$$\varepsilon_{CN} = 5.977 \cdot 10^{18} \cdot (dX/dt)_{CN} \quad \text{erg/gm/sec} . \qquad \text{(e.17)}$$

The value of X_N (N^{14} abundance by weight) assumes that all the carbon and nitrogen is in the form of N^{14},

$$X_N = Z - Z_m - X_O, \qquad \text{(e.18)}$$

where Z is the total metal abundance by weight, Z_m is the weight abundance of all non-CNO metals, and X_O is the weight abundance of O^{16}. The approach to NO equilibrium is taken as a simple burning rate of O^{16} assuming O^{17} equilibrium.

$$(dX_O/dt) = 9.54 \cdot 10^{7} \rho X X_O T_9^{-17/21} f_s \cdot \exp\{-16.693/T_9^{1/3}\} - 1.6 \cdot 10^{-3} \cdot (dX/dt)_{CN} \quad \text{sec}^{-1} \qquad \text{(e.19)}$$

Between successive models the value of X_O is decreased at a rate of (dX_O/dt) per second, and thus the value of X_N is correspondingly increased. The derivatives of the CN energy production are easily calculated.

$$(\partial \varepsilon_{CN}/\partial \ell n \rho)_T = \varepsilon_{CN} \cdot \{1 + (\partial \ell n f_s/\partial \ell n \rho)_T\} \qquad \text{(e.20)}$$

$$(\partial \varepsilon_{CN}/\partial \ell n T)_\rho = \varepsilon_{CN} \cdot \{-2/3 + 5.076/T_9^{1/3} + (\partial \ell n f_s/\partial \ell n T)_\rho\} \qquad \text{(e.21)}$$

The helium burning rate is assumed to be solely due to the triple-alpha process.

$$(dY/dt)_{3\alpha} = 8.094\cdot10^{-10}\rho^2 Y^3 T_9^{-3} f_s \cdot \exp\{-4.4109/T_9\} \text{ sec}^{-1} \quad \text{(e.22)}$$

$$\varepsilon_{3\alpha} = 5.849\cdot10^{17}\cdot(dY/dt)_{3\alpha} \text{ erg/gm/sec} \quad \text{(e.23)}$$

$$(\partial\varepsilon_{3\alpha}/\partial \ell n\rho)_T = \varepsilon_{3\alpha}\cdot\{2 + (\partial \ell n f_s/\partial \ell n\rho)_T\} \quad \text{(e.24)}$$

$$(\partial\varepsilon_{3\alpha}/\partial \ell nT)_\rho = \varepsilon_{3\alpha}\cdot\{-3 + 4.4109/T_9 + (\partial \ell n f_s/\partial \ell nT)_\rho\} \quad \text{(e.25)}$$

The neutrino losses are calculated from the analytic form given by Beaudet, Petrosian and Salpeter (1967). These losses are computed as a negative energy in the energy generation subroutine,

$$\varepsilon_\nu = -(\varepsilon_1 + \varepsilon_2 + \varepsilon_3), \quad \text{(e.26)}$$

where the subscripts $_1$, $_2$ and $_3$ refer to pair, photo and plasma neutrinos, respectively. By defining

$$\lambda \equiv kT/m_e c^2 = T_9/5.9302 \quad \text{(e.27)}$$

$$\xi \equiv 10^{-3}(\rho/\mu_e)^{1/3}/\lambda \quad \text{(e.28)}$$

$$f(\lambda,\xi) \equiv \exp\{-c\xi\}\cdot p(\xi)/q(\lambda,\xi) \quad \text{(e.29)}$$

$$= \exp\{-c\xi\}\cdot(a_0 + a_1\xi + a_2\xi^2) /(\xi^3 + b_1\lambda^{-1} + b_2\lambda^{-2} + b_3\lambda^{-3}) ,$$

one can calculate the neutrino losses,

$$\varepsilon_1 = g(\lambda)\cdot f_1(\lambda,\xi)\cdot\exp\{-2/\lambda\} \quad \text{(e.30)}$$

$$\varepsilon_2 = \lambda^5/\mu_e\cdot f_2(\lambda,\xi) \quad \text{(e.31)}$$

$$\varepsilon_3 = \rho^2/\mu_e\cdot f_3(\lambda,\xi) , \quad \text{(e.32)}$$

where the function $g(\lambda)$ is defined as

$$g(\lambda) \equiv 1.0 - 13.04\cdot\lambda^2 + 133.5\cdot\lambda^4 + 1534.\cdot\lambda^6 + 918.6\cdot\lambda^8 . \quad \text{(e.33)}$$

The mean weight per electron μ_e is computed as

$$1/\mu_e = \tfrac{1}{2}(1 + X) \quad \text{and} \quad (1/\mu_e)^{1/3} = 0.7937 + 0.2063 \cdot X \tag{e.34}$$

which is correct in either limit X = 0 or X = 1. The following table lists the coefficients for the f functions.

	a_0	a_1	a_2
1(pair)	6.002E19	2.084E20	1.872E21
2(photo)	4.886E10	7.580E10	6.023E10
3(plasma)	2.320E-7	8.449E-8	1.787E-8

	b_1	b_2	b_3	c
1	9.383E-1	-4.141E-1	5.829E-2	5.5924
2	6.290E-3	7.483E-3	3.061E-4	1.5654
3	2.581E-2	1.734E-2	6.990E-4	0.56457

The derivatives of the neutrino rates can be calculated as follows.

$$(\partial \ell nf/\partial \ell nT)_\rho = -(a_1\xi + 2a_2\xi^2)/p(\xi) + c\xi + (b_1\lambda^{-1} + 2b_2\lambda^{-2} + 3b_3\lambda^{-3} + 3\xi^3)/q(\lambda,\xi) \tag{e.35}$$

$$(\partial \ell nf/\partial \ell n\rho)_T = \tfrac{1}{3}\cdot\{(a_1\xi + 2a_2\xi^2)/p(\xi) - c\xi - 3\xi^3/q(\lambda,\xi)\} \tag{e.36}$$

PAIR:
$$(\partial \varepsilon_1/\partial \ell nT)_\rho = \varepsilon_1\cdot\{2/\lambda + (\partial \ell nf_1/\partial \ell nT)_\rho + (\partial \ell ng/\partial \ell nT)\} \tag{e.37}$$

$$(\partial \varepsilon_1/\partial \ell n\rho)_T = \varepsilon_1\cdot\{-1 + (\partial \ell nf_1/\partial \ell n\rho)_T\} \tag{e.38}$$

PHOTO:
$$(\partial \varepsilon_2/\partial \ell nT)_\rho = \varepsilon_2\cdot\{5 + (\partial \ell nf_2/\partial \ell nT)_\rho\} \tag{e.39}$$

$$(\partial \varepsilon_2/\partial \ell n\rho)_T = \varepsilon_2\cdot(\partial \ell nf_2/\partial \ell n\rho)_T \tag{e.40}$$

PLASMA:
$$(\partial \varepsilon_3/\partial \ell nT)_\rho = \varepsilon_3\cdot(\partial \ell nf_3/\partial \ell nT)_\rho \tag{e.41}$$

$$(\partial \varepsilon_3/\partial \ell n\rho)_T = \varepsilon_3\cdot\{2 + (\partial \ell nf_3/\partial \ell n\rho)_T\} \tag{e.42}$$

$$(\partial \ell ng/\partial \ell nT) = (-26.08\cdot\lambda^2 + 534.\cdot\lambda^4 + 9204.\cdot\lambda^6 + 7348.8\cdot\lambda^8)/g(\lambda) \tag{e.43}$$

The calculation of the increase in energy generation due to electron screening is difficult, and thus, most workers have tended to use the weak screening approximation. The weak screening factor is $f_s = \exp(H)$ where in the limit,

$$H = Z_1 \cdot Z_2 \cdot \tilde{z} \cdot \Lambda_0 \qquad \text{(e.44)}$$

$Z_1, Z_2 \equiv$ charge of the two interacting nuclei

$\tilde{z} \equiv$ r.m.s. average of the number of electrons per nucleide, including electron degeneracy factor

$$\Lambda_0 \equiv 1.88 \cdot 10^8 \cdot (\rho/\mu_a T^3)^{\frac{1}{2}}$$

The basic problem with the weak screening approximation is that it is only valid for $H \ll 1$ and hence where the screening is unimportant.

I have adopted the formulae of DeWitt, Graboske and Cooper (1973) and Graboske, DeWitt and Grossman (1973) for both intermediate and strong screening. For intermediate screening one has

$$H_i = \alpha \cdot (Z_1 \cdot Z_2 \cdot \tilde{z} \cdot \Lambda_0)^{0.860}, \qquad \text{(e.45)}$$

where α is a function of $(Z_1 Z_2/\tilde{z}^2)$. For strong screening one has

$$H_s = 0.624 \cdot \bar{z}^{1/3} \cdot \Lambda_0^{2/3} \cdot \{f_1(Z_1,Z_2) + 0.316 \cdot \bar{z}^{1/3} \cdot f_2(Z_1,Z_2) + 0.460 \cdot \bar{z}^{-2/3} \cdot f_3(Z_1,Z_2), \qquad \text{(e.46)}$$

where $\bar{z}$ is the mean number of electrons per nucleide and

$$f_1(Z_1,Z_2) = (Z_1 + Z_2)^{5/3} - Z_1^{5/3} - Z_2^{5/3} \qquad \text{(e.47)}$$

$$f_2(Z_1,Z_2) = (Z_1 + Z_2)^{4/3} - Z_1^{4/3} - Z_2^{4/3} \qquad \text{(e.48)}$$

$$f_3(Z_1,Z_2) = (Z_1 + Z_2)^{2/3} - Z_1^{2/3} - Z_2^{2/3} . \qquad \text{(e.49)}$$

As can be seen from the formulation of H_i and H_s, the screening factors depend on composition in addition to density and temperature. For my calculations I have fixed the

composition for any given reaction and thus, also fixed the values of μ_a, $\bar{z}$ and $\tilde{z}$ (degeneracy is also ignored in the screening). Thus, for a given reaction and composition the screening factors can be calculated from

$$F_0 \equiv 1.88 \cdot 10^8 \cdot (\rho/T^3)^{\frac{1}{2}} , \qquad (e.50)$$

and are given in the following table.

Reaction	Composition X	Composition Y	H_i	H_s
pp	0.72	0.28	$0.606 \cdot F_0^{0.860}$	$0.798 \cdot F_0^{2/3} - 0.179$
pN	1	0	$3.572 \cdot F_0^{0.860}$	$3.678 \cdot F_0^{2/3} - 0.303$
αα	0	1	$2.039 \cdot F_0^{0.860}$	$2.052 \cdot F_0^{2/3} - 0.190$
αBe	0	1	$3.845 \cdot F_0^{0.860}$	$3.648 \cdot F_0^{2/3} - 0.233$
3α	0	1	$5.884 \cdot F_0^{0.860}$	$5.700 \cdot F_0^{2/3} - 0.423$

The screening for the triple-alpha reaction is the sum of the screenings for (αα) and (αBe). The cross-over point between intermediate and strong screening ($H_i(F_0') = H_s(F_0')$) for the three basic reactions is given below.

Reaction	F_0'	log F_0'	$H_i(F_0')=H_s(F_0')$
pp	0.6276	-0.2023	0.4060
pN	0.6281	-0.2020	2.3945
3α	0.3927	-0.4059	2.6337

Since weak screening is ignored, the intermediate screening is extended into the weak limit where the screening is negligible. The derivatives of the screening factor $f_s = \exp(H)$ can be easily calculated for either type of screening if one expresses H as

$$H = a \cdot F_0^b - c \ , \qquad \text{(e.51)}$$

where b = 2/3 for strong screening and b = 0.860 and c = 0 for intermediate screening.

$$(\partial \ell n f_s / \partial \ell n T)_\rho = -\tfrac{3}{2} \cdot b \cdot (H + c) \qquad \text{(e.52)}$$

$$(\partial \ell n f_s / \partial \ell n \rho)_T = +\tfrac{1}{2} \cdot b \cdot (H + c) \qquad \text{(e.53)}$$

Because the derivatives of the intermediate and strong screening agree to within 10% at the cross-over point, a direct switch between the two forms--rather than an interpolation formula--is used at the cross-over point.

The energy generation routine computes the following quantities given the temperature, density and composition:

1) total energy generation ε

$$\varepsilon = \varepsilon_{PP} + \varepsilon_{CN} + \varepsilon_{3\alpha} + \varepsilon_\nu \quad \text{erg/gm/s} \quad (\varepsilon_\nu < 0),$$

2) natural logarithm derivatives of ε

$$(\partial \varepsilon / \partial \ell n T)_\rho = (\partial \varepsilon_{PP} / \partial \ell n T)_\rho + (\partial \varepsilon_{CN} / \partial \ell n T)_\rho + (\partial \varepsilon_{3\alpha} / \partial \ell n T)_\rho + (\partial \varepsilon_\nu / \partial \ell n T)_\rho$$

$$(\partial \varepsilon / \partial \ell n \rho)_T = (\partial \varepsilon_{PP} / \partial \ell n \rho)_T + (\partial \varepsilon_{CN} / \partial \ell n \rho)_T + (\partial \varepsilon_{3\alpha} / \partial \ell n \rho)_T + (\partial \varepsilon_\nu / \partial \ell n \rho)_T \ ,$$

3) decrease in hydrogen (by weight) per second

$$(dX/dt) = (dX/dt)_{PP} + (dX/dt)_{CN} \ ,$$

4) decrease in O^{16} (by weight) per second (dX_O/dt),

5) increase in Z (actually C^{12} by weight) per second (dY/dt).

§5. Advancing the Model

a) Time Steps

The timing routine calculates the time steps based upon a hydrogen- or helium-burning source. Let L_H (erg/s) be the total hydrogen-burning luminosity; and L_{He}, the helium luminosity. There are two time steps,

Δt_H = hydrogen-burning time step

Δt_t = total time step (i.e., for entropy and helium),

where $\Delta t_t \neq \Delta t_H$ only if the hydrogen shell is being shifted outward. If $L_H = 0$, the following section for hydrogen-burning is skipped.

For hydrogen-core burning ($X_{core} > X_c^{min}$), a time step corresponding to a set reduction in X_{core} is calculated. Let i be the innermost point if the core is radiative (i=1) or the outermost convective point if the core is convective. Then, the change in X_{core} is computed,

$$\Delta X_{core} = \min\{\Delta X_c^{max}, \Delta f_X^{max} \cdot X^i\},$$

and the time step is

$$\Delta t_t = \Delta t_H = 6 \cdot 10^{18} \cdot \Delta X_{core} \cdot m^i / L^i,$$

where m^i is the mass of the core (gm) and L^i is the luminosity of the core (erg/s, assumed to be mainly hydrogen burning).

When the core-burning criterion no longer applies ($X_{core} < X_c^{min}$), a limit is placed on the total amount of mass which may be burned.

$$\Delta m = \Delta f_m \cdot M_\theta \cdot X_{env}$$

$$\Delta t_H^m = 6 \cdot 10^{18} \cdot \Delta m / L_H$$

If there is a hydrogen-burning shell ($X_{core} = 0$), the timing routine locates it. Let $_0$ denote the inner edge of the shell (first point where $X > 0$); let $_{½}$ denote the mid-point of the shell ($X = ½X_{env}$); and let $_1$ denote the end of the shell ($L^i - L^{i-1} < 10^{-4} \cdot L$ or $X \simeq X_{env}$ or $\varepsilon_H = 0$). There is a limitation set on the maximum depletion of hydrogen at the mid-point of the shell.

$$\Delta t_H^{½} = \Delta X_{½}^{max} / (dX/dt)_{½}$$

With the exception of the core-burning phase, the new hydrogen burning time step is limited by the previous total time step.

$$\Delta t_H(new) = \min\{1.5 \cdot \Delta t_t(old),\ \Delta t_H^m,\ \Delta t_H^{½}\}$$

If there is to be no shell shifting then one sets $\Delta t_t = \Delta t_H$. If the hydrogen shell is to be shifted outward through Δm_s in mass, then the shift time step is computed as

$$\Delta t_{shift} = 6 \cdot 10^{18} \cdot X_1 \cdot \Delta m_s / L_H,$$

and the total time step is

$$\Delta t_t = \Delta t_H + \Delta t_{shift}.$$

If there is a hydrogen shell ($X_{core} = 0$), the helium burning is examined. For helium-core burning ($Y_{core} > X_c^{min}$ and $L_{core} > 0.10\ L_\odot$), the maximum helium depletion is

$$\Delta Y_{core} = \min\{\Delta Y_c^{max},\ \Delta f_Y^{max} \cdot Y_{core}\},$$

and the helium time step is

$$\Delta t_{He} = 5.85 \cdot 10^{17} \cdot \Delta Y_{core} \cdot M_\odot / L_{core}.$$

For helium-shell burning ($Y_{core} < X_c^{min}$), the amount of mass burned through by the helium shell is limited,

$$\Delta t_{He} = 5.85 \cdot 10^{17} \cdot \Delta f_m \cdot M_\odot / L_{He}.$$

The helium time step places an upper limit on the previously computed hydrogen time step,

$$\Delta t_t = \min\{\Delta t_t, \Delta t_{He}\},$$

$$\Delta t_H = \min\{\Delta t_t, \Delta t_H\}.$$

The following parameters used in the determination of the time step are read in at the beginning of each model run. Typical values are given.

$$X_c^{min} = 0.001$$

$$\Delta X_c^{max} = 0.04 \qquad \Delta Y_c^{max} = 0.02$$

$$\Delta f_X^{max} = 0.5 \qquad \Delta f_Y^{max} = 0.3$$

$$\Delta f_m = 0.0015\ M_\theta$$

$$\Delta X_{\frac{1}{2}}^{max} = 0.10$$

$$\Delta m_s = 5 \cdot 10^{-4}\ M_\theta$$

b) Composition Advance

The mixing routine performs all the operations on the model which are necessitated by the application of the time step to increase the age of the model. The routine first checks that there is no mixing within the hydrogen shell if the shell is supposed to be shifted. If there is such mixing, the shifting is suppressed (i.e., set $\Delta t_t = \Delta t_H$).

Each mass shell is burned individually by computing the energy generation rates for the physical conditions existing in that mass shell from the previously converged model. Since the program stores only the values of hydrogen, total metal and oxygen abundance, the change in these quantities is computed as

$$X(\text{new}) = X(\text{old}) - (dX/dt)\cdot\Delta t$$

$$Z(\text{new}) = Z(\text{new}) + (dY/dt)\cdot\Delta t$$

$$X_{16}(\text{new}) = X_{16}(\text{old}) - (dX_0/dt)\cdot\Delta t,$$

where $\Delta t = \Delta t_t$ inside the hydrogen shell ($X = 0$) and $\Delta t = \Delta t_H$ elsewhere.

The routine then mixes those zones which it is instructed to do so by being given a set of indices (i1, i2).

$$X_{i1} = X_{i1+1} = \ldots = X_{i2} = \bar{X} = \{\sum_{j=i1}^{i2} a_j \cdot X_j\}/\{\sum_{j=i1}^{i2} a_j\}$$

The weights a_j are proportional to the amount of mass associated with shell j and are set up in the point readjustment routine. The form of this mixing allows for arbitrary remixing and overlapping of mixing zones by the sequence of indices (i1, i2).

If the hydrogen shell is to be shifted, the routine calculates

$$\Delta s_{shift} = (\delta - \delta^2/2 + \delta^3/3 - \delta^4/4)/\ell n10,$$

where $\delta \equiv \Delta m_s/m_{\frac{1}{2}} << 1$. The points in the hydrogen shell are shifted by Δs_{shift},

$$s_0 \leq s^i \leq s_1 \rightarrow s^i(\text{new}) = s^i(\text{old}) + \Delta s_{shift},$$

where $s^i = \log m^i$. The points up to a distance $f_s\cdot\Delta s_{shift}$ in front of the shell are squeezed together,

$$s_1 < s^i < s_{end} \rightarrow s^i(\text{new}) = s^i(\text{old}) + \{s_{end} - s^i(\text{old})\}/f_s,$$

where $s_{end} \equiv s_1 + f_s\cdot\Delta s_{shift}$.

For all of these shifted and squeezed points the changes in log P and log T must be preserved for the calculation of

the entropy energy term in the subsequent model. Thus for every s^i(new), one must locate s^j(old) such that s^j(old) $\leq$ s^i(new) $< s^{j+1}$(old) (note that $j \geq i$ since s^i(new) $\geq s^i$(old)) and then interpolate linearly in s to get the old values of log P and log T which correspond to the new value of s. Then the effective changes are stored,

$$\Delta \log P^i = \log P^i(\text{new s}) - \log P^i(\text{pre-shift s})$$

$$\Delta \log T^i = \log T^i(\text{new s}) - \log T^i(\text{pre-shift s}).$$

For the region in front of the shell which is squeezed, it is desirable to preserve the original composition gradient if such a gradient exists. The values of X, Z and X_{16} are interpolated linearly in s as are log P and log T. Note that the shifting process affects only the value of s and not the values of (P, T, R, L, X, Z, X_{16}) with the exception of (X, Z, X_{16}) in the squeezed region.

The mixing routine finally checks on the physical sense of the new composition at all of the points.

$$X = \max\{X, 0\}$$

$$Z = \min\{Z, 1-X\}$$

$$X_{16} = \max\{X_{16}, 0.99 \cdot 10^{-3} \cdot Z_{CNO}\}$$

The first two requirements are obvious; the third requirement brings the value of X_{16} up to the approximate equilibrium value while turning off the X_{16} burning rate which is calculated if $X_{16} > 10^{-3} \cdot Z_{CNO}$. The value of Z_{CNO} is easily computed as $Z_{CNO} = Z - Z_m^0$ where Z_m^0 is the original weight abundance of all non-CNO metals. This method allows for the enrichment of CNO elements from the helium burning.

c) Mixing Zones

The mixing of the composition in convective regions of the stellar model is conventional. Consecutive mass shells, which are determined to be "convective" ($\nabla_r > \nabla_{ad}$) in the previously converged model, are mixed together.

If there is a helium-burning convective zone, the semi-convective instability is treated as an over-shooting (Castellani, Giannone and Renzini 1971) rather than a true semi-convection zone (Robertson and Faulkner 1972). The composition is first burned and mixed according to the standard convection zones. At the first radiative point outside a helium convective zone, the quantity $f \equiv \nabla_r{}^{int}/\nabla_r{}^{ext}$ is defined where the radiative gradient is computed with the (s, P, T, R, L) values of the radiative point and with the composition of both the radiative point (^{ext}) and the interior convective zone (^{int}). The original convective zone is extended outward through the radiative region for all the points at which $f \cdot \nabla_r > \nabla_{ad}$.

This over-shooting region is restricted to the helium core (X = 0) and is limited by the condition of Castellani, Giannone and Renzini (1971) which defines a maximum radius R_{max} of the over-shoot mixing.

$$\int_{R_c}^{R_{max}} (1 - \mu(R)/\mu_c^{int}) \cdot dR < (1 - \nabla_{ad_c}^{int}/\nabla_{r_c}^{int}) \cdot L_c \cdot \Delta t / (40\pi \cdot P_c \cdot R_c^2)$$

where the subscript $_c$ refers to the (s, P, T, R, L) values at the edge of the original convective zone. The composition

is then re-mixed from the beginning of the convective zone to the maximum extent of the over-shoot region.

d) Point Readjustment

The point readjustment routine refloats all of the points between successive models. This routine starts with the central point and places each subsequent new point i so that all of the following criteria are met:

$$s^i - s^{i-1} \leq \Delta s_{max}$$

$$\log P^i - \log P^{i-1} \leq \Delta P_{max}$$

$$L^i - L^{i-1} \leq \Delta f_L \cdot L^M \quad (M = \text{outermost point}).$$

All of the new values are interpolated linearly in s by locating the old point j such that $s^j(\text{old}) \leq s^i(\text{new}) < s^{j+1}(\text{old})$. The fundamental variables (s, P, T, R, L), the composition (X, Z, X_{16}), the density and the entropy terms ($\Delta \log P$, $\Delta \log T$) are refloated between the center and outermost points. These variables are stored in temporary arrays and are transferred to the original arrays once the process is completed. In addition to the 1^{st} and M^{th} points remaining fixed, other points may be retained:

1) the first radiative point (outer edge of convective zone),
2) the innermost point of the convective envelope,
3) the edge of the helium core (X = 0),
4) composition discontinuities, $X^j - X^{j-1} > \Delta X_{disc}$ or $Z^j - Z^{j-1} > \Delta Z_{disc}$.

The point routine then recalculates the weights assigned to each mass shell based upon the mass values at the preceding and following mid-points.

$$m_i = 10^{s_i}$$

$$a_1 = \tfrac{1}{2} \cdot (m_1 + m_2)$$

$$a_i = \tfrac{1}{2} \cdot (m_{i+1} - m_{i-1}) \quad \text{for } i = 2, M-1$$

$$a_M = m_{total} - \tfrac{1}{2} \cdot (m_M + m_{M-1})$$

The value m_i defines the location of the i^{th} shell, and a_i is the number of grams contained in the shell.

Additionally, the point routine adjusts the temperature of the outermost M^{th} point by adding a new point or deleting some old points. Given the desired temperature range T_{min} to T_{max}, then if $T_M < T_{min}$ the outermost point $j<M$ such that $T_j > \overline{T} \equiv \tfrac{1}{2} \cdot (T_{min} + T_{max})$ is selected as the new fit point. The points j+1 to M are deleted. If $T_M > T_{max}$ the process is more complicated. The last envelope which was integrated will have stored the values of (s_e, P_e, T_e, R_e) for the first inward integration step in which $T_e > \overline{T}$. If (s_f, P_f, T_f, R_f) are the values for that envelope at the fit point (i.e., $s_f = s_M$), then the new point M+1 is added with the following values.

$$s_{M+1} = s_e$$

$$\log P_{M+1} = \log P_M + (\log P_e - \log P_f)$$

$$\log T_{M+1} = \log T_M + (\log T_e - \log T_f)$$

$$\log R_{M+1} = \log R_M + (\log R_e - \log R_f)$$

$$L_{M+1} = L_M \qquad X_{M+1} = X_M$$

$$Z_{M+1} = Z_M \qquad X_{16M+1} = X_{16M}$$

§6. Model Calculation Sequence

The following list describes the sequence of calculations which is used in computing a series of stellar models.

(0) Input the model and compute a time step.

(1) Zero the entropy terms ($\Delta \log P = \Delta \log T = 0$).

(2) Locate the mixing zones and advance the composition and hydrogen shell for the given time step.

(3) Readjust the points in the model.

(4) Compute the new age of the model and reset any of the physical "constants" (e.g., G in the Brans-Dicke case).

(5) Retaining the old envelope triangle and surface boundary conditions, do N_1 iterations for corrections to the dependent variables (P,T,R,L) and apply a given fraction of the corrections.

(6) If necessary, relocate the envelope triangle for the partially converged model and compute new envelopes and surface boundary conditions.

(7) Do N_2 iterations or until the model converges.

(8a) If the corrections are excessively large at any time or if the model does not converge after N_2 iterations, then retain the previous model which has been stored on tape or disk and stop.

(8b) If the model has converged,

(i) compute a new time step,
(ii) perform the requested printing and punching,
(iii) store the model temporarily on tape or disk, over-writing the previous model,
(iv) return to step (1).

A. References

Allen, C.W. 1963, Astrophysical Quantities, (London: Athlone Press), Chapter 3.

Bahcall, J.N. and R.L. Sears 1972, Ann.Rev.Ast.& Ap., 10, 25.

Baker, N. and P. Kippenhahn 1962, Z.Ap., 54, 114.

Beaudet, G., V. Petrosian and E.E. Salpeter 1967, Ap.J., 150, 979.

Bulirsch, R. and J. Stoer 1966, Numerische Math., 8, 1.

Canuto, V. 1970, Ap.J., 159, 641.

Castellani, V., P. Giannone and A. Renzini 1971, Ap.& Space Sci., 10, 340.

Clayton, D.D. 1968, Principles of Stellar Evolution and Nucleosynthesis, (New York: McGraw-Hill), pp. 362-435.

Cox, A.N. and J.N Stewart 1970, Ap.J.Suppl.No.174, 19, 243&261.

Cox, J.P. and R.T. Giuli 1968, Principles of Stellar Structure, (New York: Gordon & Breach).

DeWitt, H.E., Graboske, H.C. and M.S. Cooper 1973, Ap.J., 181, 439.

Fowler, W.A., G.R. Caughlan and B.A. Zimmerman 1974, O.A.P., No. 380.

Graboske, H.C., H.E. DeWitt and A.S. Grossman 1973, Ap.J., 181, 457.

Henyey, L.G., J.E. Forbes and N.L. Gould 1964, Ap.J., 139, 306.

Henyey, L.G., M.S. Vardya and P. Bodenheimer 1965, Ap.J., 142, 841.

Hubbard, W.B. and M. Lampe 1969, Ap.J.Suppl.No.163, 18, 297.

Kippenhahn, P. 1967, J.Comp.Phys., 7, 181.

Krishna Swamy, K.S. 1966, Ap.J., 145, 174.

Paczynski, B. 1969, Acta Ast., 19, 1.

Robertson, J.W. and D.J. Faulkner 1972, Ap.J., 171, 309.

Schwarzschild, K. 1906, Göttinger Nachrichten, p. 41.

Schwarzschild, M. 1958, Structure and Evolution of Stars, (New York: Dover), p. 96ff.

Sweigart, A. 1974, private communication.

---------- 1975, private communication.

APPENDIX B. ISOCHRONES

The calculation of isochrones is based upon the ability to interpolate intermediate-mass evolutionary tracks from a set of computed tracks. For example, given the complete evolutionary sequence for a 0.90 $M_\odot$ star and a 1.00 $M_\odot$ star, one should be able to describe the evolution of a 0.95 $M_\odot$ star to within a well-defined error. The accuracy of the final isochrones will depend upon the accuracy of these interpolated tracks which will in turn depend upon the method of interpolation.

For the interpolation procedure, I claim that the positions of different mass stars which are at equivalent evolutionary phases (EEPs) are related (e.g., same central hydrogen abundance, same helium core mass). At these EEP points it is useful to compare the ages and luminosities in order to determine their variation with stellar mass. The age-mass relationship of some EEP points is shown in figure 1 for the STD models (Y=0.25, Z=0.02, $G \equiv G_0$). The relationship between log(age) and $\log(M/M_\odot)$ is nearly linear with some curvature at the high-mass end. The same data for the BDI models (see Chapter III) is plotted in figure 2 with the ZAMS relationship for the STD models shown for comparison. Even though G is variable, the values of log(age) and $\log(M/M_\odot)$ are still nearly linear over this range. The major difference between the STD and BDI models is that the slope of the line for the BDI models changes noticeably between different EEPs. This

is expected since the integrated effect of a decreasing G will cause a relatively faster evolution of the high-mass stars which complete their evolution in the younger, high-G universe.

The luminosity at these EEPs is compared with stellar mass for the STD models in figure 3 and for the BDI models in figure 4. Once again, $\log(L/L_\odot)$ and $\log(M/M_\odot)$ are approximately linear in this range and the slope of the relationship changes more radically for the BDI models.

From the observed linearity in figures 1-4, one can expect to reliably determine the age and luminosity for an intermediate-mass star at these phases of evolution by linearly interpolating in $\log(M/M_\odot)$. I shall assume that the effective temperature can be interpolated in the same manner as the luminosity. Thus, for a given stellar mass for which there exist bounding tracks, the fundamental quantities--age, log L and log T_{eff}--can be easily calculated at each of the EEP points. In order to determine the evolution of such a star between the EEP points, it is necessary to define more equivalent points in the original tracks. The insertion of such points between the original EEP points is done by dividing the evolutionary track between a pair of EEP points into equal "lengths". The number of intervals between the same EEP points for different mass tracks must be the same, and then the inserted points can be treated as EEP points. The major ambiguity in this process is the selection of the metric: how does one measure the "length"? The length between two

points of the originally computed evolutionary track can be any combination of variables. For example, defining

$$(\text{length})^2 \equiv (a \cdot \Delta \log L)^2 + (b \cdot \Delta \log T_{eff})^2 + (c \cdot \Delta \text{age})^2,$$

where (a,b,c) are arbitrary scaling factors, includes the three fundamental parameters of the evolution. For the definition of length I have have arbitrarily ignored the age and have used the length of the track as viewed in a reasonably scaled (log L, log T_{eff})-diagram: (a, b, c) = (1, 10, 0). For the giant branch I have used only log L to define the length: (a,b,c) = (1, 0, 0). If the selection of the original EEP points is made wisely, these newly added points should not critically affect the interpolation procedure.

Now one has a set of evolutionary tracks for a range of masses such that, starting with the ZAMS points, each successive point is a corresponding EEP point for all of the masses. Not all of the tracks will have the same number of points since it is unnecessary to extend the evolution of low-mass stars beyond the ages in which one is interested. The construction of an isochrone for a time τ proceeds as follows:

1. Select an EEP point.
2. Locate the pair of tracks (i,j) whose ages at the selected EEP point bound the desired age τ.

   $$\tau_i \leq \tau \leq \tau_j$$

   (If the value of τ cannot be bounded, then the two tracks with the nearest times must be used. However, the extrapolation may have considerably larger errors than the interpolation.)
3. Define the interpolating weight,

   $$f \equiv (\log \tau - \log \tau_i)/(\log \tau_j - \log \tau_i),$$

and use it to interpolate the value of the mass,

$$\log M = \log M_i + f\cdot(\log M_j - \log M_i),$$

and the values of $\log L/L_\odot$ and $\log T_{eff}$ in the same manner with the same weighting factor.

4. Repeating the process for all the EEP points, one has a sequence of (M, log L, log T_{eff}) points for a given age τ (i.e., an isochrone).

This procedure has a distinct advantage over the standard procedure of feeding in a sequence of masses and computing their location in the HR diagram. Using the above technique guarantees placing a "star" at every EEP point. The density of points along the isochrone is equal to the density of EEP points, and thus one is able to have a uniform sample of stars through even the fastest phases of evolution. A rapid evolutionary phase can be discerned by the small increment in mass between successive points. Between a pair of points (i,i+1) in the isochrone, the number density of "stars" is readily calculated as

$$N(i,i+1) = \phi\{\tfrac{1}{2}\cdot(M_i+M_{i+1})\}\cdot(M_{i+1}-M_i),$$

where $\phi\{M\}$ is the initial mass function. Similarly, each point i can be allotted a weighting factor for use in the computation of integrated luminosities,

$$W_i = \phi\{M_i\}\cdot\tfrac{1}{2}\cdot(M_{i+1} - M_{i-1}).$$

In order to estimate the accuracy of this interpolation procedure, I have tried to devise a rigorous test: (i) use two evolutionary tracks to interpolate an intermediate track which is already known; (ii) instead of comparing only the positions of the true and the interpolated tracks in the

(log L, log T_{eff})-diagram, compare also the ages along each of the tracks. For this purpose the interpolation procedure is as follows:

1. Define the interpolating weight factor,

$$f \equiv (\log M - \log M_i)/(\log M_{i+1} - \log M_i),$$

where (i,i+1) are the bounding tracks.

2. For every pair of EEP points in the bounding tracks, interpolate the values of (log τ, log L, log T_{eff}) linearly using f.

3. One now has the interpolated track for mass M. To find the value of (log L, log T_{eff}) at a given age τ_0, locate the points on the interpolated track which bound τ_0 and interpolate (log L, log T_{eff}) linearly with τ.

This test is made for the 1.10 M_θ STD model track by using the 1.20 M_θ and 1.00 M_θ STD tracks for the interpolation. This particular case should reveal the largest errors since the log τ-log M and log L-log M relationships are most non-linear in this mass range. The results are shown in figure 5, where at a given set of ages the location of the true 1.10 M_θ star in the (log L, log T_{eff})-diagram is compared with the location of the interpolated 1.10 M_θ star. This process is repeated for the BDI models using the 1.10 M_θ and 0.90 M_θ tracks to interpolate the 1.00 M_θ track and is shown in figure 6. Taking into account both the shape of the track and the time scales along the track, the interpolated track agrees very well with the true track in both cases. Any similar errors in the final isochrones should be smaller than the errors in this test since the most non-linear region was tested

and the mass interval (0.2 $M_\odot$) is twice that to be used in the isochrone construction.

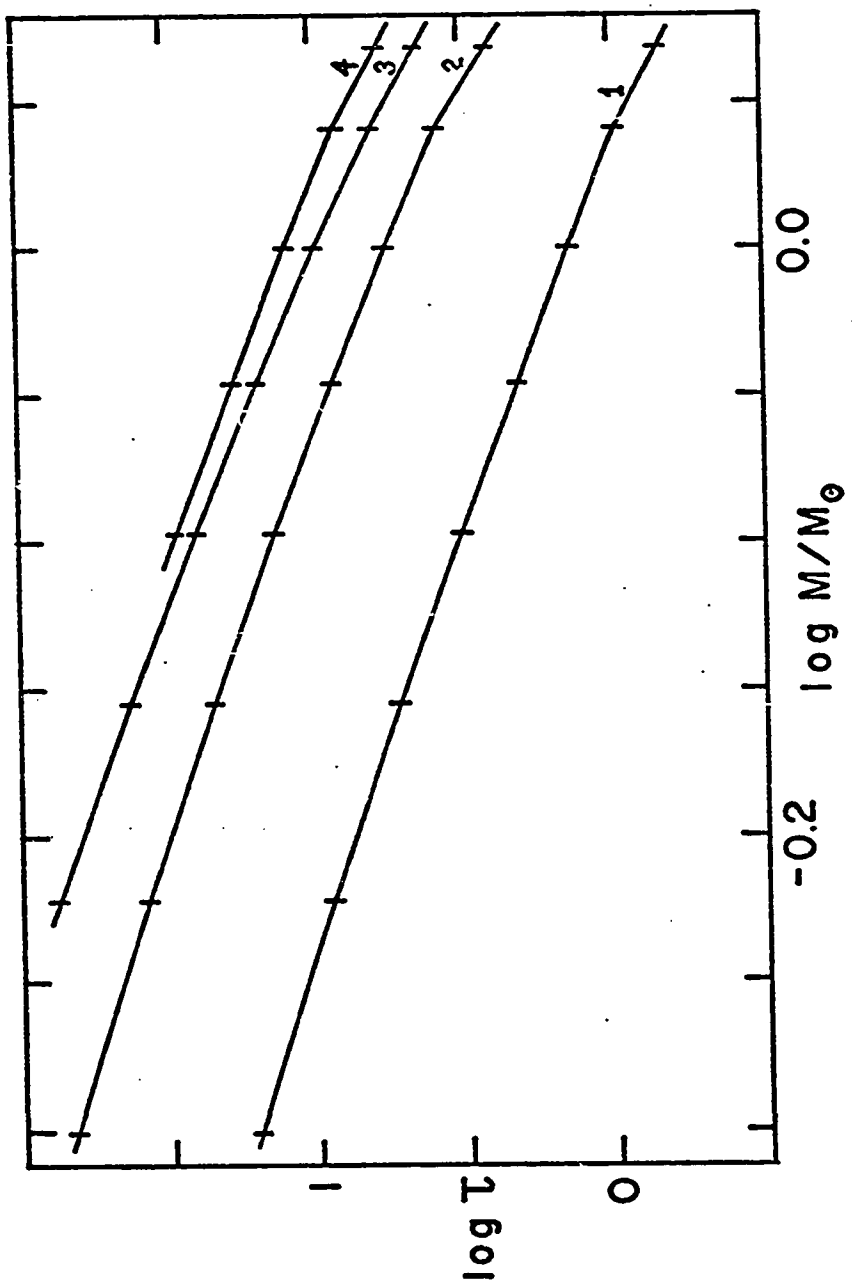

Fig.1.---Log τ vs. log M for STD models. τ is the evolutionary age in units of Gyr except for line 1. Each solid line corresponds to an equivalent phase of evolution: 1) ZAMS, τ = M/L in solar units, 2) X_c = 0.30, 3) X_c = 0.0002, 4) M_{core} = 0.150 $M_\odot$.

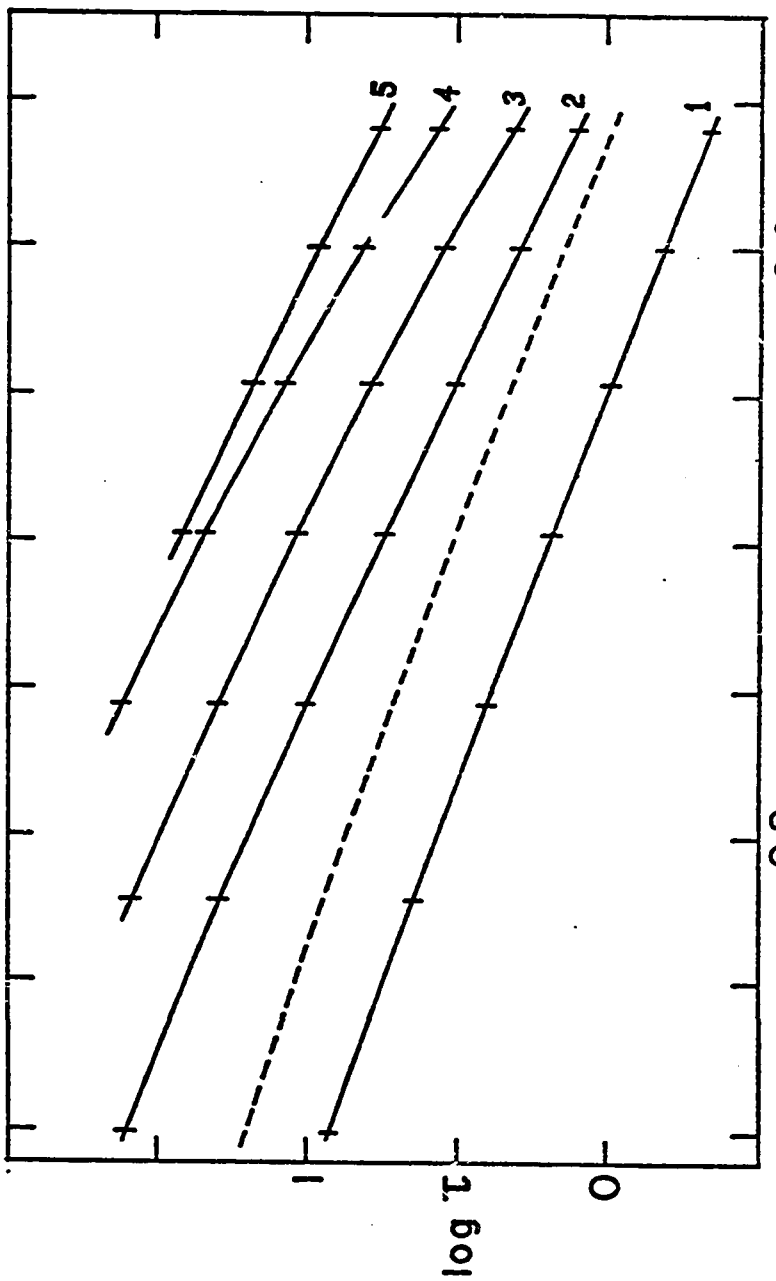

Fig.2.---Log τ vs. log M for BDI models (see Fig. 1). Each solid line corresponds to 1) ZAMS, τ = M/L in solar units, 2) X_c = 0.46, 3) X_c = 0.26, 4) X_c = 0.0002, 5) M_{core} = 0.150 $M_\odot$. The dashed line is the ZAMS relationship for the STD models (line 1 of Fig. 1).

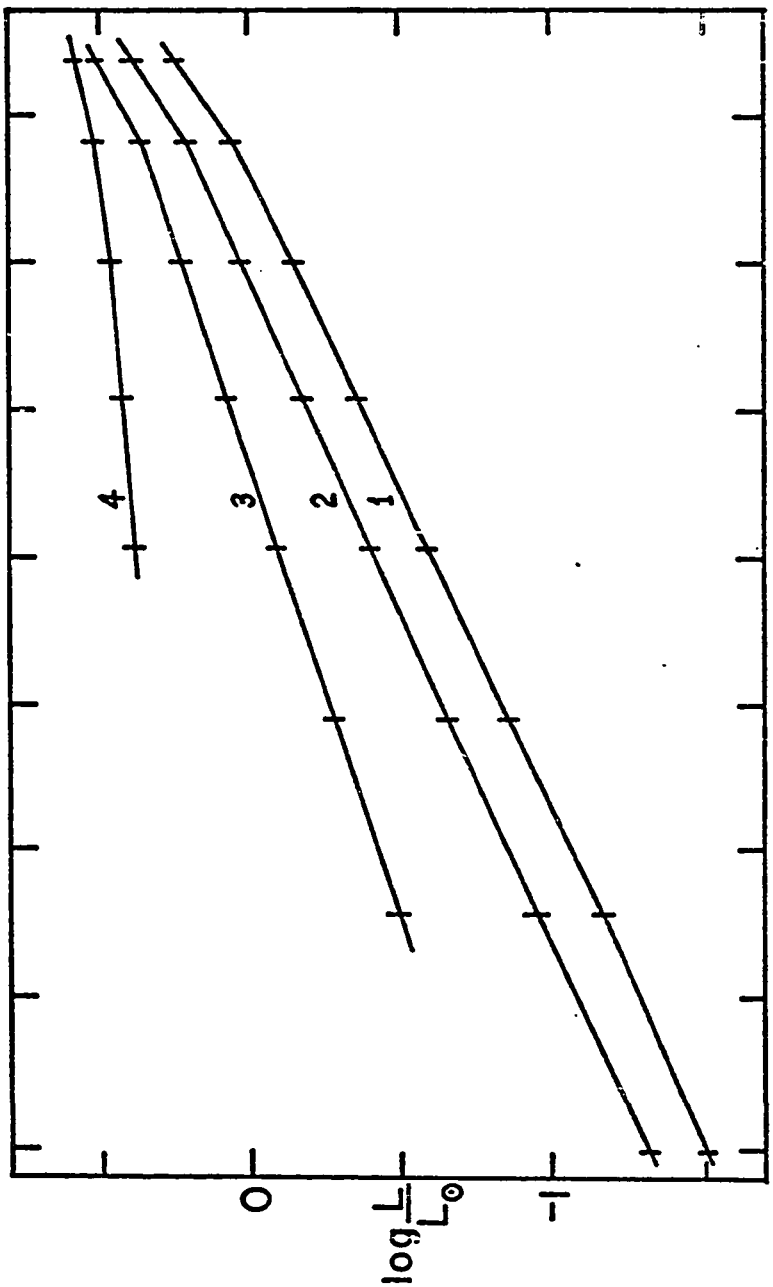

Fig.3.---Log L/L_θ vs. log M for STD models. Each solid line corresponds to an equivalent phase of evolution: 1) ZAMS, 2) $X_c = 0.30$, 3) $X_c = 0.0002$, 4) $M_{core} = 0.150\ M_\theta$.

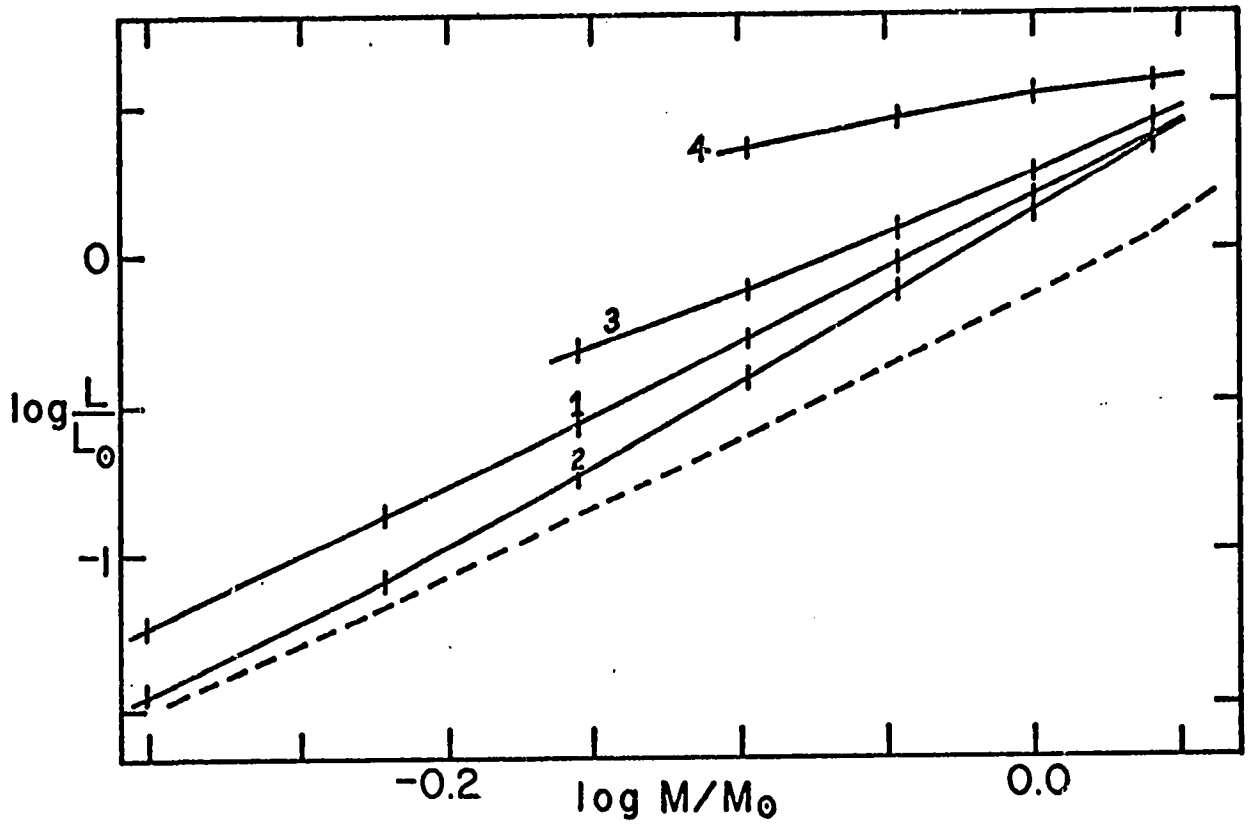

Fig.4.---Log L/L_0 vs. log M for BDI models. Each solid line corresponds to an equivalent phase of evolution: 1) ZAMS, 2) $X_c = 0.46$, 3) $X_c = 0.0002$, 4) $M_{core} = 0.150\ M_0$. The dashed line is the ZAMS relationship for the STD models (line 1 of Fig. 3).

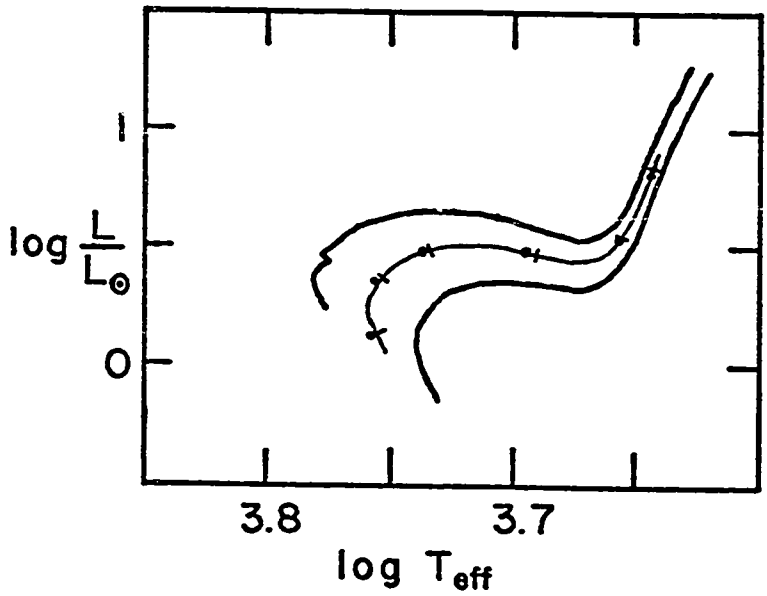

Fig.5.---Log L/L_θ vs. log T_{eff} interpolation for STD models. The two bounding tracks (1.2 and 1.0 M_θ) along with the true intermediate-mass track (1.1 M_θ) are shown. At a range of evolutionary ages the true location of the 1.1 M_θ star is denoted by tick marks. These are to be compared with the dots which are the location of the 1.1 M_θ star as predicted from the interpolation with the bounding tracks.

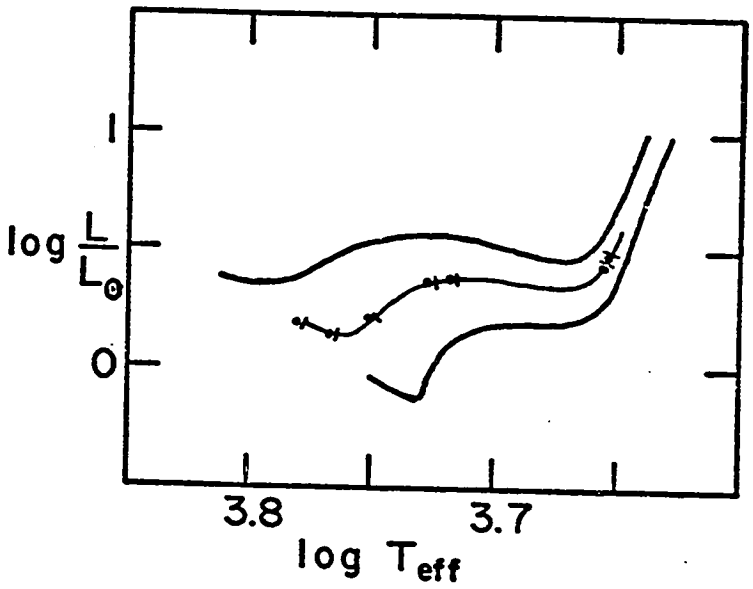

Fig.6.---Log L/L_θ vs. log T_{eff} interpolation for BDI models. This figure is the same as Fig. 5 except for the masses of the bounding tracks (1.1 and 0.9 M_θ) and the intermediate track (1.0 M_θ).

APPENDIX C. COLOR CALIBRATIONS

This appendix describes the conversion of my theoretical (log L, log T_{eff}) values for solar abundance stars into the observable broad-band UBVRIJKL magnitudes and colors of Johnson (1966). For both main sequence (Class V) stars and giant (Class III) stars the (color, color)- and (color, bolometric correction)-calibrations are established. In order to obtain a reliable (color, log T_{eff})-calibration for my stellar models, the T_{eff} calibrations in the literature must be discarded. Instead, the observed color-magnitude sequences are converted into color-M_{bol} sequences with the already established calibrations. Then they are compared with my (log L, log T_{eff}) sequences to give a (color, log T_{eff})-relationship. The resultant calibration reproduces the observed color-magnitude sequences with my own stellar models.

For the class V color-color relationships, the (B-V), (V-R), (V-J), (V-K) and (V-L) colors of Johnson (1966) are calibrated against (V-I). The (U-V) color (Johnson 1966, Morton and Adams 1968, FitzGerald 1970) is calibrated against (B-V) as is the bolometric correction (Schlesinger 1969). No corrections for TiO-blanketing are applied to the lower main sequence. This color-color calibration for spectral class A0 V through M5 V is given in table 1.

At each (B-V) value in this color calibration, a value of M_V is interpolated from the observed zero-age main sequence (ZAMS) of Johnson (1963) and Allen (1963) which is listed in table 3. The absolute visual magnitude is converted to a

bolometric magnitude, $M_{bol} = M_V$ - B.C., which then is compared with my theoretical ZAMS to interpolate a log T_{eff} value for each tabulated (B-V) value. My ZAMS spans the mass range 0.5-1.2 $M_\odot$ for composition (Y,Z) = (0.25,0.02) and was extrapolated to cover the full range of the color calibration. The resulting (log T_{eff}, color)-relationship for the main sequence is listed also in table 1.

The T_{eff}-color relationship for the class III giant stars is derived in a manner similar to that for the main sequence stars. All of the colors and the bolometric correction are calibrated against the (V-I) color. The data of Johnson (1966) is used for early giants; and the data of Lee (1970), for M-giants. The TiO-blanketing in the V-magnitude, δV, is taken from Wing (1967) and is calibrated against spectral type. The bolometric magnitude is then given by $M_{bol} = M_V$ - B.C. - δV. Two separate observed giant branch (GB) sequences which are listed in table 4 are used to derive the T_{eff}-color relationship. The (M_V, B-V) GB of M67 (Racine 1971, Eggen 1972) is used for G and K giants; and the (M_I, R-I) GB of the old disk population (Eggen 1973), for M-giants. For the early giants I combined my 1.2 $M_\odot$ GB track with the M67 GB to determine T_{eff} at each tabulated (V-I); for the M0-M3 giants, my 1.2 $M_\odot$ GB track with the old disk GB; and for the M4-M6 giants, the mean of my 1.0 $M_\odot$ and 1.2 $M_\odot$ asymptotic GB extensions with the old disk GB. The three resulting T_{eff}-color calibrations agree to within 0.002 in log T_{eff} at the two junctures points. The adopted T_{eff}-color calibration for

giant stars is listed with the color-color calibration in table 2. The first two lines of table 2 (class V colors) are included so that the class III colors merge smoothly with the class V colors.

The T_{eff}-color calibrations for class V and class III stars has been derived. The sub-giant stars (class IV) are not considered separately because they could not be adequately calibrated. The super-giant stars can be safely ignored because all of the stars in this study are of relatively low mass. Thus, to compute the visual magnitude and colors of a star from its (log L, log T_{eff}) value, one interpolates in tables 1 and 2 with respect to log T_{eff} and obtains the colors, δV and bolometric correction for the corresponding class V and--where possible--class III stars. If the star lies within one magnitude of the theoretical-ZAMS bolometric magnitude at its T_{eff} value, then the class V colors are adopted. If the star is more than two magnitudes above the ZAMS, only class III values are employed. In the middle of these two cases, the values are interpolated between class III and class V. Once these quantities have been derived, the luminosity in any broad-band color (e.g., C) can be calculated from,

$$\log L_C/L_\odot = \log L/L_\odot - 0.4 \cdot \{B.C. + \delta V - (V-C)\}.$$

TABLE 1. CLASS V CALIBRATIONS

Sp.Cl.	B.C.	U-V	B-V	V-R	V-I	V-J	V-K	V-L	$\log T_{eff}$
A0	0.30	0.00	0.00	0.03	0.01	0.00	-0.02	0.00	4.0796
A2	0.20	0.12	0.06	0.08	0.09	0.11	0.13	0.16	4.0447
A4	0.13	0.21	0.11	0.13	0.17	0.21	0.27	0.31	4.0112
A7	0.08	0.31	0.20	0.20	0.29	0.36	0.48	0.55	3.9538
	0.07	0.36	0.27	0.25	0.39	0.48	0.65	0.75	3.9095
F0	0.07	0.37	0.31	0.28	0.45	0.55	0.75	0.87	3.8836
	0.07	0.38	0.33	0.30	0.47	0.58	0.79	0.90	3.8694
F2	0.06	0.40	0.38	0.35	0.55	0.68	0.93	1.07	3.8348
	0.05	0.42	0.42	0.38	0.60	0.74	1.00	1.17	3.8112
F5	0.05	0.46	0.45	0.39	0.63	0.77	1.05	1.23	3.7948
	0.06	0.52	0.50	0.43	0.69	0.86	1.15	1.34	3.7732
F8	0.08	0.61	0.55	0.47	0.75	0.94	1.25	1.44	3.7599
G0	0.09	0.72	0.60	0.49	0.80	1.01	1.34	1.52	3.7471
G5	0.13	0.91	0.68	0.55	0.91	1.17	1.53	1.72	3.7284
	0.18	1.09	0.75	0.60	0.99	1.28	1.69	1.88	3.7149
K0	0.21	1.22	0.80	0.63	1.05	1.36	1.81	1.98	3.7052
K2	0.31	1.58	0.92	0.75	1.23	1.58	2.16	2.26	3.6831
	0.44	1.81	1.00	0.82	1.35	1.72	2.34	2.43	3.6702
K5	0.76	2.25	1.18	0.99	1.62	2.04	2.75	2.84	3.6434
	1.15	2.61	1.37	1.19	2.01	2.49	3.33	3.51	3.6134
M0	1.37	2.68	1.42	1.26	2.16	2.67	3.55	3.73	3.6057
M1	1.65	2.70	1.49	1.39	2.43	3.03	3.92	4.11	3.5800
M2	1.98	2.70	1.51	1.50	2.69	3.37	4.27	4.47	3.5794
M4	2.30	2.70	1.55	1.69	3.18	3.96	4.85	5.17	3.5401
M5	2.60	2.77	1.60	1.83	3.54	4.37	5.26	5.80	3.4780

TABLE 2. CLASS III CALIBRATIONS

Sp.Cl.	B.C.	δV	U-V	B-V	V-R	V-I	V-J	V-K	V-L	$\log T_{eff}$
(G0V)	0.13	0.00	0.91	0.68	0.55	0.91	1.17	1.53	1.72	3.7284
(K0V)	0.16	0.00	1.22	0.80	0.63	1.05	1.36	1.81	1.98	3.6811
G5	0.20	0.00	1.55	0.92	0.69	1.17	1.52	2.08	2.18	3.6481
K0	0.30	0.00	1.93	1.04	0.77	1.30	1.71	2.35	2.47	3.6241
K2	0.42	0.00	2.32	1.16	0.84	1.42	1.87	2.59	2.73	3.6045
K3	0.61	0.00	2.74	1.30	0.96	1.61	2.12	2.92	3.07	3.5803
K4	0.81	0.05	3.07	1.41	1.06	1.81	2.36	3.24	3.39	3.5567
M0	1.14	0.20	3.42	1.56	1.24	2.14	2.77	3.74	3.89	3.5214
M1	1.24	0.25	3.48	1.58	1.29	2.24	2.89	3.90	4.06	3.5130
M2	1.45	0.30	3.52	1.61	1.37	2.45	3.12	4.16	4.33	3.4970
M3	1.81	0.47	3.49	1.62	1.52	2.82	3.53	4.63	4.81	3.4710
M4	2.42	0.76	3.33	1.62	1.78	3.38	4.19	5.34	5.54	3.4430
M5	3.15	1.25	3.04	1.59	2.13	4.06	4.96	6.20	6.44	3.4100
M6	4.10	1.65	2.70	1.58	2.70	4.90	5.90	7.20	7.50	3.3000

TABLE 3. OBSERVED ZAMS

M_V	(B-V)	M_V	(B-V)
1.10	-0.05	5.88	0.80
1.50	0.00	6.32	0.90
1.74	+0.05	6.78	1.00
2.00	0.10	7.20	1.10
2.45	0.20	7.66	1.20
2.95	0.30	8.11	1.30
3.56	0.40	8.6	1.40
4.23	0.50	9.6	1.50
4.79	0.60	12.0	1.60
5.38	0.70	16.0	1.70

TABLE 4. OBSERVED GIANT BRANCH

M67		Old Disk	
M_V	(B-V)	M_I	(R-I)
3.56	0.83	-1.00	0.562
3.00	0.91	-1.50	0.625
2.50	0.96	-2.00	0.687
2.00	1.00	-2.40	0.750
1.50	1.07	-2.95	0.875
1.00	1.15	-3.20	0.937
0.50	1.25	-3.60	1.062
0.00	1.35	-4.05	1.250
		-4.20	1.312
		-4.40	1.437
		-4.90	1.687
		-5.40	1.937
		-5.65	2.062

C. References

Allen, C.W. 1963, Astrophysical Quantities, (London: Athlone Press), p.199.

Eggen, O.J. 1972, Ap.J., 172, 639.

--------- 1973, P.A.S.P., 85, 542.

FitzGerald, M.P. 1970, Astr.& Ap., 4, 234.

Johnson, H.L. 1963, Basic Astronomical Data, K.Aa. Strand ed., (Chicago: University of Chicago Press), p.216.

---------- 1966, Ann.Rev.Astr.& Ap., 4, 193.

Lee, T.A. 1970, Ap.J., 162, 217.

Morton, D.C. and T.F. Adams 1968, Ap.J., 151, 611.

Racine, R. 1971, Ap.J., 168, 393.

Schlesinger, B.M. 1969, Ap.J., 157, 533.

Wing, R.F. 1967, Ph.D. dissertation, University of California, Berkeley.